Development of a compact hard X-ray split-and-delay line for studying ultrafast dynamics at free electron laser sources

Dissertation

zur Erlangung des Doktorgrades

an der Fakultät für Mathematik, Informatik und Naturwissenschaften

Fachbereichs Physik

der Universität Hamburg

vorgelegt von

Rustam Rysov

Hamburg

2019

Gutachter/innen der Dissertation: Prof. Dr. Gerhard Grübel
Prof. Dr. Martin Trebbin

Zusammensetzung der Prüfungskommission: Prof. Dr. Gerhard Grübel
Prof. Dr. Martin Trebbin
Prof. Dr. Robin Santra
Prof. Dr. Nina Rohringer
Prof. Dr. Christian Schroer

Vorsitzender des Prüfungskomission: Prof. Dr. Robin Santra

Datum der Disputation: 27 September 2019

Leiter des Fachbereichs PHYSIK: Prof. Dr. Wolfgang Hansen
Dekan der Fakultät MIN: Prof. Dr. Heinrich Graener

Abstract

The study of condensed matter dynamics on ultrafast timescales is one of the key topics in modern material science research. Hard X-ray free-electron laser sources with extreme peak brightness and ultra short pulses provide excellent conditions for studying ultrafast dynamics in the time domain by employing such techniques as X-ray pump-probe spectroscopy or X-ray photon correlation spectroscopy. However, the intrinsic time structure of FEL sources limits the investigated timescales to 0.2 microseconds or slower. One way of overcoming this limitation is split-and-delay technology. This work presents a new concept for a compact hard X-ray split-and-delay device, enabling such experiments at X-ray FEL sources. The device is designed to split a single X-ray pulse into two fractions introducing time delays from -5 to 815 ps. Accessing such timescales allows to push studies of ultrafast dynamics beyond the intrinsic temporal limit of the X-ray source. The split-and-delay unit is based on Bragg optics and modern technologies for mechanics. Having a compact portable design with dimensions of $60\times60\times30$ cm^3 and a weight of about 60 kg allows to install the device in basically any experimental hutch of a FEL source. The split-and-delay line utilizes a combination of various silicon Bragg optics, arranged in various configurations, enabling the operation in the energy range from 7 to 16 keV. The quality of the beam splitting optics is checked by X-ray topography measurements. A novel method for the split-and-delay line alignment and time delay calibration using a infrared laser setup is developed and successfully used. The infrared setup allows a temporal pre-alignment with a precision better than 22 ps without the need for X-rays. The performance of the split-and-delay setup is checked by measuring the throughput and the delay times with the use of Si(111), Si(220) and Si(422) optics at 7 keV and 9 keV photon energies. Delay times are measured, ranging from 130 ps to 716 ps. The average uncertainty of measured delay times is 16.2 ps. The results show, that ultrafast pump-probe or XPCS experiments can be carried out with the compact split-and-delay line.

Zusammenfassung

Die Messung der Dynamik kondensierter Materie auf ultraschnellen Zeitskalen ist eines der Schlüsselthemen in der modernen Erforschung der Materialwissenschaften. Heutzutage ermöglichen Freie Elektronen-Laser (FEL) mit extremer Spitzenbrillianz und ultrakurzen Pulsen ultraschnelle Dynamik in der Zeitdomäne zu studieren, indem Methoden wie die Pump-Probe-Spektroskopie oder die Röntgen-Photon-Korrelations-Spektroskopie verwendet werden. Jedoch ist der Untersuchungszeitraum aufgrund der intrinsischen Zeitstruktur von FEL-Quellen auf 0.2 Mikrosekunden oder langsamer eingeschränkt. Die Split-and-Delay-Technologie ist eine Möglichkeit, diese Einschränkung zu überwinden. In dieser Arbeit wird ein neues Konzept einer kompakten split-and-delay-Einheit für harte Röntgenstrahlen präsentiert, mit dem Experimente an Röntgen FEL-Quellen durchgeführt werden können. Diese Einheit ist in der Lage einen einzelnen Röntgenpuls in zwei Pulse zu spalten, um Laufzeitunterschiede von -5 ps bis 815 ps zwischen den beiden Pulsen herbeizuführen. Diese Zeitskalen erlauben es ultraschnelle Dynamik jenseits von intrinsisch zeitlichen Einschränkungen der Röntgenquelle durchzuführen. Die split-and-delay-Einheit basiert auf Bragg-Röntgenoptik und modernen Technologien für die Mechanik. Das portable und kompakte Design von $60{\times}60{\times}30$ cm^3 und das Gewicht von ungefähr 60 kg erlaubt es, das Gerät in beliebigen experimentellen Aufbauten einer FEL-Quelle zu installieren. Die split-and-delay-Einheit nutzt einen Kombination von unterschiedlichen Silizium-Bragg-Optiken in verschiedenen Konfigurationen, die einen Betrieb im Bereich Röntgenenergie von 7 keV bis 16 keV ermöglichen. Die Qualität der Strahlaufteilungs-Optiken wird in Röntgen-Topografie-Messungen geprüft. Die neuartige Methode der split-and-delay-Anordnung und die Kalibrierung der Laufzeitunterschiede mit einem Infrarot-Laser-Aufbau wird entwickelt und erfolgreich eingesetzt. Dieser Infrarot-Laser-Aufbau ermöglicht die zeitliche Voreinstellung ohne Röntgenstrahlen mit einer Genauigkeit von weniger als

22 ps. Die Leistung des split-and-delayAufbaus wird in Messungen der Transmission und Laufzeitunterschiede mit Si(111)-, Si(220)- und Si(422)-Optiken bei Photonenenergien von 7 keV und 9 keV durchgeführt. Die Laufzeitunterschiede reichen von 130 ps bis 716 ps. Die durchschnittliche Unsicherheit der gemessenen Laufzeitunterschieden beträgt 16.2 ps. Die präsentierten Messungen demonstrieren, dass ultraschnelle Pump-Probe oder XPCS-Experimente mit der kompakten split-and-delay-Einheit durchgeführt werden können.

Contents

Chapter 1

Introduction

Hard X-ray Free Electron Laser (FEL) sources based on Self Amplified Spontaneous Emission (SASE) (see Section 1.1) provide spatially coherent, brilliant ultrashort pulses with more than 10^{12} photons/pulse [1–6]. Study of the condensed matter dynamics on ultrafast timescales nowadays is one of the research topics using FEL sources [7–9]. This kind of investigations in many fields of science including molecular biology, medicine or chemistry can be done using the third generation of X-ray synchrotron sources [10]. These X-ray sources deliver nowadays pulses with a ∼100 ps duration allowing to perform time resolved experiments [11]. However, for many applications the duration and intensity of storage ring pulses are still limiting research capabilities. FELs enable to study fast dynamics in the time domain using correlation spectroscopy [12, 13]. Moreover, some of the experimental methods require a time delay between two pulses in order to measure the sum of two coherent scattering patterns and provide a dynamical information on equilibrium condensed matter systems.

XPCS with two pulses and pump-probe experiments can be enabled by having a controlled short delay time between two X-ray pulses on the picosecond timescales (<1 ns) and faster [14]. Such double pulse control can be achieved by accelerator techniques via tuning the single electron bunch or produce multiple bunches (see

Section 1.5). Another approach is based on optical means by splitting and delaying FEL pulses. Split-and-delay line (SDL) devices have been built and operated with EUV light and soft X-rays. This concept was transferred into the hard X-ray range (see Section 1.5). The first hard X-ray SDL design was realized with the 90 degree scattering geometry design based on Bragg crystals and was built at DESY [15, 16], providing delays up to 3.5 ns. Stationary SDL devices are operating at LCLS [17], SACLA [18, 19] and European XFEL [20, 21] employing various optical configurations. First measurement of nanosecond equilibrium structural dynamics was performed at LCLS [22], providing the first demonstration of split-pulse x-ray photon correlation spectroscopy (XPCS) at an FEL source.

This thesis work present a novel concept of a compact hard X-ray SDL device based on the Bragg crystal optics.

1.1 Modern X-ray sources

X-ray radiation was discovered by Wilhelm Röntgen in 1895 [23]. It is a electromagnetic wave with a spectrum covering the wavelength range from 10 nm to 0.01 nm. This range makes X-rays a perfect tool to study the atomic structure of the matter.

A number of X-ray sources were developed, starting from X-ray tubes in the end of XIX century [36]. X-rays have been one of the most important research and investigation tools in medicine, chemistry and physics, taking images of solid objects, determining the structure of crystalline materials, and their chemical composition. Nowadays third generation synchrotron sources provide intense and pulsed X-ray radiation with a pulse duration of $\sim$100 ps [10]. The term synchrotron radiation is used for the radiation emitted by accelerated charged particles moving with relativistic speed. Typically this is achieved in a storage ring where electrons are circulating in a closed orbit, for example as PETRA III in Hamburg (Germany) [37] or European Synchrotron Radiation Facility (ESRF) in Grenoble (France) [38]. The generation of X-ray radiation in storage rings nowadays is achieved by insertion devices - wigglers and undulators, that are placed into the storage ring in the path of the electrons, consisting of two sets of magnets, which are aligned along the electrons trajectory. Magnets have alternating magnetic poles in one row along the beam propagation, emitting the photons from oscillating electrons in the variable magnet field [39]. Undulator produces a linearly polarized radiation and the photon energy can be tuned by varying the gap between magnetic poles.

X-ray free-electron lasers (FELs) are newly developed light sources based on the Self-Amplified Spontaneous Emission (SASE) [40]. The initial concept of FEL was suggested by John Madey [41]. In the conventional FEL scheme electrons are accelerated by a linear accelerator followed by the long array of undulators [42].

Facility	**Location**	**Status**	**Emittance, µm**	**Energy range, keV**	**Repetition rate (max.)**	**Beam size, µm**	**Divergence, µrad**
XFEL [4]	Germany	O	1.4	0.26-25	4.5 MHz	1 - 100	1
FLASH [**24**, **25**]	Germany	O	<2	0.02-0.3	5kHz[1]	> 5µm	90
FLASH-II [**25**, **26**]	Germany	O	1-1.5	0.01-0.31	5kHz[1]	> 10µm	90
LCLS [**5**, **27**]	USA	O	1	0.28-11.2	120 Hz	2-750	1.1
LCLS-II [**28**]	USA	C	1	0.28-25	120 Hz	2-1000	1.1
SACLA [**29**, **30**]	Japan	O	0.8	4-20	60 Hz	1-35	0.73
FERMI [**31**, **32**]	Italy	O	1	0.01-0.31	50 Hz	> 5µm	1.25 rad.
SwissFEL [**33**, **34**]	Switzerland	O	0.4	1.7-12.4	100 Hz	1-10	1.1
PAL XFEL [**6**, **35**]	Korea	O	1	2-20	60 Hz	1-35	1.5

Table 1.1: Current status and parameters of modern FEL facilities. The status is marked as operational (O) or under construction (C).

---

[1] split between FLASH and FLASH II

Currently, modern FEL sources are rapidly developing and many new facilities have been built over the world (see Figure 1.1). This opportunity opens up new frontiers in many areas of physics, chemistry and biology. The parameters of different FEL sources are summarized in the Table 1.1.

The time structure of the FEL radiation pulses is mainly determined by the electron source of the beam. The repetition rate of the hard X-ray FEL sources is typically ranging from 60 Hz to MHz (see Table 1.1). The highest repetition rate is achieved by the European XFEL in Hamburg with up to 4.5 MHz pulse frequency. This facility provides pulses is trains with the repetition rate of 10 Hz. Up to 2700 pulses per train can be produced [4] with a minimum separation time of 222 ns. At this repetition the high flux is achieved due to the microbunching of electrons in the undulator, leading to the laser-like amplification [4]. A detailed explanation of the FEL time structure in the context of implementing SDL devices will be given in Section 2.2.

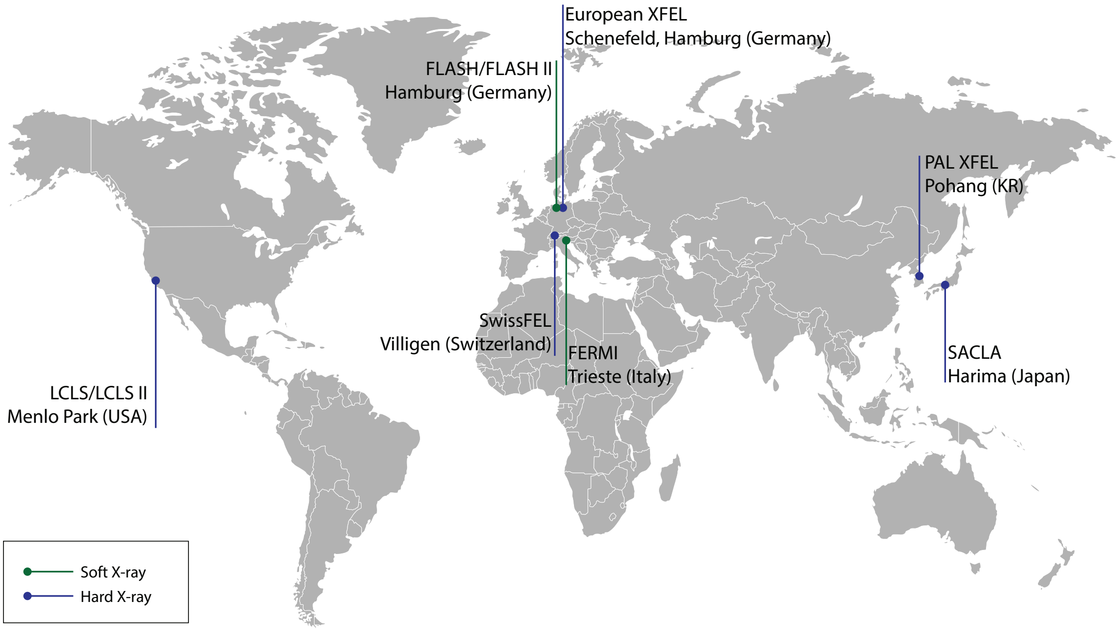

Figure 1.1: Modern X-ray Free Electron Lasers

1.2 Ultrafast dynamics

FEL radiation enables a new method to track changes in interatomic structure of materials on timescales as short as a few tens of femtoseconds. By combining a very high time-resolution with highly specific structural probes such as X-ray diffraction [43], it becomes possible to achieve a profoundly new understanding of the forces that determine the dynamic properties in materials. FELs make it possible to study molecular reactions on femtosecond and picosecond timescales. Figure 1.2 shows the typical timescales of some processes, that take place in condensed matter. For instance, thermal diffusion is a relatively slow process, typically occurring on the nanosecond timescale. In contrast, photon absorption, charge transfer, intramolecular vibrational motions and simulated emission are much faster and occur on picosecond timescales [44]. One of the methods to study such ultrafast processes is to conduct pump-probe experiments (see Section 1.3). For instance, investigations the ultrafast nucleation processes that occur during the ablation process in semiconducting materials [45] can be performed.

With the use of ultrafast XPCS techniques (see Section 1.4) it is possible to study equilibrium dynamics and investigate transient short- and medium-range structures of molecular fluids [46].

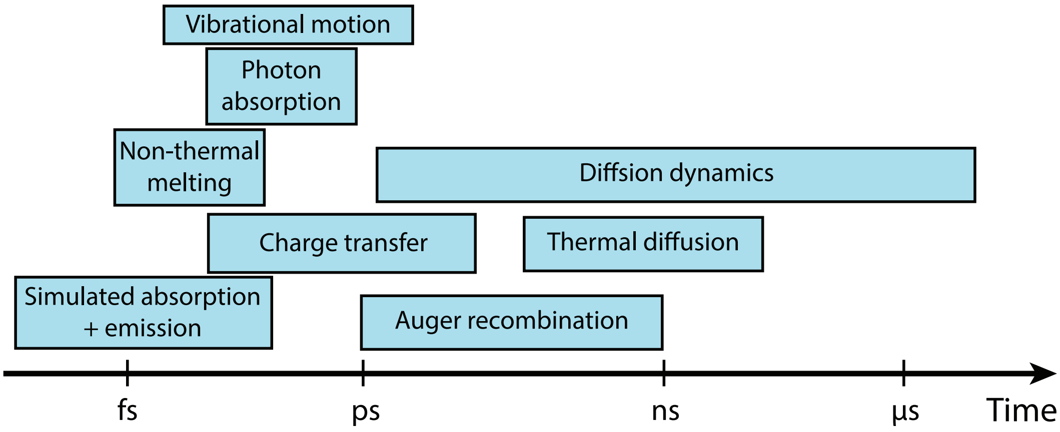

Figure 1.2: Overview of the timescales of various molecular processes.

1.3 Pump-probe techniques

In pump-probe experiments two beams usually are combined on the sample with a various delay time, enabling the investigation of ultrafast structural dynamics. It is possible to follow the time evolution of the electron density during the course of a photo-induced biological, chemical or physical transformation of the investigated system upon external excitation. The sample is illuminated with a first pulse, which changes the state of the system. The second pulse arrives to the sample after a time τ and probes the current state of the sample (see Figure 1.3). Dynamics of the system can be tracked by varying the delay time τ and obtaining scattering patterns from the sample by fast detectors [47].

Nowadays for various investigations X-rays can be combined with laser and terahertz pulses. For instance, with an optical laser it is much easier to change the incident angle and the delay time from the femtosecond range up to several nanoseconds. Pump-probe techniques with using a laser pump and X-ray probe beam were performed using vacuum

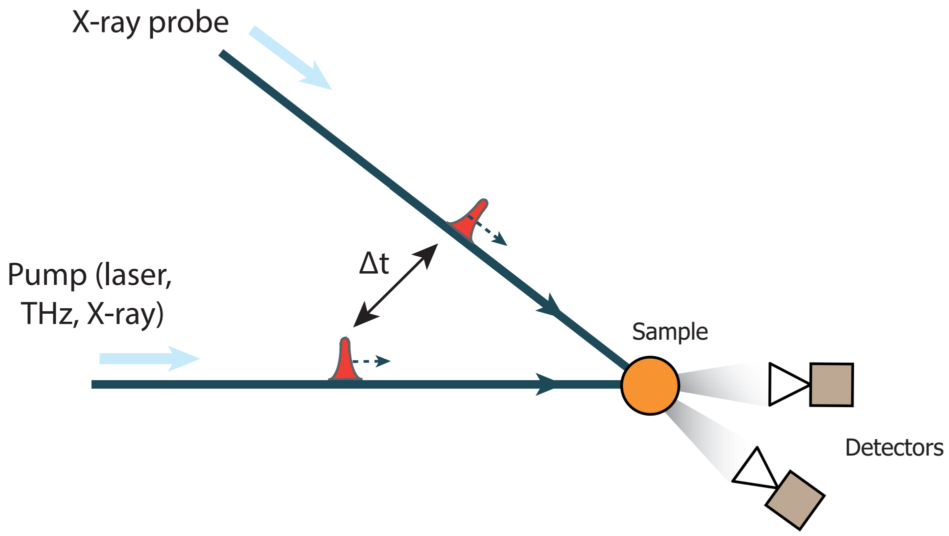

Figure 1.3: Sketch of a pump-probe experiment with a delay time Δt between two pulses.

ultraviolet (VUV) as a pump and FEL radiation as a probe in 100 fs range [48, 49]. It became possible for the first time to access the ultrafast times and nanometer length scales simultaneously [50].

A terahertz pump pulse is usually generated by a THz undulator in order to provide coherent femtosecond or picosecond (ps) pulses [51]. As an example the investigation of two-photon double ionization (TPDI) processes using the THz field is possible.

X-ray pump X-ray probe methods are a special way to collect time-dependent structural information about the sample [52] with a resolution determined by the pulse length and the device, which produce the delay time.

1.4 Ultrafast Photon Correlation Spectroscopy

Modern studies of material dynamics require not only static or time-average methods but also measurements of dynamics on various timescales. Photon correlation spectroscopy (PCS) can provide this information by observing fluctuation dynamics on length scales down to atomic sizes at timescales down to microseconds and below. X-ray Photon Correlation Spectroscopy (XPCS) is a coherent X-ray scattering technique used to study nanoscale dynamics by means of observing time-dependent changes in the speckle pattern [53]. XPCS has significantly contributed to understanding of nanoscale dynamics in various disordered systems, such as colloidal suspensions, crystals or magnetic systems [54]. Figure 1.4 shows the spatio-temporal range in the condensed matter science, which can be studied using the XPCS method.

However, the application of XPCS is limited at synchrotron sources by the available coherent photon flux and by the performance of X-ray detectors (i.e. frame rate,

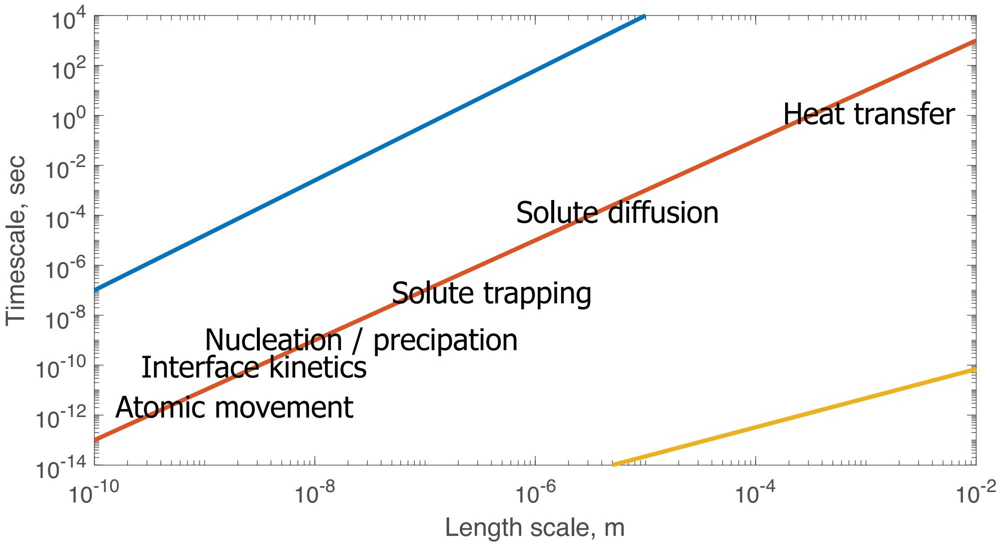

Figure 1.4: Length and time scales of the processes in condensed matter science, which can be studied by the XPCS technique. Solid lines show a typical timescales for diffusion processes such as interstitial or vacancy diffusion (blue) or diffusion in liquids (red). The speed of light is shown by the yellow line.

single-photon sensitivity, readout time, pixel size). Currently the fastest timescale obtained with XPCS at the state-of-the-art synchrotron sources is in the range of sub-microseconds.

With the development of diffraction-limited storage ring sources, the availability of much larger coherent flux will allow to probe dynamics down to the picosecond timescale. However, the timescales will be still limited by the frame rate of the available detectors. Due to the higher coherent flux, FELs offer the possibility to study dynamics on a timescales that are longer than the pulse repetition rate of the FEL assuming a suitable detector catches speckle pattern for every pulse.

The feasibility of performing XPCS scattering experiments on radiation sensitive soft-matter materials at FEL sources has been recently demonstrated [55]. In order to overcome temporal limitation and access faster timescales X-ray Speckle Visibility Spectroscopy (XSVS) can be used.

XSVS was originally developed in the visible-light region [56, 57]. In XSVS the dynamic information of the speckle patterns are obtained by analyzing the speckle statistics and calculating the speckle contrast in single scattering pattern as a function of exposure time. When scatterers move during the exposure time the speckle pattern is blurred thus speckle contrast decreases. Several studies [58–61] demonstrated the performance of XSVS at synchrotron sources. At FELs, the X-ray pulse duration (∼100 fs) is shorter than the acquisition time of currently available 2D modern detectors. An XSVS can be performed at FELs by changing the X-ray pulse duration. The XSVS experiment on liquid water, recently performed at LCLS, has demonstrated the performance of XSVS to study femtosecond dynamics [62].

XPCS with two pulses is based on the generation of two identical X-ray pulses with time separation shorter than the integration time of the detector [63]. Recently, the first split-and-delay experiment has been demonstrated by studying the diffusion of nanoparticles in the nanosecond regime [22].

1.5 Double pulse generation

Accelerator and optical based (split-and-delay) techniques are currently available to provide double pulses at FEL sources. Accelerator-based techniques manipulate the electron bunch or produce multiple controlled bunches. One of the methods is utilizing a thin piece of slotted aluminum foil at a dispersive section of the accelerator where the electron beam energy is correlated to the horizontal dimension. The foil can be used to spoil the portion of the bunch that interacts with it. Only the electrons that travel through the slots contribute to the lasing. The pulse durations in this method can be tuned by varying the slot widths [64].

Another method, called as split-undulator scheme, is a default two-color generation method for FEL sources [65,66]. In this method undulators are divided into two sections tuned to slightly different photon energies. Two pulses of different photon energies are emitted in undulators while a variable time delay between the pulses is introduced a magnetic chicane placed between the undulators. The chicane delays electrons of the second radiation pulse with respect to the first X-ray pulse.

Double pulse generation can be achieved by the double bunch operation of the accelerator at femtosecond, picosecond or nanosecond timescales. The basic principle of this method is that two electron bunches with a picosecond delay are generated at the cathode [67]. They are accelerated and compressed in the linac generating two bunches of different energies with a final delay on the fs/ps/ns timescales. This scheme overcomes the power limitations of the split undulator and has a wider application perspective. All timescales of the aforementioned methods are shown in Figure 1.5 together with the achievable time delays of SDL techniques.

Split-and-delay line devices currently operate with soft and hard X-rays [68]. First devices have been built for soft X-ray sources [69–71]. These devices are splitting and recombining FEL pulses using grazing incidence mirrors. This approach produces picosecond delay times between two pulses with attosecond time resolution.

The first hard X-ray SDL was designed and built at DESY [15, 16]. This device has a 90 degree scattering geometry design based on silicon Bragg crystals. The SDL idea was also pursued for the hard X-ray range at LCLS [17], SACLA [18, 19, 72] and the European XFEL [20, 21, 73, 74].

The SACLA SDL concept [72] is based on Si(220) Bragg crystals. The performance of the device was tested for energies from 6.5 keV to 11.5 keV. Split-delay optics throughput values of 12% and 7.4% were obtained for two branches of the SDL, respectively.

Recently the design of LCLS SDL device was reported [17]. This configuration uses a series of Si(220) crystal reflections in the horizontal scattering geometry. It covers an energy range between 6.5 and 13 keV, a delay range from -30 ps up to 500 ps at 8 keV. Reported parameters of the aforementioned SDL devices are listed in Table 1.2.

However, all of these devices are integrated into the beamline infrastructure and designed for a single FEL instrument. This thesis presents the compact hard X-ray SDL device, developed for use in any experimental hutch of any FEL instrument.

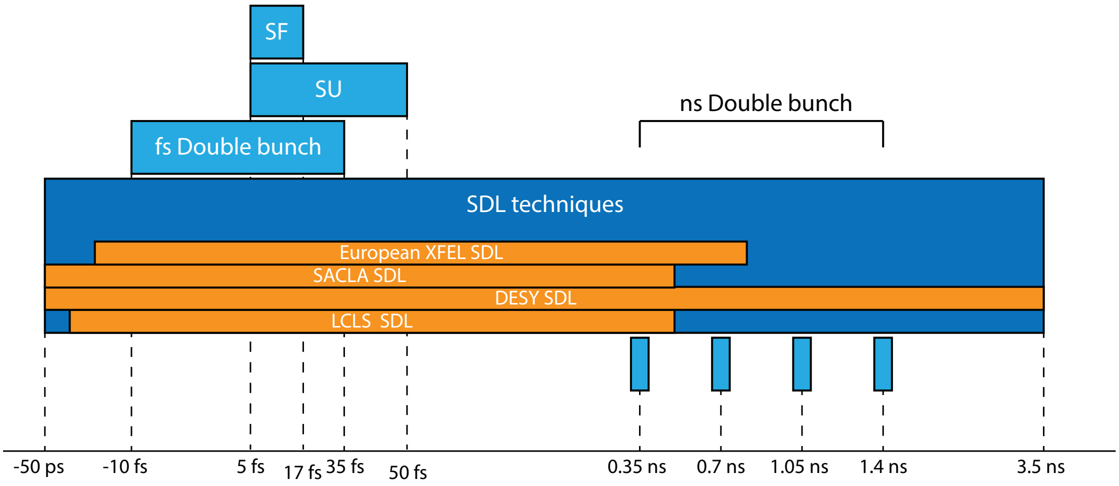

Figure 1.5: Time windows for double pulse techniques at FELs.

1.6 Outline

Chapter 2 contains a detailed conceptual design of the SDL. The main specifications and performance estimates of the device including calculations of its dimensions and throughput are presented. Chapter 3 presents the mechanical design of the SDL. Based on optical schemes a design of mechanical stages for crystal components is presented. Chapter 4 presents results of SDL experiments at synchrotron sources. The performance of the beam splitting optics was tested in X-ray topography measurements. The SDL optics was aligned using the laser-based time delay calibration setup. The expected performance of the setup was experimentally checked by measuring time delays at 7 keV and 9 keV photon energies. An outlook for future improvements of the setup is presented in Chapter 5. A conclusion on the SDL project is given in Chapter 6.

Facility	**Energy range, [keV]**	**Time delay range**	**Type of the beam splitting**
DESY, Germany [15,16]	8.39, 12.4	-1.4...3.5 ns	Amplitude
LCLS, USA [17]	6.5-13	-30...500 ps	Amplitude
SACLA, Japan [18,19]	6.5-11.5	-50...220 ps	Amplitude, Wavefront
European XFEL, Germany [20,21]	5-10	-10...800 ps	Amplitude, Wavefront

Table 1.2: Characteristics of SDL devices at various FEL facilites. Amplitude and wavefront division methods of the beam splitting are explained in Section 2.4.1

Chapter 2

Conceptual design of the compact Split-and-Delay Line

In this chapter the conceptual design of the compact split-and-delay line (SDL) is presented. A short introduction to the dynamical diffraction theory of X-ray diffraction is given in the first section. The SDL device requirements are discussed in the following section. Basic concepts of the setup are presented showing three configurations. The choice of optical components for the SDL device is discussed. The expected performance estimates of the SDL is given in the last section of the chapter.

2.1 Dynamical theory of the X-ray diffraction

The intensities observed in X-ray diffraction studies can be treated according to the kinematical or dynamical theory. The first one, kinematical theory was suggested by Darwin in 1914 [75] and treats the scattering from each volume element of the illuminated sample independently. The kinematical theory does not take into account multiple scattering effects inside the crystal. Therefore for relatively thick crystals the dynamical diffraction theory has to be used. The dynamical diffraction theory was first presented in the publication of Darwin [75] and further summarized in an article of Batterman and Cole [76] and books of Zachariasen [77], Pinsker [78] and Authier [79]. A basic introduction into the dynamical diffraction theory will be given here, which is necessary for understanding the latter parts of this thesis.

X-ray diffraction in a crystal occurs if the Bragg condition is fulfilled. This condition is valid only when the angle θ_B between the crystal net planes and the incident X-ray beam fulfills the expression

$$m\lambda = 2d\sin(\theta_B), \tag{2.1}$$

where d is a crystal interplanar distance and λ is the wavelength of the incident beam. The parameter m corresponds to the order of reflection. Figure 2.1 shows the diffraction scattering geometry in (a) reflection or (b) transmission, which are named Bragg and Laue geometries, respectively. In the current section the Bragg geometry will be discussed since this type of crystals is employed in the SDL setup.

Any electromagnetic wave propagates in the direction, defined by its wavevector $\mathbf{k}$ (see Figure 2.1). The length of wavevectors of incident and diffracted waves $\mathbf{k}$ and $\mathbf{k}'$ can be defined as

$$\|\mathbf{k}\| = \|\mathbf{k}'\| = 2\pi/\lambda. \tag{2.2}$$

When a photon with the wavevector $\mathbf{k}$ interacts with a particle and emerges from the collision with a different direction (i.e. scattered) its wavevector changes accordingly into $\mathbf{k}'$ [80]. The change in the wavevector is called the scattering vector $\mathbf{q}$ and defined as :

$$\mathbf{q} = \mathbf{k}' - \mathbf{k}, \tag{2.3}$$

Bragg diffraction takes place not only when the incident angle of the beam is precisely equal to the Bragg angle θ_B. There is an angular range $\Delta\theta$ around θ_B, given by the Darwin width (or rocking curve width) ω of the crystal. The Darwin width is the full width at half maximum (FWHM) of the total reflective profile of the crystal and it is equal to [81]

$$\omega = \frac{2r_e\lambda^2}{\pi v_c \sin 2\theta_B}\sqrt{b}|P|\,|F|\,e^{-M}, \tag{2.4}$$

where r_e is the electron radius ($r_e = 2.82 \times 10^{-5}$Å), the volume of unit cell is represented as v_c and parameter e^{-M} is the Debye-Waller factor. The polarization factor P is equal 1 or $\cos 2\theta_B$ for perpendicular (σ) and parallel (π) polarizations, respectively. The structure factor F is a mathematical function describing the amplitude and phase of

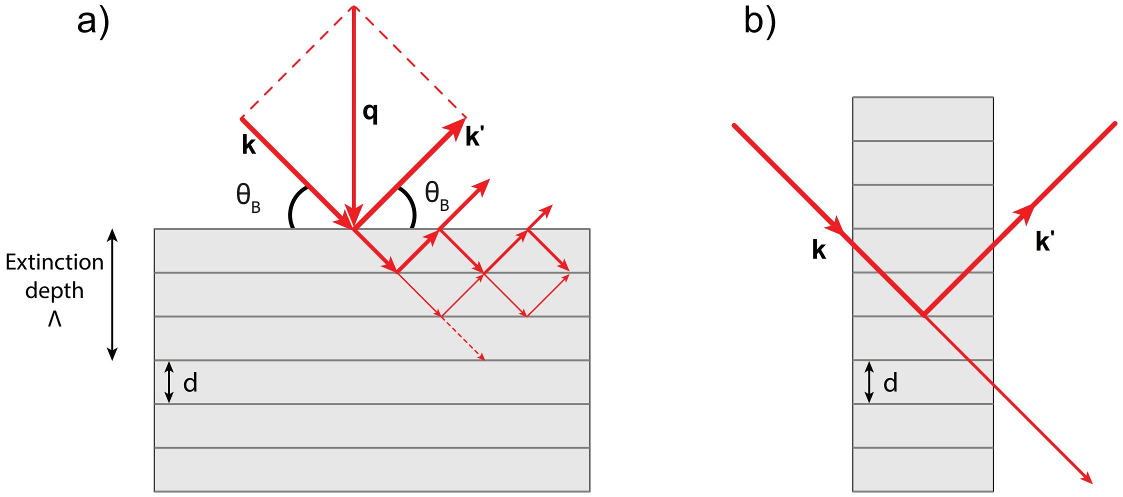

Figure 2.1: Diffraction by the thick perfect crystal in a) Bragg or b) Laue geometries with the lattice spacing d.

a wave diffracted from crystal lattice planes characterized by Miller indices h,k,l [82]. These indices are used to specify directions and planes in crystallography.

The parameter b in Equation 2.4 is the asymmetry factor defined by

$$b = \frac{\sin(\alpha + \theta_B)}{\sin(\alpha - \theta_B)}. \tag{2.5}$$

Here α denotes the angle between the crystal surface and the reflecting planes. For the symmetric Bragg reflection $b = -1$ (i.e. $\alpha = 0$).

Due to refraction the center of the rocking curve is shifted from the Bragg angle θ_B by [79]

$$\Delta\theta_i = \frac{1}{2}(1 - b)\Delta\theta_{os} \tag{2.6}$$

$$\Delta\theta_e = \frac{1}{2}\left(1 - \frac{1}{b}\right)\Delta\theta_{os} \tag{2.7}$$

for the incident θ_i and reflected θ_e beam. The angle θ_{os} in Equations 2.6 and 2.7 is

$$\Delta\theta_{os} = \frac{1}{\sin 2\theta_B}\frac{r_e\lambda^2 F}{\pi v_c}. \tag{2.8}$$

For the symmetric reflection in Bragg geometry $\Delta\theta_e = \Delta\theta_i = \Delta\theta_{os}$. Figure 2.2 illustrates the asymmetric Bragg crystal geometry when the surface normal is neither parallel nor perpendicular to the lattice planes $b \neq \pm 1$.

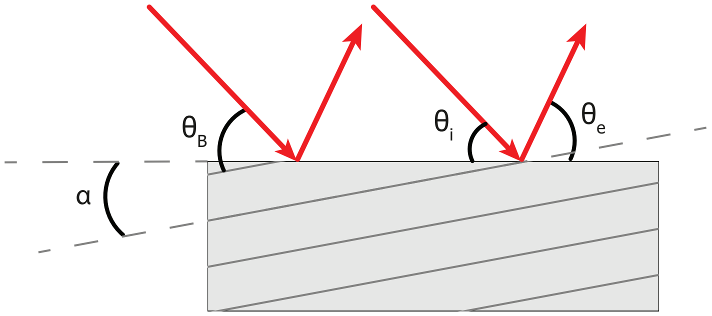

Figure 2.2: Bragg crystal diffraction in the asymmetric scattering geometry. The incident and exit angles are denoted by θ_i and θ_e, respectively. The Bragg angle is marked by θ_B.

While an X-ray beam penetrates into the crystal it becomes weaker after each atomic layer since some photons are scattered every time they pass through a plane of atoms. Propagating through the crystal the primary beam becomes more and more attenuated. This effect is known as a primary extinction [77]. For a finite size crystal the evolution of the wave field and, consequently, the extinction process depend on the diffraction geometry. When the Bragg condition is satisfied the extinction depth Λ is defined as

$$\Lambda = \frac{1}{4}\left(\frac{m}{d}\right)\frac{v_c}{r_e|F|}. \tag{2.9}$$

Figure 2.3 a) shows an example of the reflectivity curve from the Si(111) crystal with a thickness of $L = 100\Lambda$, calculated according to the dynamical theory of diffraction at the photon energy $E = 8\ keV$. The crystallographic planes are assumed to be parallel to the crystal surface. In this specific case the effective attenuation distance for X-rays upon the dynamical diffraction is represented by the extinction depth $\Lambda = 1.72\,\mu\mathrm{m}$ (see Equation 2.9). In the angular range $\Delta\theta = \theta - \theta_B$, the reflectivity curve

$$R(\Delta\theta) = \left.\frac{E_h(z,\Delta\theta)}{E_0(z,\Delta\theta)}\right|_{z=0} \tag{2.10}$$

have a sharp asymmetric peak with the maximum of the order of unity in modulus. Here parameters E_0 and E_h correspond to the amplitudes of electric waves which are propagating along the directions of transmission and diffraction, respectively.

Depending on the lattice orientation in crystals, the Darwin width ω (see Equation 2.4) varies as it shown in Figure 2.3 (b).

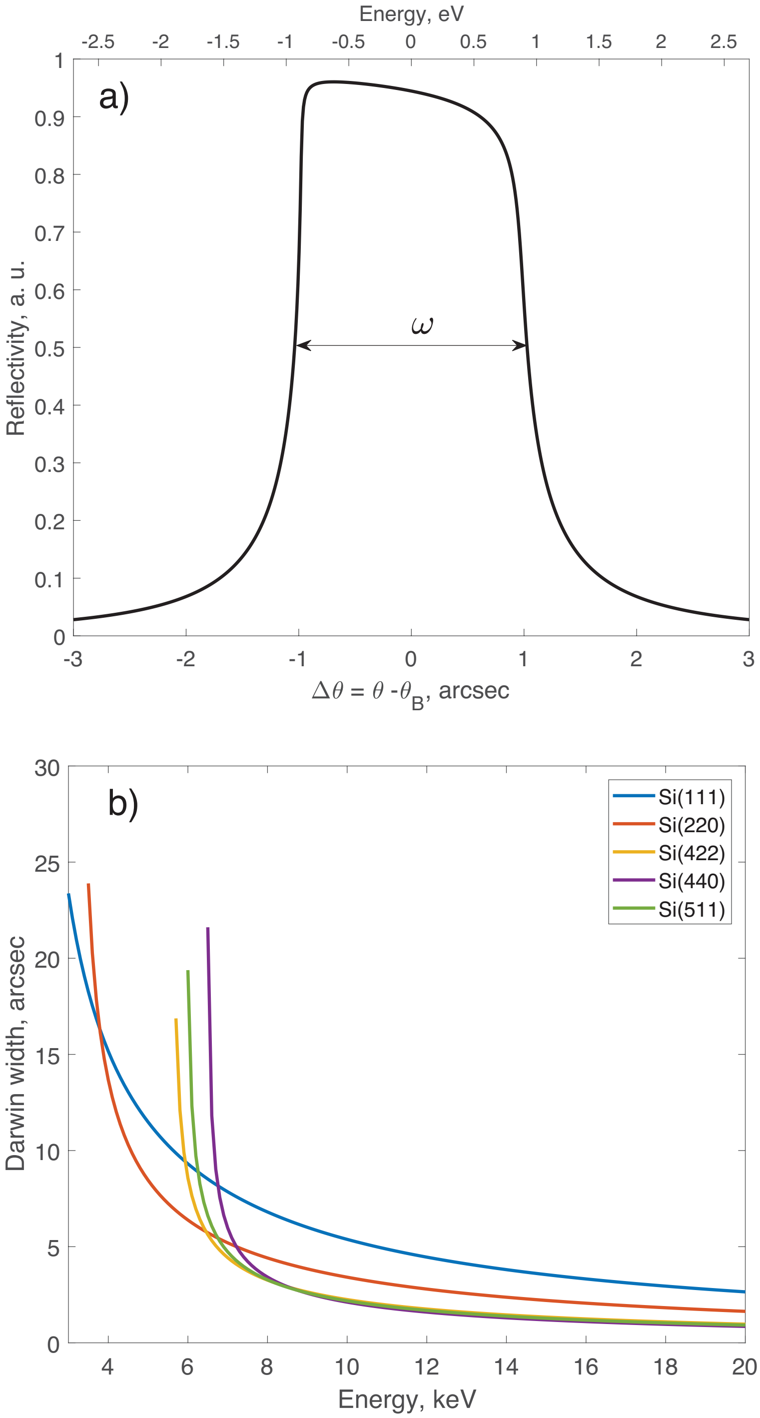

Figure 2.3: (a) Normalized Si(111) reflectivity curve at E=8 keV and (b) the comparison of typical Darwin widths for the Bragg crystals with the different h,k,l indices. The Darwin width distribution $\omega(E)$ is shown only for the limited hard X-ray energy range of $3 < E < 20$ keV.

2.1.1 X-ray topography

X-ray topography is a non-destructive technique for imaging the defects and strain fields in crystalline materials via X-ray diffraction [83–85]. Topographic images (topograms) can be taken in transmission (Laue geometry) or reflection (Bragg geometry) mode (see Section 2.1) by registering the intensity distribution of the diffracted beam from an investigated crystal. The intensity distribution of the diffracted beam from a perfect crystal is always homogeneous. Defects and strain fields result in lattice deformation inside the crystal, causing variations in the diffracted intensity on the resulting diffracted intensity distributions. The X-ray topography is used for visualization of such defects as dislocations, twins, domain walls, inclusions, impurity distributions, that can be present in the crystal volume [86].

The basic principle of X-ray topography is shown in Figure 2.4. In this example, a crystal with lattice defects is oriented in such a way that the Bragg condition is fulfilled. The intensity distribution of the diffracted beam is changing corresponding to the defects allocation. The crystal areas which are not affected by the strains are fully diffracting the beam in the Bragg condition. Defects are transforming the lattice which leads to the decrease of the diffracted intensity. A rather low intensity of the diffracted beam can be observed in the corresponding topogram regions.

For X-ray topography measurements either a mono- or a polychromatic beam can be used. When using a monochromatic beam, only one topogram can be recorded at a time due to the presence of only a single Bragg condition. A set of topograms can be recorded simultaneously when using a polychromatic beam for a multiple Bragg angles. There will be at least one wavelength in the incident spectrum present, for which the Bragg condition for a certain set of lattice planes will be fulfilled.

There are two different kinds of contrast that can be identified on the topographic image: orientation contrast and extinction contrast [87]. Orientation contrast is based on the Bragg law and arise when a part of the crystal crystallographically perfect but misoriented with respect to the rest of the crystal so that the Bragg condition is not fulfilled. Therefore, no diffraction from this part of the crystal will be present. Extinction contrast arises from the scattering power (integrated reflectivity) of crystallographically imperfect regions of the crystal.

Orientation contrast topography maps of the Bragg crystal can be obtained by performing the topography measurements in the angular range $\Delta\theta$ close to the Bragg angle. Thus, an intensity distribution over the angle will result in the Bragg curve of the crystal, registered by every pixel of the detector separately. Such scan of the crystal allow to measure the full-width at half-maximum (FWHM) and shift in the peak position across the crystal. The rocking curve peak position and its FWHM can be correlated, for instance, with local defects or lattice strains.

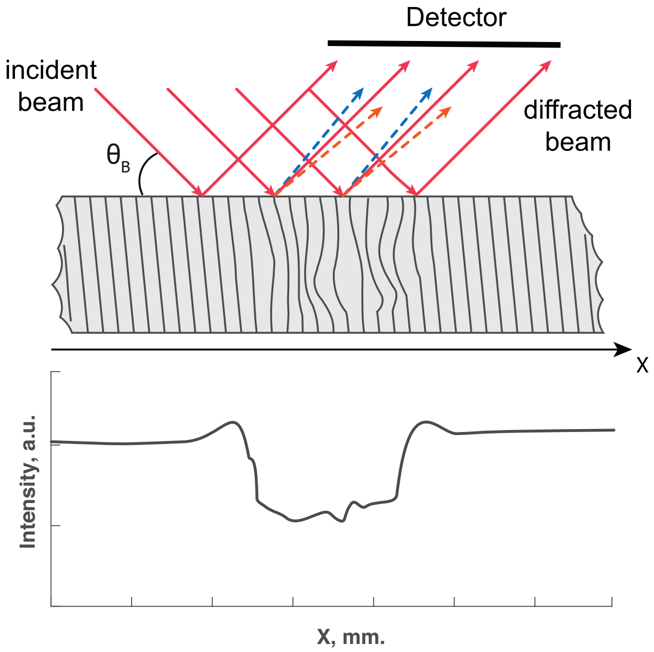

Figure 2.4: Sketch of the basic X-ray topography principle. The incident beam is diffracted with an intensity distribution which depends on the lattice structure. Red and blue arrows represent a diffracted waves at the different incident angle.

2.2 Requirements for the compact Split-and-Delay Line

The compact SDL is designed to perform jitter-free X-ray pump X-ray probe (see Section 1.3) and XPCS experiments (see Section 1.4), where the time resolution is determined not by the photon source but by the SDL setup.

In order to set the operational parameters and technical capabilities of the SDL basic requirements and functionality of the device should be defined. The most important parameter is the achievable delay time range. The SDL application is employed to cover the time gap between two successive FEL pulses. The European XFEL facility in Hamburg (see Table 1.1) is able to provide a pulsed X-ray radiation with a maximum repetition rate of 4.5 MHz [4]. Figure 2.5 shows the default time structure of the source. This facility provide pulse trains with the repetition rate of 10 Hz. Each train contains up to 2700 pulses per train [4]. However, the faster timescales could be accessed by operating the LINAC in custom modes where electron bunches with the smaller separation could be generated. The minimum expected delay of 769 ps between two

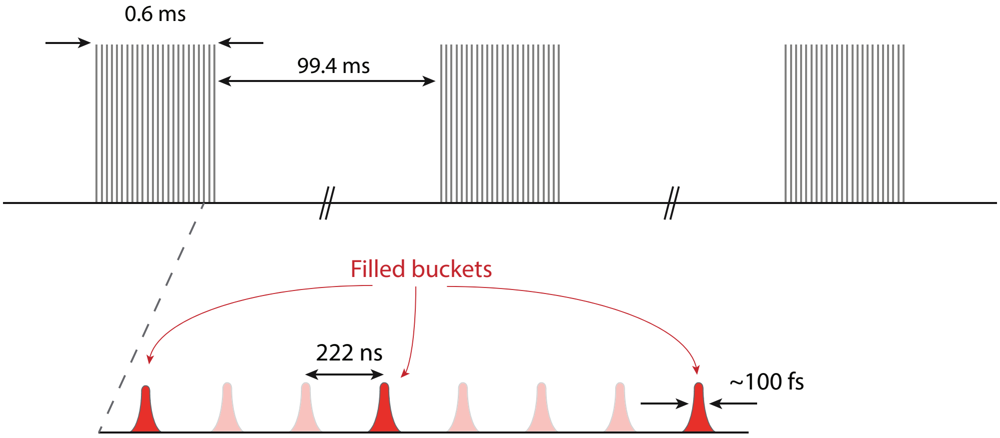

Figure 2.5: Time structure of the European XFEL with 2700 pulses at 4.5 MHz (within a pulse train) and an overall 10 Hz train repetition rate.

successive pulses can be obtained by filling the empty buckets in 1.3 GHz RF cavities generation mode [4]. For ultrafast experiments it is highly necessary to have a device which gives a possibility to access delays in this timescales with a flexible time delay.

In order to have high flexibility on the types of conducted experiments and preserving the maximum flux at the sample, the SDL should be placed as close as possible to the sample. In this case a stability of the beam at the sample position is less critical since the beam path after SDL is minimized (see Figure 2.6). Sample environment can be also included to the setup as one of the components. Overall the device dimensions must be compact (less than 1 m in every dimension) for reliable transportation and quick mounting. Moreover, the SDL should be able to operate in vertical and horizontal orientations to minimize throughput losses affected by incident beam polarization. In order to match aforementioned demands the main design criteria for developing an SDL are summarized below:

- Applicability for X-ray pump X-ray probe and double pulse XPCS experiments
- Achievable delay times 0 ns< τ <1 ns
- Picosecond time resolution
- Compact and portable device dimensions
- Hard X-ray operating energy range (>5 keV)
- Minimizing the number of optical components to achieve maximum throughout

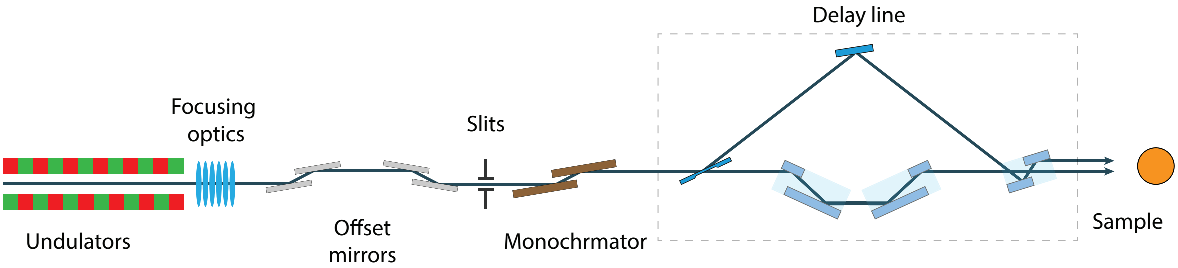

Figure 2.6: Sketch of the SDL positioning during FEL experiments.

2.3 Basic concept

The concept of the SDL design is based on symmetric Bragg reflection geometry. A basic scheme shown in Figure 2.7 consists of two Bragg optical components: the beam splitter (BS) and the beam reflector (BR). The incoming X-ray pulse is split by the BS into two fractions, which are propagating along fixed- and variable delay branches, respectively. The fixed-delay branch is a geometrical path of the beam which is transmitted by the BS and defined by length L_1. The variable-delay branch is a geometrical path of the beam, diffracted by the BS, respectively. The optical path of the variable-delay branch is defined by $L_{21} + L_{22}$. In order to achieve the intersection between two branches the BR must have a higher order of reflection than the BS (e.g. Si(111) crystal as a BS and Si(220) as a BR crystal).

In order to change the delay time τ, crystals BS and BR must be moved to the sample along the directions shown in Figure 2.7. Ultrafast experiments are typically sensitive to the movement of the sample during the investigation. Thus in the designed

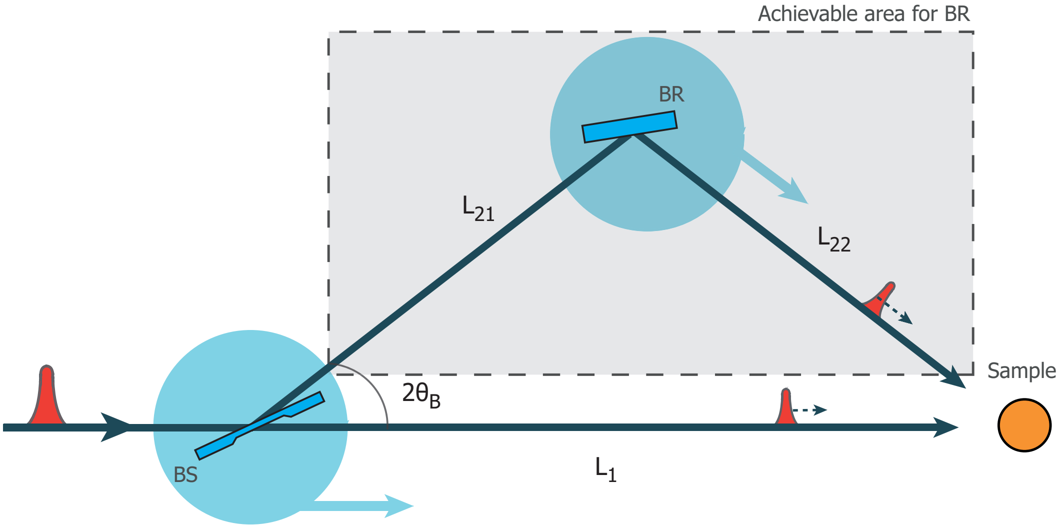

Figure 2.7: A basic scheme of SDL with BS and BR crystals in the Bragg geometry.

scheme a sample is fixed and the crystals are moved relatively to change the time delay between split pulses. Time resolution is limited only by the precision of motors and stability of the entire system. Achievable maximum delay times are limited by the dimensions of the SDL setup.

The achievable delay time τ for the introduced scheme can be calculated as

$$\tau = \frac{L_{21} + L_{22} - L_1}{c}, \tag{2.11}$$

where c is a light speed.

The scheme shown in Figure 2.7 has an advantage of generating the delay time using only two crystals. However, in order to reach zero delay time between split pulses, the first SDL scheme can be modified by adding the channel-cut module CH1 (see Figure 2.8). This module consists from two pairs of crystals and can be mounted in the fixed-delay branch to shift the delay time range to ”near-zero” timescales. This configuration can be used for ultrafast FEL experiments, which require femtosecond to few picoseconds (< 10 ps) time range. Depending on the required delay time range channel-cut optics can have the different order of reflection and the distance between

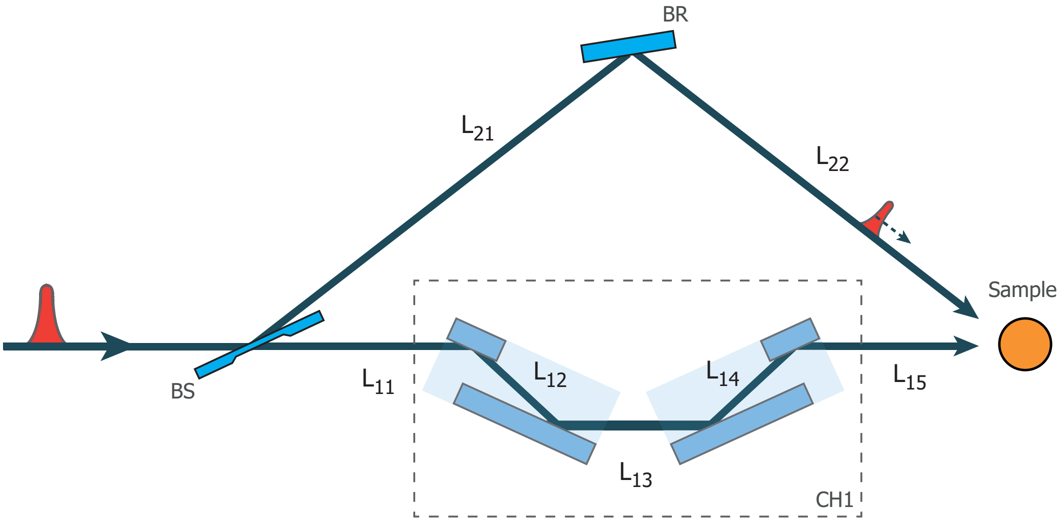

Figure 2.8: The SDL scheme with a channel-cut module CH1 in the fixed-delay branch.

crystals in each pair. In this crystal configuration the delay time is defined by

$$\tau = \frac{(L_{21}+L_{22})-(L_{11}+L_{12}+L_{13}+L_{14}+L_{15})}{c}. \tag{2.12}$$

In addition to the CH1 configuration, a crystal set CH2 can be also implemented (see Figure 2.9). The additional crystal pair in a variable-delay branch can provide two parallel beam fractions at the output of the SDL. Double pulse experiments such as X-ray photon correlation spectroscopy [88] can be enabled in this mode. Together with CH1 and CH2 modules the total delay time is

$$\tau = \frac{(L_{21}+L_{22}+L_{23}+L_{24})-(L_{11}+L_{12}+L_{13}+L_{14}+L_{15})}{c}. \tag{2.13}$$

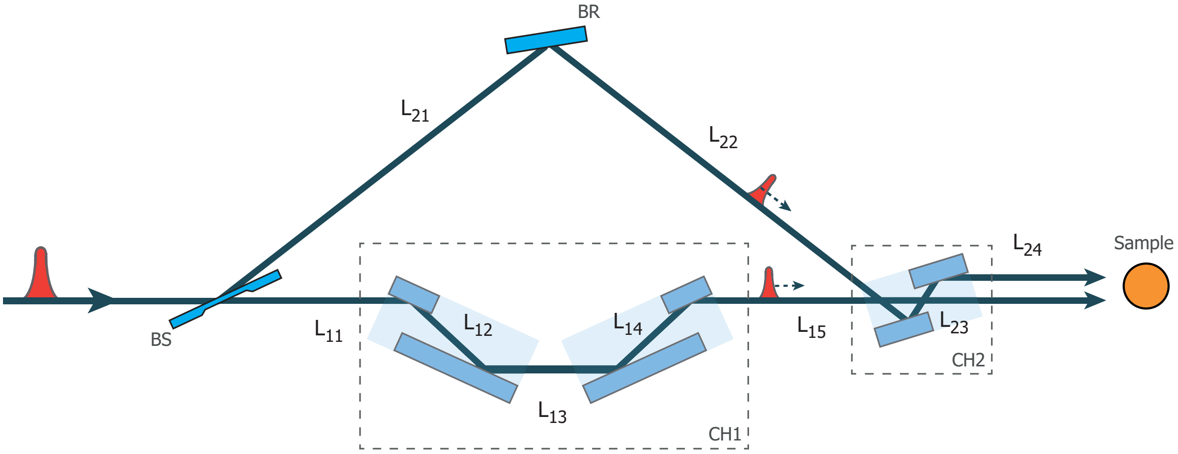

Figure 2.9: The SDL concept scheme with additional modules CH1 and CH2.

2.4 Crystal optics

The optical components of the SDL should guarantee first of all high transmission, wide energy tuning range and good stability of the X-ray beam. Optical elements for hard X-ray energies follow different operating principles, compared to conventional visible light optics. They use the diffraction as a mechanism for changing the direction of the beam. Most common optical components for X-rays are mirrors, used in grazing incidence close to the critical angle [89]. Also a concave spherical mirrors at the grazing angles are used to focus the beam in one direction. However, the Bragg crystals can be used to achieve high reflection angles in hard X-ray range.

Bragg X-ray optics is usually fabricated to serve numerous purposes on synchrotron beamlines such as monochromators, mirrors and focusing elements [90, 91]. Silicon, diamond and germanium are the most suitable materials to use for the X-ray beam diffraction [92]. Thermal properties of these materials are listed in the Table 2.1 [93].

The peak reflectivity of diamond is certainly higher among others and this material has higher temperature stability. This implies that less heat per unit volume is absorbed which makes diamond more suitable for high power X-ray beams.

Despite of the better thermal stability of diamond, a preferable candidate for Bragg crystals in the SDL design is silicon. It is cheap and easy to manufacture, resulting in the perfect crystalline structure on the atomic scale [94]. Nowadays, technologies of machining advanced crystal shapes and etching of silicon are widely developed due to the high demand in silicon optics for the X-ray sources.

	Si(111)	**Ge(111)**	**D(111)**
$\boldsymbol{a}$**,** Å	5.43	5.65	3.56
κ at 300 K ($\times$10^{-6}), K^{-1}	2.60	5.90	1.00

Table 2.1: Lattice parameters a and linear thermal expansion coefficients κ for silicon, germanium and diamond.

2.4.1 Beam splitters

The beam splitter is the key component of the SDL. Efficient operation of the device strongly relies on the quality of beam splitting optics. Beam splitters, used in the hard X-ray regime, can be classified into three types: mirror-based geometrical splitters [95], grating-based splitters [96], and crystal-based Bragg splitters [71, 97]. The last type provides high reflection angles comparing to grazing mirrors or gratings. There are two mechanisms of dividing the X-ray beam using the Bragg crystal: wavefront [98] and amplitude division [16].

Wavefront division is a method of dividing the wavefront of the incident beam. Splitting is achieved by inserting a sharp crystal edge to the beam is it shown in Figure 2.10 a). To obtain a high quality of the diffracted beam the crystal must be polished with a high perfection, making a sharp beam division. This kind of splitters

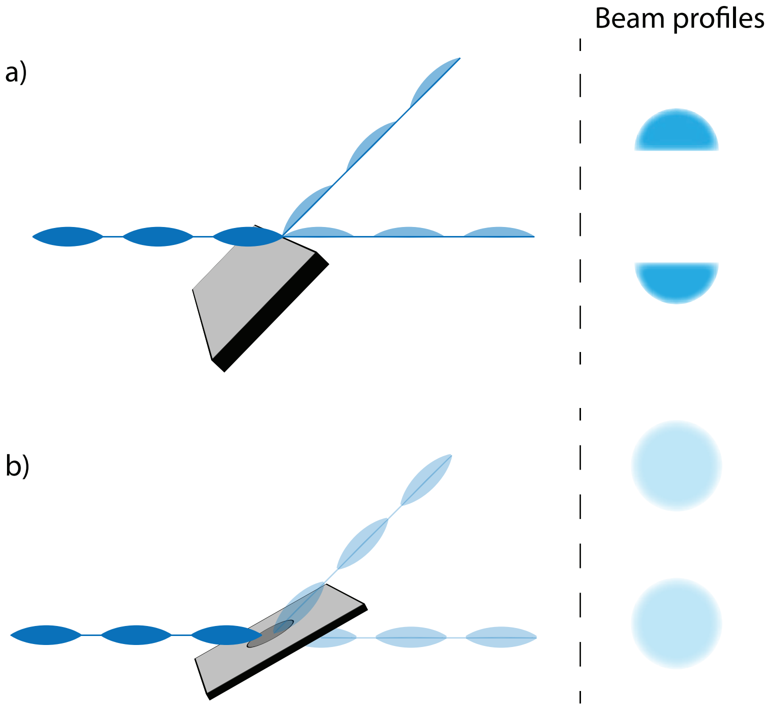

Figure 2.10: Types of beam splitting.

are sensitive to the pointing stability of the incident beam. The 1:1 splitting ratio is achieved only when the wedge split the incident beam into two beams which have the equal area of the beam profile.

Amplitude division is a method to divide the incoming pulse into two fractions, preserving its size and shape. A thin Bragg crystal split the beam into two fractions dividing the incident intensity as it shown in Figure 2.10 b). Splitting ratio given by this technique is related to a beam splitter thickness and not affected by FEL beam fluctuations.

The concept (see Section 2.3) allows SDL to operate using both types of beam splitters. However, the amplitude division is chosen as the most efficient method for current SDL design. Much progress with the fabrication of amplitude beam splitters was achieved using Plasma Chemical Vaporization Machining (PCVM) [97]. A sketch of such a splitter is shown in Figure 2.11. It has a very high crystalline quality (crystal roughness < 0.2 nm rms.) with a sufficiently thin ($< 15\,\mu\text{m}$) uniform splitting area [99].

During the diffraction an incoming intensity is partially absorbed transmitted and

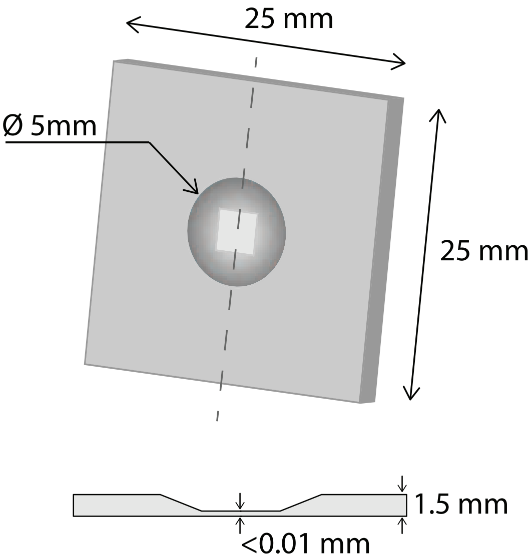

Figure 2.11: Drawing of the thin PCVM crystal.

diffracted. The corresponding intensities I$_a$, I$_t$ and I$_r$ can be calculated as a function of crystal thickness [100]. These values are related to the intensity of the input beam I_0 as:

$$I_0 = I_a + I_r + I_t, \tag{2.14}$$

Following this approach [100, 101], a distribution of the intensity values are shown at Figure 2.12. The intersection point of the transmission and reflection curves is corresponds to 1:1 splitting ratio. This ratio can be changed by varying the crystal thickness.

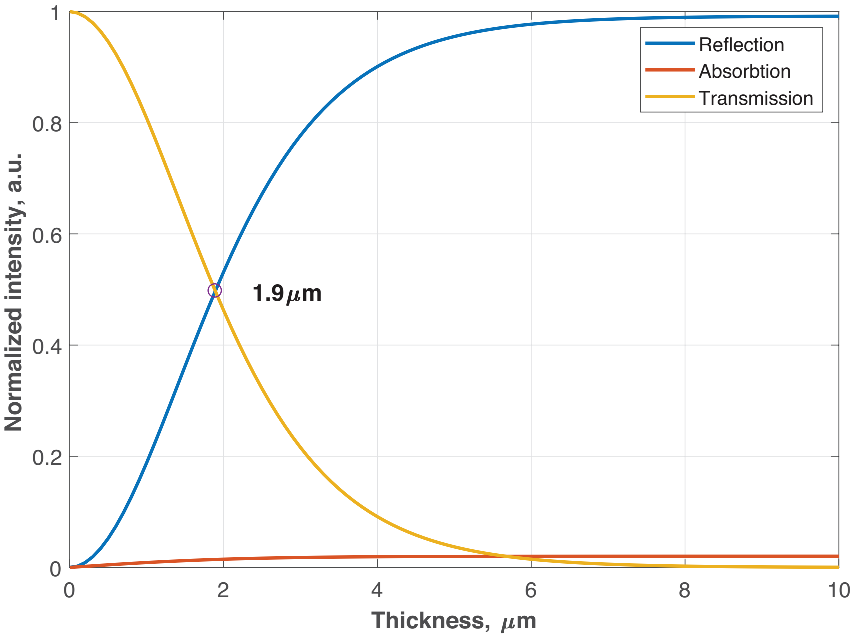

Figure 2.12: Transmitted, reflected and absorbed intensities of 8 keV beam at the Si(220) thin beam splitter as a function of the crystal thickness.

2.4.2 Bragg crystals

Bragg silicon crystals are employed for a beam guiding inside the SDL. X-ray diffraction from bulk single crystals can be described by dynamical theory of the X-ray diffraction (see Section 2.1). Darwin curves of Si(111) are depicted in Figure 2.13, representing the diffracted intensity by a Si(111) crystal at the photon energies 8 keV, 12 keV and 15 keV. Due to refraction the center of the curve is shifted from the Bragg angle. The Darwin width ω is the FWHM of this curve. Bragg angle θ_B changes with the energy as it shown on the Figure 2.14.

The integrated intensity of the Darwin reflectivity curve R_{int} is given by integrating the diffraction profile over the entire angular range.

$$R_{\text{int}} = \int_{-\infty}^{\infty} R(\theta) d\theta. \tag{2.15}$$

The maximum value of the curve is called peak reflectivity R_{max}. The distribution of R_{max} over the hard X-ray energy range shown in Figure 2.15.

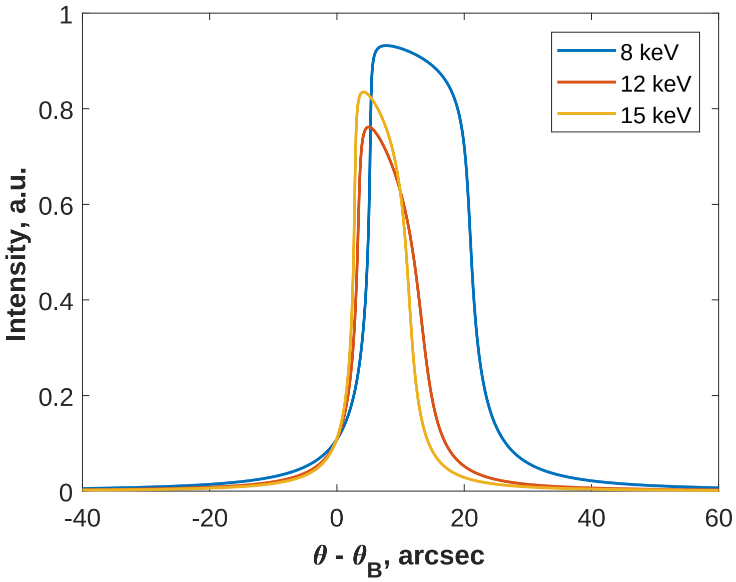

Figure 2.13: Reflection curves of Si(111) in the symmetric Bragg case

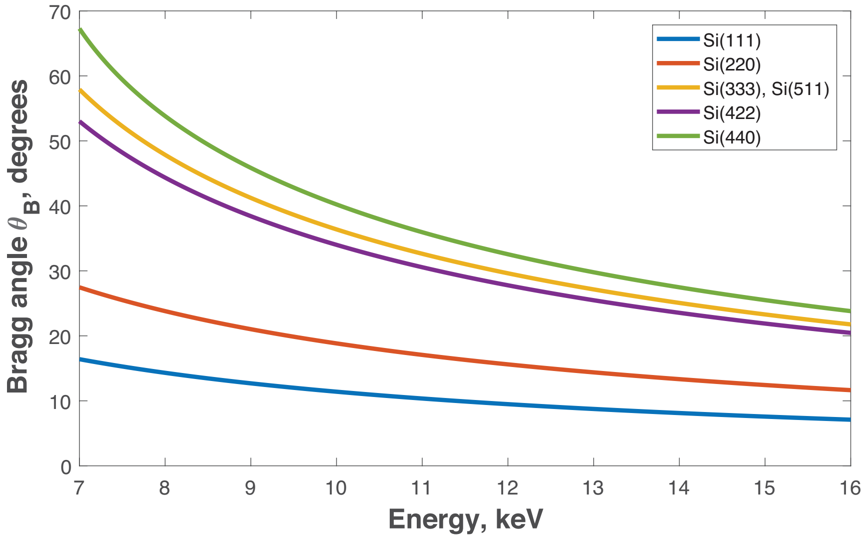

Figure 2.14: Bragg angle θ_B of the Silicon crystals in the 7-16 keV energy range

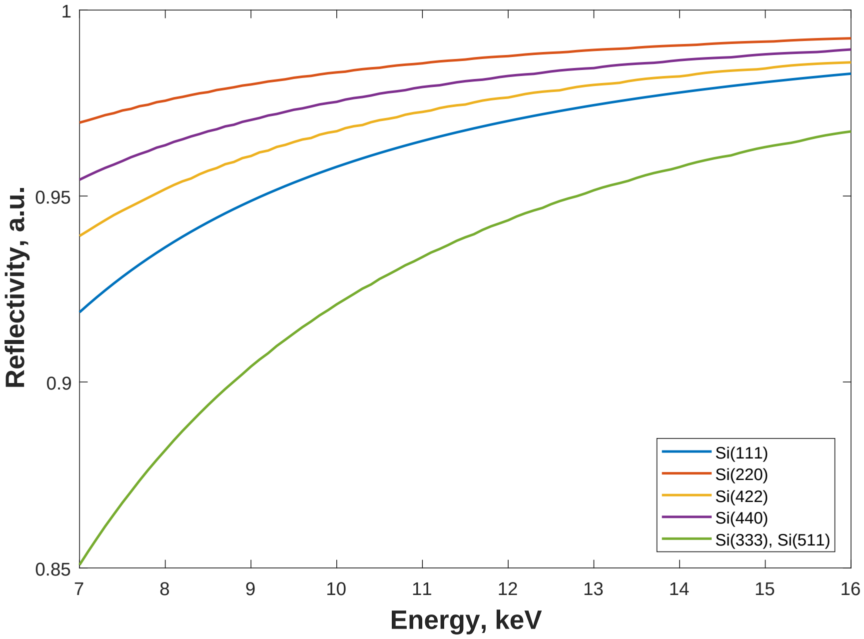

Figure 2.15: Perfect crystals reflectivity R_{max} at the range of energies 7-16 keV

Reflectivity parameters of silicon, diamond and germanium crystals for various *h*,*k*,*l* indices are listed in the Table 2.2. A crystals with the higher energy resolution must be implemented to the SDL setup in order to maximize the throughput. For the BS and BR optics a crystals with different Miller indices must be employed. Si(111), Si(220) and Si(422) optics is chosen for the SDL device to use in pairs, where BS crystal have lower indices than the BR crystal.

Diamond and germanium can be still considered as a materials for the future development and improvement of the SDL device (see Section 5).

Miller indices (hkl)	**$\Delta E/E$, ($\times 10^{-5}$)**	**ω, arcsec**	**Peak intensity R_{max}, a.u.**	**R_{int}, a.u.**
Silicon				
111	14	5.8	0.96	32.8
220	6	4.2	0.98	24.3
422	1.5	2	0.97	11.4
511	0.9	1.3	0.92	7.2
Germanium				
111	31.7	12.7	0.95	69.1
220	14.1	9.5	0.98	53.3
422	3.2	2.8	0.96	23.8
511	1.9	1.5	0.91	14.8
Diamond				
111	6.2	4	0.997	24.3
220	2	2.4	0.998	14.3
422	0.5	1.6	0.996	9.5
511	0.3	1.2	0.991	7.3

Table 2.2: Energy resolutions $\Delta E/E$, Darwin widths ω, peak reflectivity R_{max} and the integrated normalized intensity R_{int} for various Bragg crystal materials and lattice orientations [102]. Listed values were calculated using the photon energy E=10 keV.

2.5 Performance estimates

In Section 2.3 a geometrical scheme based on the Bragg diffraction was presented. Delay times, generated by the SDL, can vary depending on the distance between the sample and the BS crystal. Thus the delay times are limited only by the physical dimensions of the device. The SDL dimensions (width W and length L) are chosen $W = L = 60$ cm as proposed values for portability and flexible transportation.

Si(220) and Si(422) optics is chosen for the BR crystal. For the CH1 module, a pair of Si(220) channel cut crystals is implemented. They have a 10 mm channel cut gap and mounted on the separate goniometer stages. Such dimensions are the most compact option for the Bragg angles θ_B in the energy range of 7-16 keV, covering the range $7.5° < \theta_B < 44.3°$. This gives up to 244 mm path length difference and corresponds to the maximum achievable time delay in the aforementioned SDL dimensions.

The delay times and throughput are calculated for the each configuration (see Section 2.3). In hard X-ray energy range from 7 keV to 16 keV the achievable delay times between two successive FEL pulses are -5 ps $< \tau <$ 815 ps. A short time delays from -5 ps up to 179 ps are available with the Si(111)-Si(220) crystal configuration (BS-BR) and using the CH1 and CH2 modules. Longer delay times can be achieved without the channel-cut CH1 and using two-crystal configuration, i.e. Si(111)-Si(220) or Si(220)-Si(422) optics for the BS-BR crystals, respectively. Figure 2.16 shows calculated delay time ranges for two SDL configurations, which are covering the whole delay time range.

A Si(111)-Si(220) BS-BR crystal pair is employed together with the Si(220) as the CH1 and Si(220)-Si(111) as the CH2 channel cuts. A time delays interval of 47 ps $< \tau <$ 179 ps can be achieved by using only the Si(111)-Si(220) BS-BR combination. The channel cut CH1 with Si(220) crystal pair in a fixed-delay branch

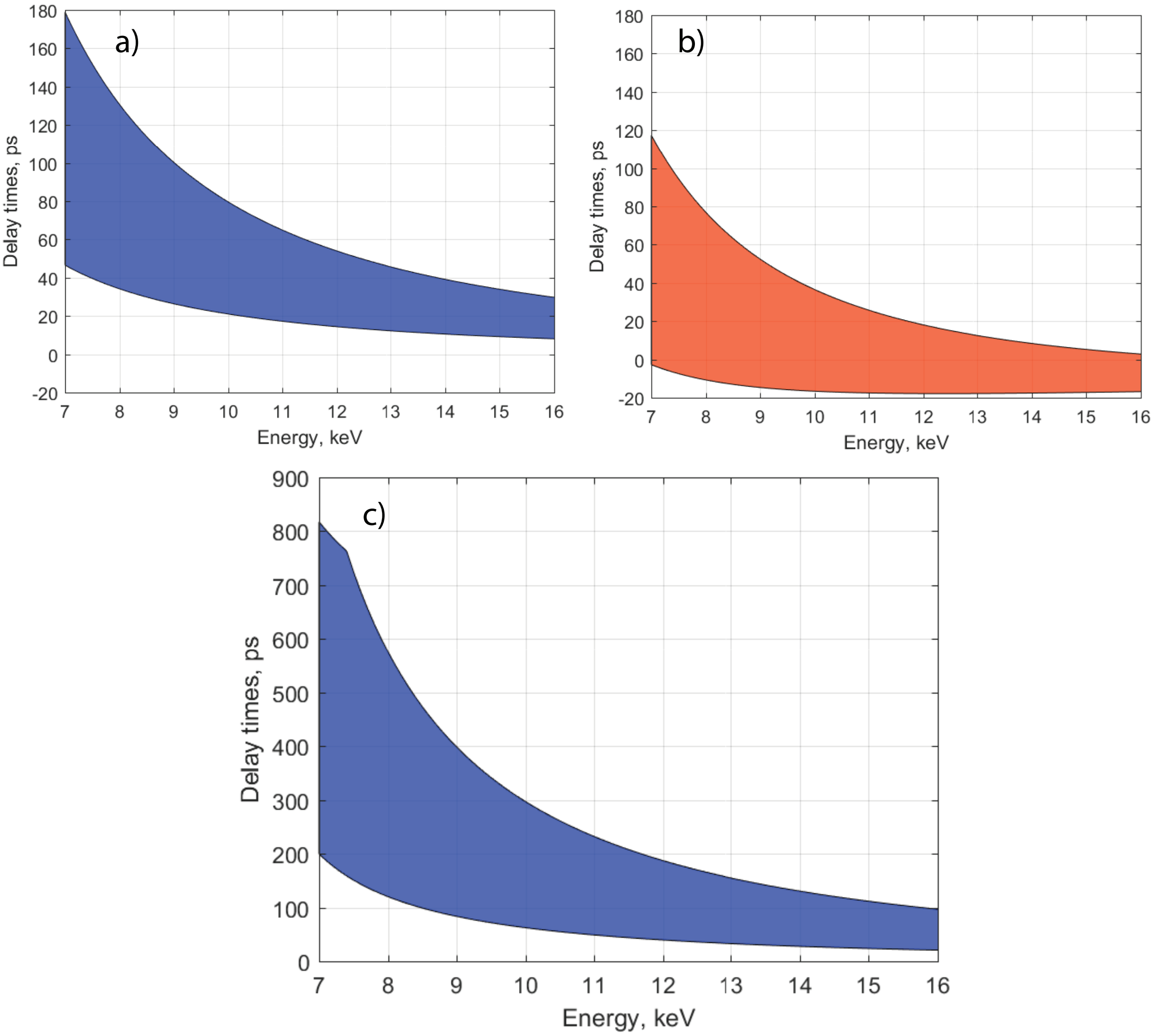

Figure 2.16: Achievable delay times with (a) Si(111)-Si(220) crystals, (b) with the mounted CH1 Si(220) channel cut and (c) with Si(220)-Si(422) BS-BR crystals without channel-cut. Calculations were performed for the photon energy range from 7 to 16 keV.

(see Figure 2.9) allows to reach the time delays from -15 ps as it is shown in Figure 2.16 b). This delay time range gives an opportunity to perform experiments, which require a temporal separation in the femtosecond and near-few picosecond delay time ranges including the delay time calibration to the $\tau = 0$.

The second configuration (see Figure 2.8) employs a Si(220)-Si(422) Bragg optics for BS-BR, respectively without the channel-cut crystals. By using this configuration a delay times up to 815 ps can be achieved (see Figure 2.16 c).

Apart from accessible delay times, throughput is a crucial parameter of the SDL. Optical path length of the fixed- and variable-delay branches is defined by Bragg angles directly affecting the throughput. For a single crystal throughput can be calculated as

$$T = R\frac{\Delta E_{\mathrm{CR}}}{\Delta E_{\mathrm{S}}}, \tag{2.16}$$

where $\Delta \mathrm{E}_{\mathrm{CR}}$ and $\Delta \mathrm{E}_{\mathrm{S}}$ are the energy resolution of a single crystal and the photon source, respectively and R is a crystal reflectivity.

To maximize the throughput of SDL, two branches can operate with slightly different range of the incoming beam. This can be achieved by adjusting the incident angle of the BS crystal. Thus, BS and BR will operate with a different ranges of energy within the range of the incoming beam.

The overall throughput for the two-crystal system (e.g. Si(111)-Si(220) according to the Figure 2.7 can be expressed as a sum for fixed T_{fix} and variable T_{var} SDL branches:

$$T = T_{\mathrm{fix}} + T_{\mathrm{var}} = \frac{\Delta E_{\mathrm{BR}}}{\Delta E_{\mathrm{SRC}}} R_{\mathrm{BS}} R_{\mathrm{BR}} + (1 - \frac{\Delta E_{\mathrm{BS}}}{\Delta E_{\mathrm{SRC}}}) T_{\mathrm{BS}}. \tag{2.17}$$

Here ΔE_{BS}, ΔE_{BR} and ΔE_{SRC} are the energy resolutions of the beam splitter BS, crystal BR and the source, respectively. For Si(111) and Si(220) the energy resolution $\Delta E/E$ equals to 1.4×10^{-4} and 6.04×10^{-5}, respectively. R_{BS} and R_{BR} corresponds to the crystal reflectivity of the beam splitter BS and beam reflector BR, respectively. T_{BS} denotes a transmission factor of the beam splitter.

In the case of using CH1 module (see Figure 2.8) the additional component R_{CH1}

must be included:

$$T = \frac{\Delta E_{\mathrm{BR}}}{\Delta E_{\mathrm{SRC}}} R_{\mathrm{BS}} R_{\mathrm{BR}} + \frac{\Delta E_{\mathrm{CH1}}}{\Delta E_{\mathrm{SRC}}} T_{\mathrm{BS}} R_{\mathrm{CH1}}. \tag{2.18}$$

This approach is also valid for the configuration with both CH1 and CH2 (see Figure 2.9) modules:

$$T = \frac{\Delta E_{\mathrm{BR}}}{\Delta E_{\mathrm{SRC}}} R_{\mathrm{BS}} R_{\mathrm{BR}} R_{\mathrm{CH2}} + \frac{\Delta E_{\mathrm{CH1}}}{\Delta E_{\mathrm{SRC}}} T_{\mathrm{BS}} R_{\mathrm{CH1}}, \tag{2.19}$$

where R_{CH1} and R_{CH2} are the total throughput of CH1 and CH2 modules, respectively.

Table 2.3 summarizes available delay times and the overall throughput of the SDL. The ratio r_{s} of fixed- and variable-branch intensities is defined as

$$r_{\mathrm{s}} = T_{\mathrm{var}}/T_{\mathrm{fix}} \tag{2.20}$$

Since Bragg optics is utilized in the SDL in various configurations, the properties of output X-ray beams such as energy bandwidth, divergence and the Darwin width are modified. In order to visualize and discuss these parameters, a DuMond diagram method [103] is used. It is a representative method for understanding properties of a series of successive optical elements on the X-ray path. DuMond diagrams show the relation between the X-ray beam divergence $\Delta\theta_i = \theta_i - \theta_B$ and the wavelength $\Delta\lambda$. Here θ_i represents the incident angle of the beam to each crystal. Further the properties of a fixed- and variable-delay branches are discussed separately.

Source, ΔE/E	Crystals configuration				τ_{min} [ps]	τ_{max} [ps]	Throughput [%]	r_s [%]
	BS	BR	CH1	CH2				
Pink beam 10^{-3}	Si(111)	Si(220)	-	-	47	179	90.9±0.1	1:15
	Si(111)	Si(220)	Si(220)	Si(220)-Si(111)	-5	117	10.8±0.8	1:1
Si(111) beam 1.4×10^{-4}	Si(220)	Si(422)	-	-	200	815	66.3±0.1	1:6

Table 2.3: Calculated values of the achievable delay times and expected throughput using various crystal sets. τ_{min} and τ_{max} corresponds to the minimum and maximum achievable delays at 7 keV. Throughput values calculated within the energy range from 7 to 16 keV. The parameter r_{s} represents the expected intensity ratio between two beams at the sample.

Figure 2.17 shows DuMond diagrams for the variable-delay branch of a 2-crystals scheme presented in Figure 2.7. Pairs of Si(111)-Si(220) and Si(220)-Si(422) were used as BS-BR crystals at the energy $E_0 = 10$ keV. According to the DuMond method, the diffracted radiation by a crystal pair equal to an intersection of the two parallelogram areas (green and yellow) of the BS and BR angular acceptance regions. In the case of polychromatic incident beam with the finite divergence θ_i, the exit divergence θ_e and the wavelength bandwidth $\Delta\lambda$ can be defined as [104]:

$$\begin{aligned} \Delta\lambda &= (\theta_0 + \theta_i) \cos\theta_B 2d, \\ \theta_e &= \theta_0 |1 + b| + \theta_i. \end{aligned} \tag{2.21}$$

The arrangement of the BS and BR crystals shown in Figure 2.7 can be considered as a non-dispersive [105], meaning that the bandwidth and wavelength spread will be conserved before and after this crystal pair. It denotes the parallel setting of two identical reflections. The throughput of the delay line optics is varying depending on the divergence of an X-ray source. A divergence of European XFEL SASE2 is equal to 0.17 arcsec [4] and used as a reference on the plots.

Figure 2.17 a) and b) shows variable-delay branch diagrams for BS−BR crystal pairs respectively. The incident beam with the energy $E = 10$ keV is diffracted by Si(111)−Si(220) and further by Si(220)−Si(422) crystals (BS-BR), respectively. Angular widths of these crystals are 5.38 arcsec−4.02 arcsec and 4.02 arcsec−2.05 arcsec (BS-BR), respectively. In every crystal pair the crystal bandwidth of BR is always smaller than the bandwidth of BS. The exit divergence of the 2-crystal SDL configuration is equal to 4.02 arcsec for Si(111)-Si(220) and 2.06 arcsec for Si(220)-Si(422) BS-BR crystal combinations.

For the CH1 module configuration the respective DuMond diagram is shown in Figure 2.18. The output divergence of the CH1 module is equal to 5.36 arcsec with the Si(111) channel-cut, giving a broad exit divergence. The European XFEL SASE2 beam divergence was taken as an example and marked by the blue regions in DuMond

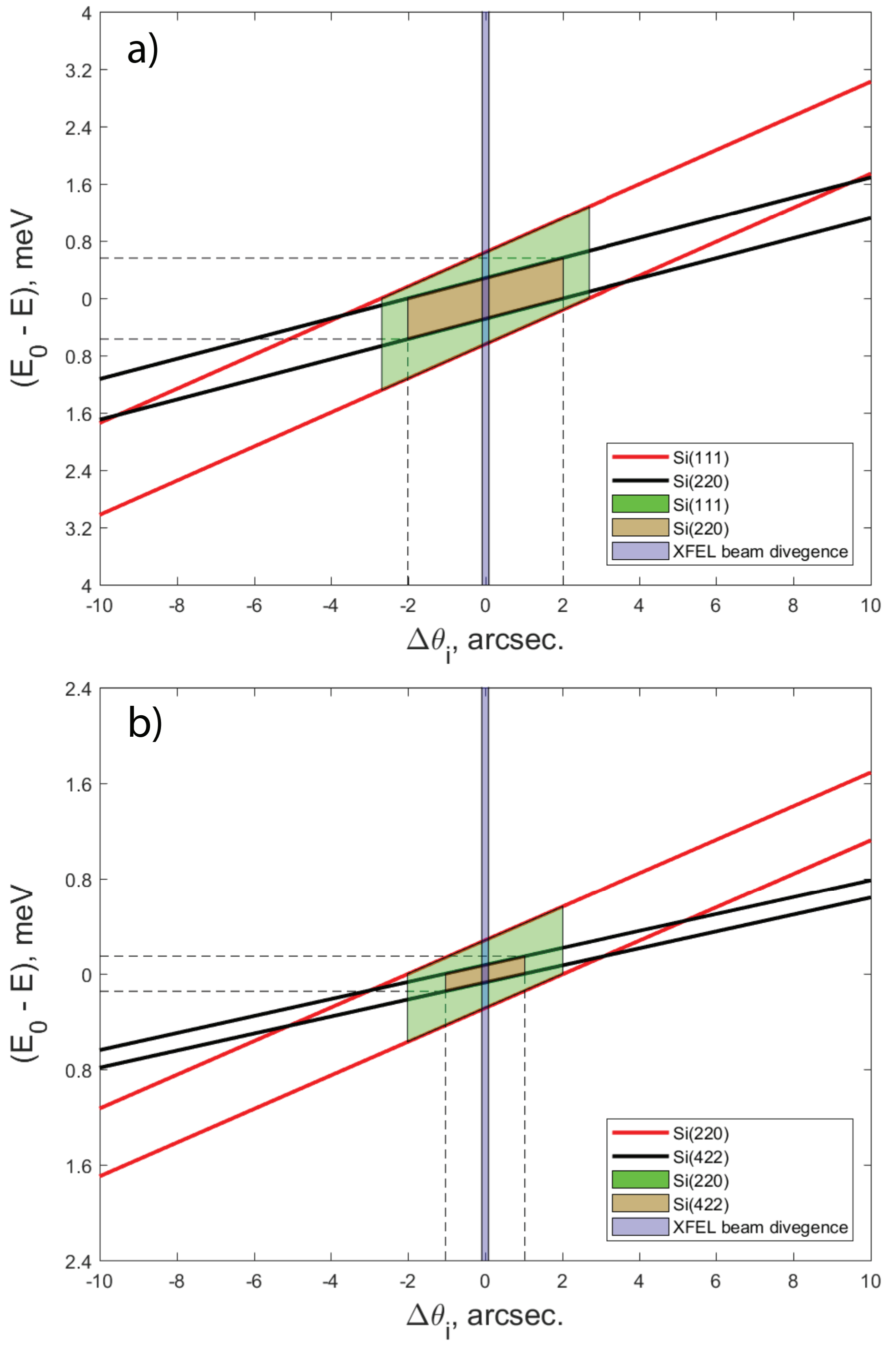

Figure 2.17: DuMond diagram illustrating the performance of 2-crystal scheme with a) Si(111)-Si(220) and b) Si(220)-Si(422) crystals at $E_0 = 10$ keV. The blue area corresponds to the XFEL beam divergence. Horizontal and vertical dashed lines show energy ranges and the angular widths of the diffracted beam, respectively.

diagrams. This area is fully covered by the crystals acceptance of the implemented optics. A throughput is not affected by the source divergence since it is much smaller than the angular acceptance of the delay unit optics.

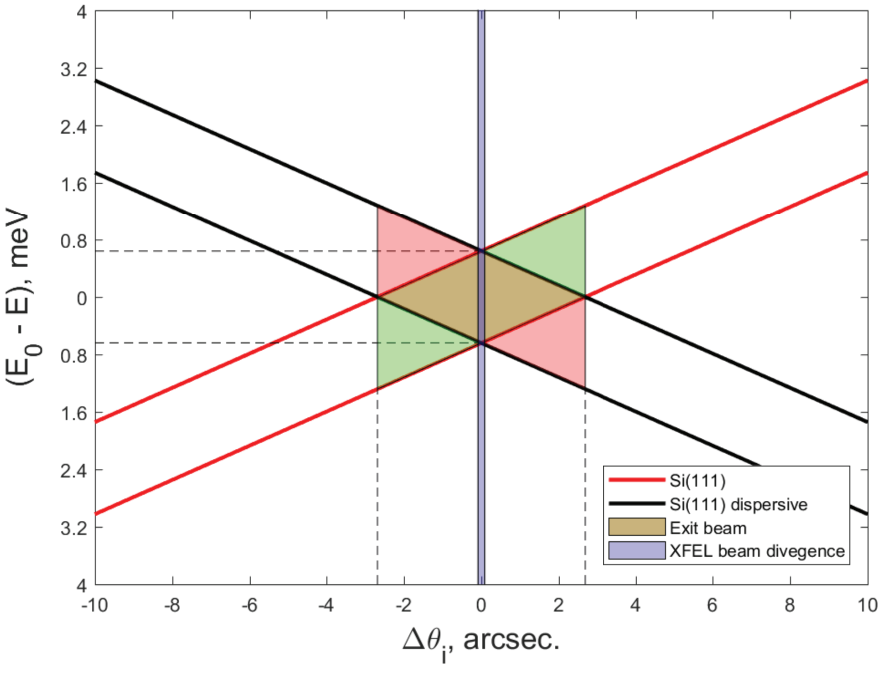

Figure 2.18: DuMond diagram illustrating the performance of the SDL scheme with Si(111) CH1 channel-cut at $E_0 = 10$ keV. The blue area corresponds to the XFEL beam divergence. Horizontal and vertical dashed lines show energy ranges and the angular widths of the diffracted beam, respectively.

Chapter 3

Experimental setup

The mechanical design of the split-and-delay line is presented in this chapter. Precise piezo driven stages are employed in the setup to control the positions of the crystal optics with nanometer resolution. Diagnostics tools, such as a beam position monitor and intensity diodes, are employed for the setup alignment, on-line intensity measurements and beam tracking. Dedicated software was developed to control opto-mechanics of the setup. A sophisticated 6-axis tripod was designed and manufactured to align the split-and-delay line to the incident X-ray beam. A description of the beamlines, used in the characterization of the device and its components is given in the last part of the chapter.

3.1 Mechanical design

The concept, presented in Chapter 2, defines the general SDL setup design. Components of the device must meet several mechanical requirements:

- Bragg crystals for the variable-delay branch must be produced using chemical mechanical polishing of the diffracting surfaces [106]. They must have a reliable holding mechanism and small dimensions without limiting the functionality of the SDL.
- The resolution of motors for crystal alignment must be smaller than the width of their Bragg reflections. An angular resolution well below 1 arcsec is required for the operation in the hard X-ray energy range.
- A strict algorithm of calculating absolute positions of the stages must be developed and implemented. Any mechanical inaccuracy will result in X-ray intensity losses and the necessity of the SDL realignment. Compact translation stages with step resolution $< 1\mu\text{m}$ are required to reach delay time step size of < 1 ps.
- The whole SDL setup must be mechanically stable and robust.
- Diagnostics tools for tracking the beam position, shape and in-situ intensity measurements in both branches should be employed. These tools must serve as measurement devices during X-ray experiments and also help in a fast alignment of the setup during the commissioning prior experiments.
- The sample stage must be designed and placed inside the device. It requires a 3-axis positioning control and flexible options for various sample holders.
- Implemented PCVM beam splitters (see Section 2.4.1) have been already manufactured. The BS holder must be designed and placed on the 6-axis tripod.

3.1.1 Bragg crystals

Bragg crystals (BR) implemented in the setup are Si(220) and Si(422) depending on time delay range (see Section 2.4). Therefore, the SDL setup must be able to mechanically switch between crystals during the operation. To make the BR stage very compact, Bragg optics was designed and manufactured according to the sketch shown in Figure 3.1 a). They have a 20×15×10 cm^3 dimensions with a grooves on both sides that allow clamping crystals to a holder. The diffracting surface of each crystal was etched and polished using the chemical mechanical polishing procedure [106]. For the diagnostics purposes (i.e. tracking the beam position), an additional fluorescent screen at the BR stage is employed. Therefore, 3 slots for two BR crystals and the fluorescent screen are included in the design (see Figure 3.1 b).

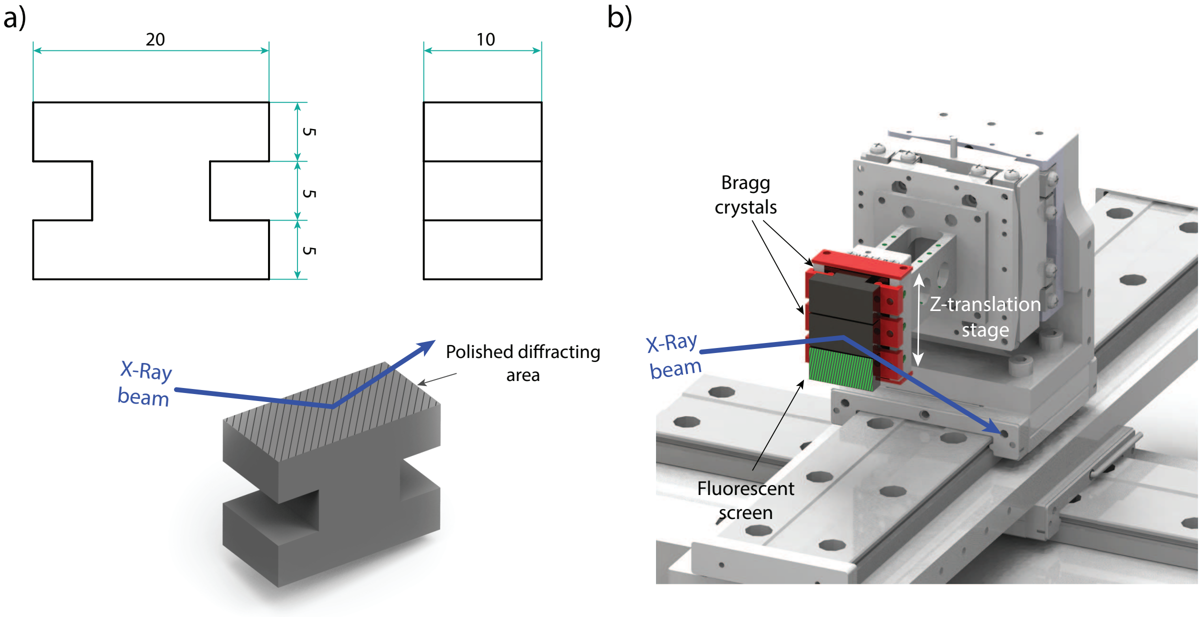

Figure 3.1: (a) Sketch of BR crystals, developed for the SDL setup. Two BR crystals and a fluorescent screen are mounted on the BR stage (b), which can be translated vertically by Z-translation stage.

3.1.2 Design of the main mechanical components

The device is developed in a modular design, such that each optical component is placed on a separate stage with multiple degrees of freedom. To achieve the required angular resolution for the alignment of crystal optics (see Section 2.2) with preserving the expected device dimensions, SmarAct [107] angular and linear piezo positioners were chosen to move the crystals. These positioners are commercially available, providing nanometer precision which is exceptional for their size. Classic stepper motor stages are not applicable due to their big size and imprecise stepping (µm range).

The device consists of two main stages for translation of BS and BR crystals. Figure 3.2 shows the layout of the developed system. The whole unit is mounted on the 40 kg optical table, providing a necessary mechanical stability to the setup. The optical table was manufactured by Thorlabs and has a dimensions of $60{\times}60$ cm^2.

The BS crystal is mounted on the movable 6-axis tripod (SmarPod 110.45), translatable along the main beam path by the linear positioner SLLV42 (see Figure 3.2). The crystal BR is mounted on a stage which allows three linear (x, y, z) and two angular motions (α_x, α_z) by using SLLV42 linear motors and SGO goniometers. Three different crystals can be placed on this stage and switched during the operation by simply moving the SLC crystal stage in z direction (see Figure 3.2). All crystal stages provide up to 1 nm linear and 0.006 arcsec angular movement resolutions, which gives in total a nominal femtosecond delay time precision in the operating energy range. The main parameters of the motors for the SDL device are listed in the Table 3.1. The base table with BS and BR main stages is shown in Figure 3.3. The respective travel axes of the both crystals are marked with the red arrows.

The whole optical table together with crystals and stages is covered with the acrylic glass enclosure (see Figure 3.6), enabling operation in helium atmosphere. This allows to reduce the X-ray absorption of the air and speeds up the heat flow inside the setup.

A sample environment is designed and placed in the intersection point of the fixed and variable-delay branches. The stage consists of an x-y-z positioner with 5 µm step resolution. The holders for various sample types, such as membranes, capillaries or any custom mounts are implemented. For the CH2 configuration (see Section 2.3) the sample holder is exchanged to the CH2 module with respective crystals on the motorized piezo stages.

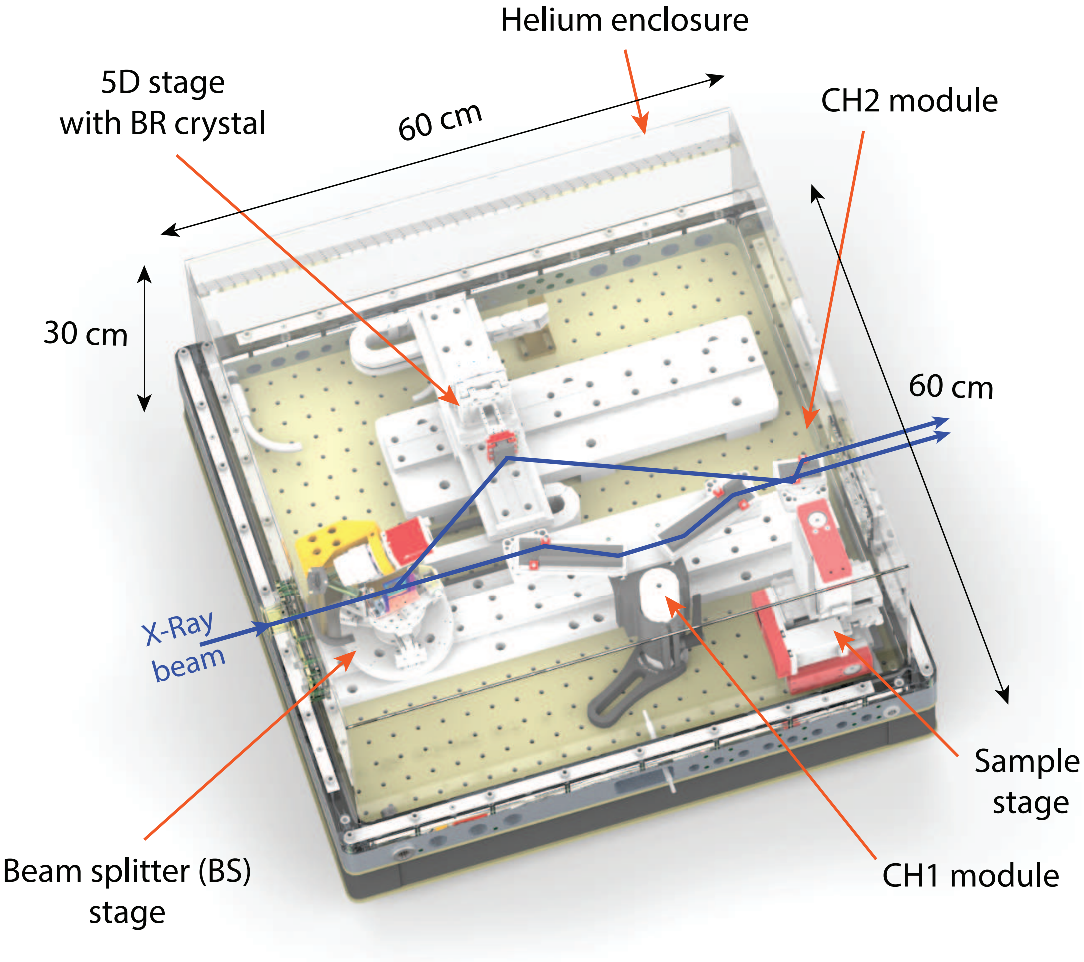

Figure 3.2: 3D sketch of the developed SDL system.

Crystal	Positioner	Axis	Travel range	Resolution
BS	SmarPod 110.45	x	20 mm	1 nm
		y	20 mm	1 nm
		z	11 mm	1 nm
		α_x	21°	0.2 arcsec
		α_y	24°	0.2 arcsec
		α_z	38°	0.2 arcsec
	SLLV42	x	530 mm	1 nm
BR	SLLV42	x	380 mm	1 nm
	SLLV42	y	270 mm	1 nm
	SLC-1730	z	21 mm	1 nm
	SGO-60.5	α_x	10°	0.006 arcsec
	SGO-77.5	α_z	10°	0.006 arcsec

Table 3.1: Specifications of crystal stages. α_x, α_y and α_z represent the angular motions around x y and z axes, respectively.

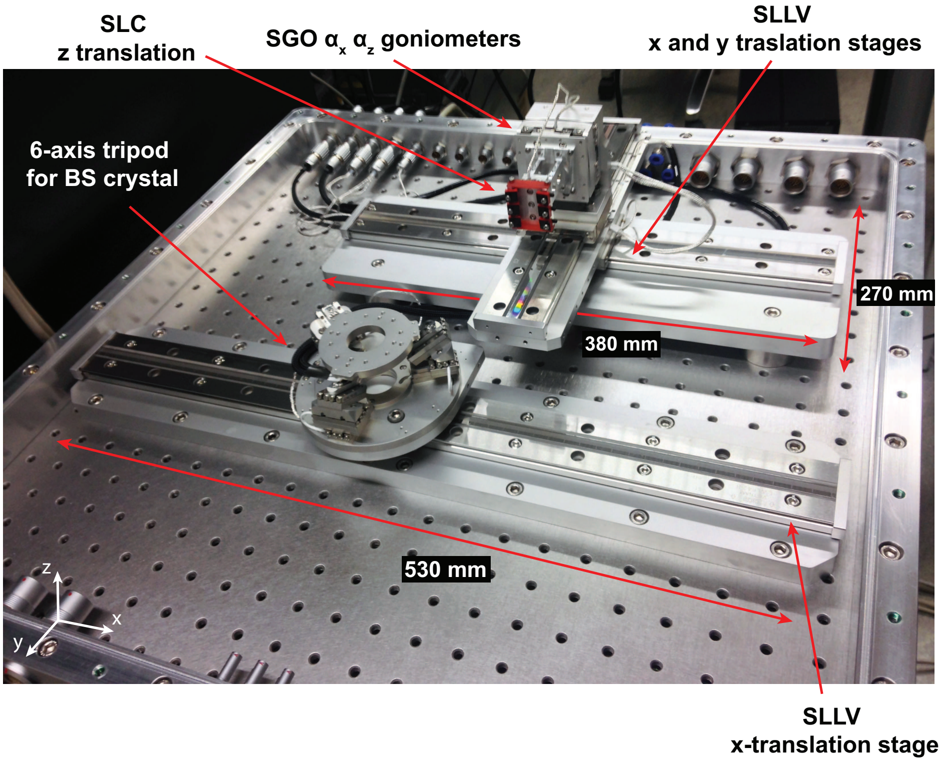

Figure 3.3: Main stages for BS and BR crystals, installed on the optical table. Respective stages from the Table 3.1 are marked with the arrows.

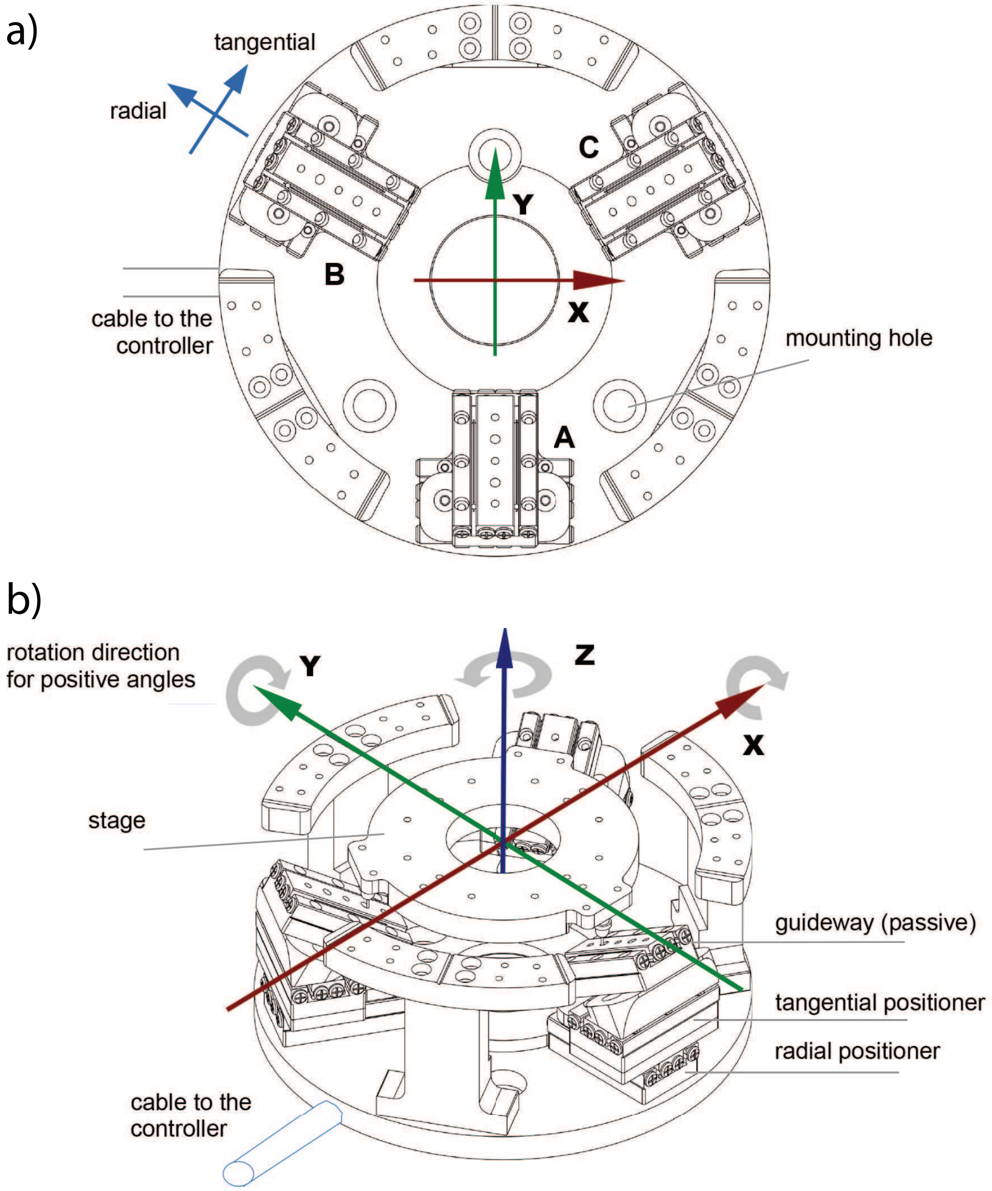

Figure 3.4: The top a) and the perspective b) views of the 6-axis tripod (SmarPod) with the coordinate system and directions of motor translations [108].

A 6-axis tripod, which is used for an alignment, has a sophisticated motion system [108]. It has three groups of positioners: A, B and C as it shown in Figure 3.4. Each group consists of a radial, a tangential and a guideway positioner. In total the tripod has 9 linear piezo motors controlling the translation, pitch and the pivot point of the object on top of its stage. The stage of the SmarPod can be moved in three linear directions and rotated around the pivot point in three angular directions. The default pivot point is located below the stage (see Figure 3.5 a) since at this point the range of angular motions is maximal. The greater the distance of the pivot to the default point, the smaller the angles the tripod can rotate. Figure 3.5 b) shows how the stage can be rotated to the same angle θ around different pivot points, marked by the red circles.

The translation and orientation of the 6-axis tripod stage is related to the actual pivot point offset from the zero coordinate (factory setting of encoders zero locations) along x, y and z axes. The actual stage translations and rotations executes around the pivot point which is the center of all rotations. By setting the pivot point it is possible to move the tripod around objects or points of interest, such as the center of the mounted BS crystal in the SDL.

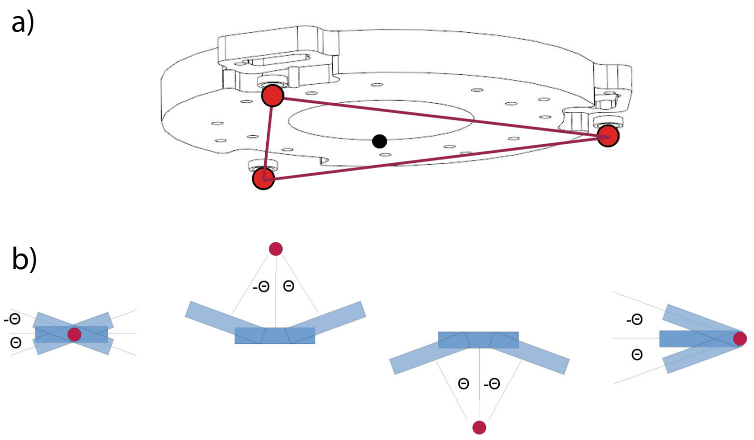

Figure 3.5: a) The default pivot point of the tripod, denoted by the black circle, and b) rotations of the stage around different pivot points (denoted by the red circles) to the angle Θ.

3.1.3 Base 6-axis tripod

The SDL setup is designed as a portable device, allowing to perform experiments at various FEL sources. However, prior every experiment, the setup has to be installed at an experimental hutch. Moreover, the X-axis of the SLLV translation stage of the BS crystal must be aligned parallel to the X-ray beam and the SDL base table must be positioned in the horizontal plane. In order to perform this alignment a base 6-axis tripod was designed and built below the SDL as it is shown in Figure 3.6. The tripod has three pairs of positioners (radial and tangential) operating in the similar way as the BS 6-axis tripod. It is able to hold, rotate and translate up to 100 kg of the weight in 3 linear and 3 angular motions. Each motor of the tripod has 5 µm step resolution, ensuring very good positioning precision.

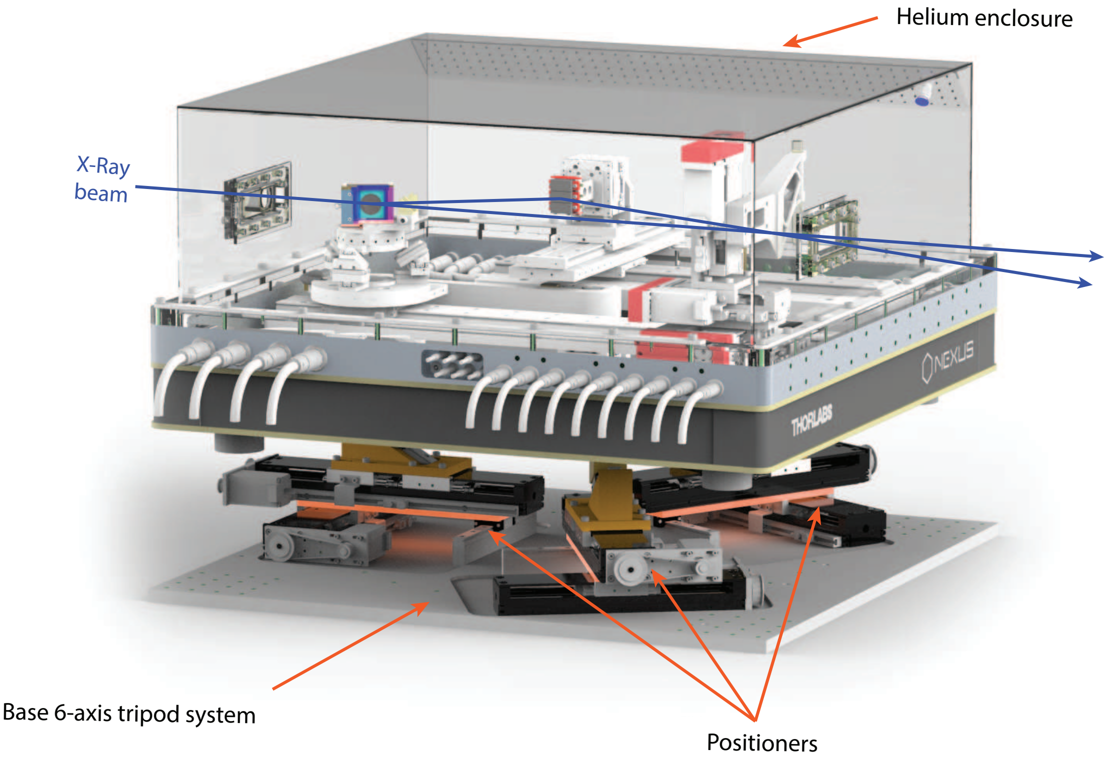

Figure 3.6: The SDL setup covered with the helium enclosure and mounted on the base 6-axis tripod.

3.2 Beam diagnostics

To monitor the intensity and shape of X-ray pulses inside the SDL and determine the time between two split pulses, a set of diagnostics tools was developed and implemented. For the alignment of the SDL to the main beam path, an X-ray beam position monitor (XBPM) is installed on the top of the BS stage (see Figure 3.7). The monitor consists of a CMOS camera and a yttrium aluminium garnet (YAG) crystal, which can be moved to the main beam path in front of the BS crystal. When the YAG crystal is illuminated, the XBPM gives the 2D beam profile with 3 µm resolution. Moreover, the precise alignment of the setup is achieved by translating the XBPM stage along the main beam path and tracking the position of the beam on the camera.

In order to measure the quantitative intensity values of split pulses in both branches during the operation, Passivated Implanted Planar Silicon (PIPS) diodes [109] are implemented in the setup (see Figure 3.8). Diodes are positioned 30 mm after the BS and BR crystals, respectively. Each diode is equipped with 25 µm kapton foils. The kapton is mounted at 45 degrees with respect to the active area of the diode, producing

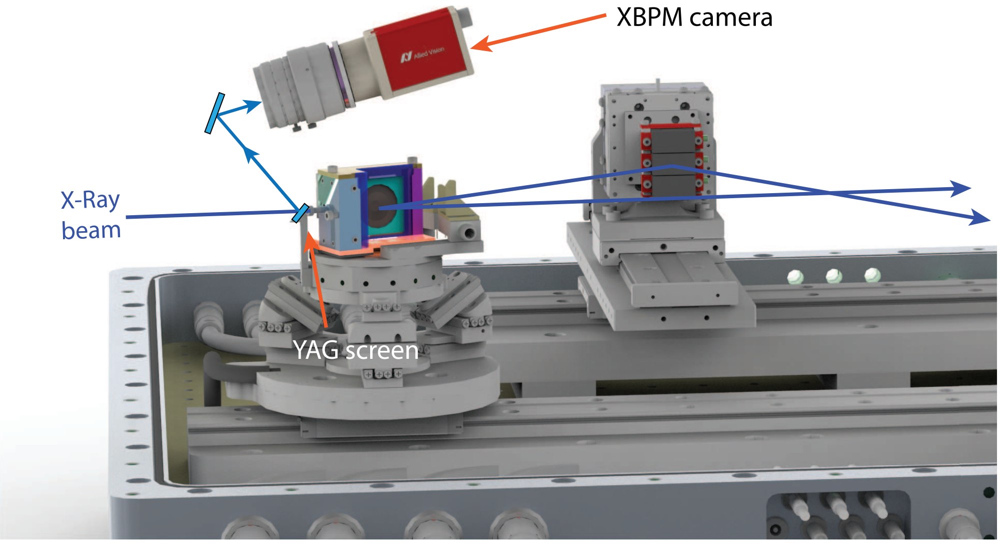

Figure 3.7: XBPM assembly with a YAG screen mounted on the tripod and the camera, following the scattered luminescence geometry. Camera holder and the mirror assembly (in front of the camera lens) are not shown.

the scattering signals during the X-ray illumination [67]. The registered intensity of the scattered X-ray beam create the output diode current which is amplified by a current-to-voltage amplifier (FEMTO DLPCA-200) according to the scheme, shown in Figure 3.9. The voltage signal is processed by the Raspberry Pi Logic Controller (PiLC) module [110]. The module has an embedded PC, a FPGA chip and I/O interfaces for digital and anlog signals. This module has been designed to control the FPGA operation from a user-friendly Tango platform (see Section 3.3) through the network. The count rate from the amplifier is further transmitted to the PC via the network. A beam splitting ratio is obtained by measuring the pulse intensities in both branches separately.

Additional shutters are installed in both branches to separate the signals at the output of the SDL. The shutters can be activated when the sample is to be illuminated only by the single beam either from the fixed- or variable-delay branches.

Compact ionization chambers (IC's) [16] are also used for quantitative flux measurements. They were manufactured at DESY and have the size of 48×40×20 mm (see Figure 3.10). Small dimensions of the IC's allows to incorporate them into the compact

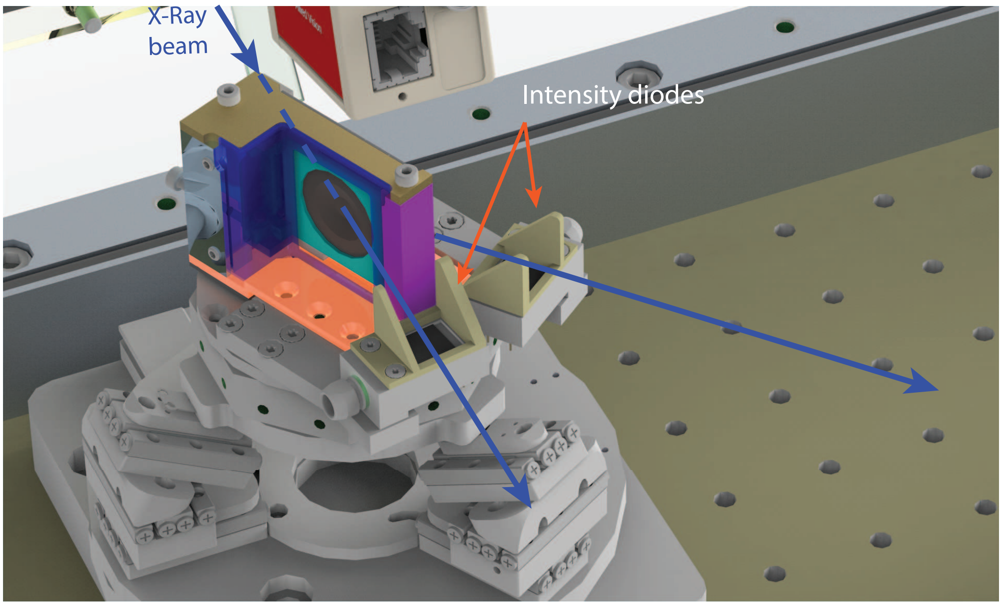

Figure 3.8: The view on the BS 6-axis tripod with the intensity (PIPS) diodes in fixed- and variable-delay branches. The kapton foils on the diodes are not displayed.

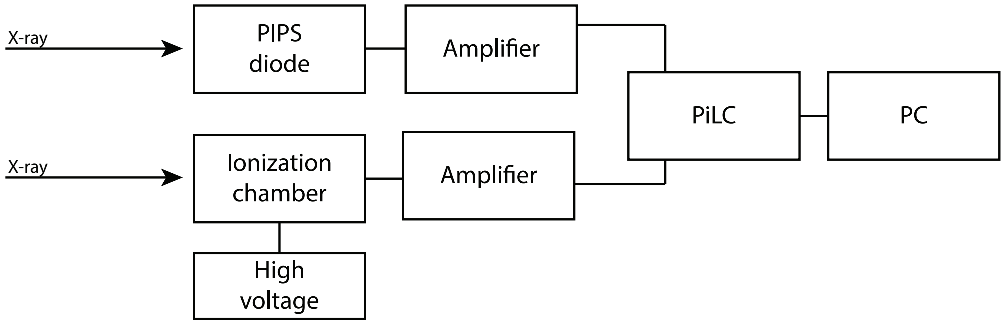

Figure 3.9: Scheme of the electronics used to register the signals from the PIPS diodes and the ionization chambers.

design of the SDL. The housing of the chambers is made of a light insulating material (trovidour). The electrodes are made of copper to minimize discharging effects. The efficiency of the chamber can be increased by filling it with various gases.

The electric field is created in the chamber by applying voltage between the electrodes through the standard SHV (Safe High Voltage) socket from a high voltage power supply. The output ionization current is amplified by a current-to-voltage amplifier (FEMTO DLPCA-200). The voltage signal is processed by the PiLC module [110], transmitted to the PC and recorded using the Tango software (see Section 3.3).

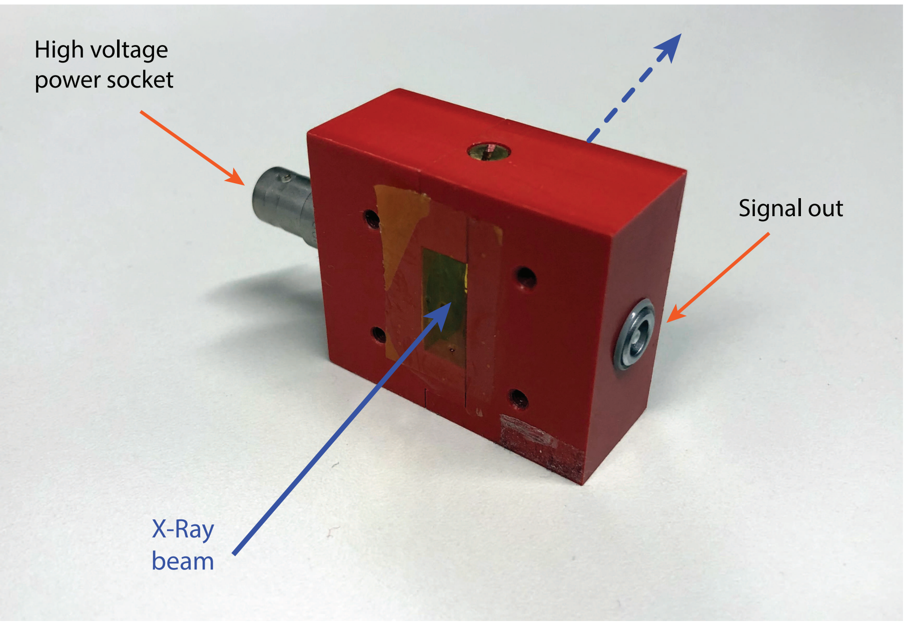

Figure 3.10: Ionization chamber, implemented in the SDL.

3.3 Control system

Figure 3.11 shows a scheme of the SDL control system. The setup employs stepper motors as well as the SmarAct piezo motors. The stepper motor controller unit (OMS VME58) is powered by the power supply with a separate power line for the each motor. The controller has a micro stepping option, which improves the resolution by a factor up to 20. The whole system is controlled by the Tango software [111], which has a separate server for every mechanical device in the SDL. The SmarAct piezo motors (6-axis BS tripod, crystal stages) are controller by the SmarAct controller via the Tango control system. The connection between the controller and the PC is established via the network interface. The controller hardware has the integrated CPU with sophisticated algorithms of positioning and computing the motion of every stage separately.

Peripherial devices and all diagnostics tools are connected to the PiLC module [110] and controlled from the main PS's Tango system via the network connection.

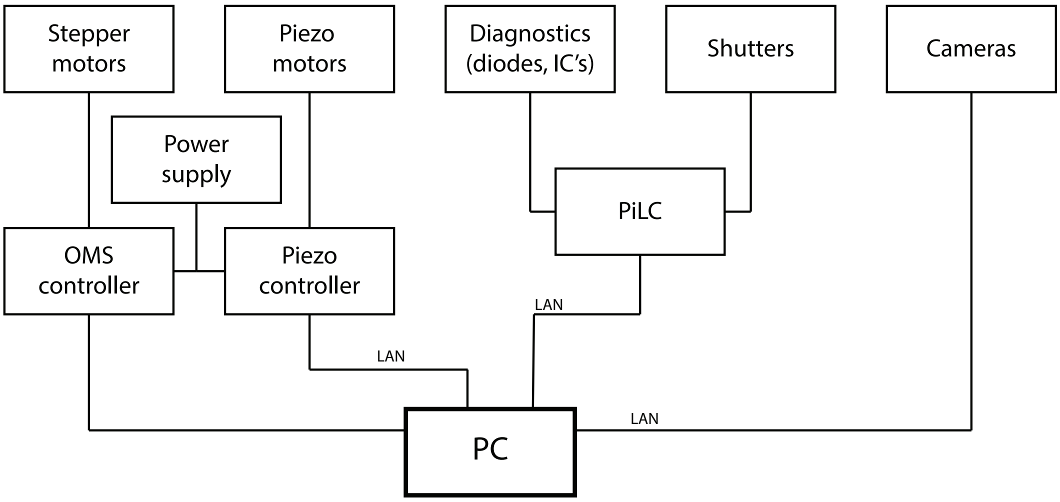

Figure 3.11: Scheme of all electronic and controller units, employed to the SDL setup.

3.4 Control software

To operate the whole SDL in the convenient way a dedicated user application was developed in Python. The setup has 31 real and virtual motors, which could be operated simultaneously. The initial coordinates of each motor are calculated according to the diffraction geometry based on the current photon energy, crystal positioning, holder type, etc.

Prior to the operation all piezo motors should be calibrated, initialized and defined in the system. The developed configuration software combines all this procedures and options in a common user user interface, including also the XBPM camera viewer, stage configurators and some basic scanning options. The stages are operating via the Tango control system [111], which can be controlled using the software interface and command line at the same time. For the device calibration all the coordinates of specific delay times can be stored and mapped according to the preliminary interference measurements, explained in the Section 4.1.

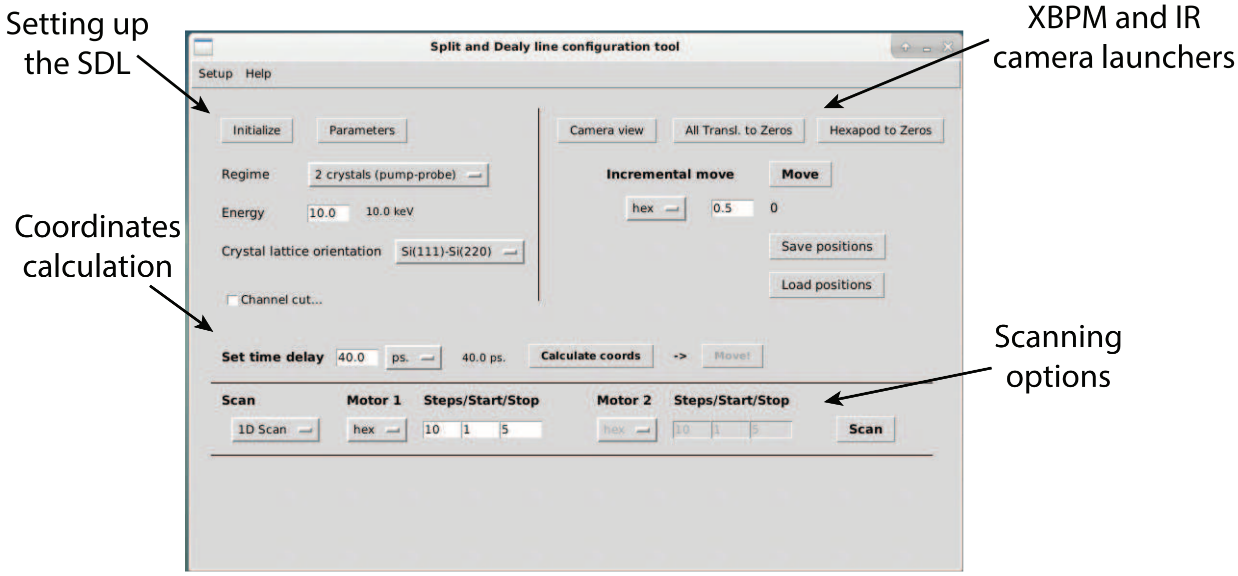

Regime: 2 crystals (pump-probe)

Energy: 10.0 — 10.0 keV

Crystal lattice orientation: Si(111)-Si(220)

☐ Channel cut...

Set time delay: 40.0 ps. — 40.0 ps.

Incremental move: hex 0.5 — 0

Scan	Motor 1	Steps/Start/Stop	Motor 2	Steps/Start/Stop
1D Scan	hex	10 / 1 / 5	hex	10 / 1 / 5

Figure 3.12: SDL configuration tool to set up, initialize and operate the setup

3.5 Analysis software

To analyze the experimental data, obtained during X-ray topography measurements (see Section 4.2), the interactive software was developed (see Figure 3.13). The software allows to analyze the crystal diffraction datasets using convenient user interface, showing intensity and topography maps, reconstructed from the detector data. Rocking curves from each pixel of the detector can be previewed separately. Obtained topograms from an investigated crystal can be evaluated by comparing the FWHM values of the measured data to the theoretical Bragg curve for the given photon energy and crystal lattice orientation.

The software can operate on-line during the measurement process, reading the acquired images directly from the beamline storage. By implementing the multi-core parallel calculations, the processing of the full topography scan takes seconds, giving the resulting topograms. Additional features such as background subtraction, noise reduction and the data enhancement are also enabled.

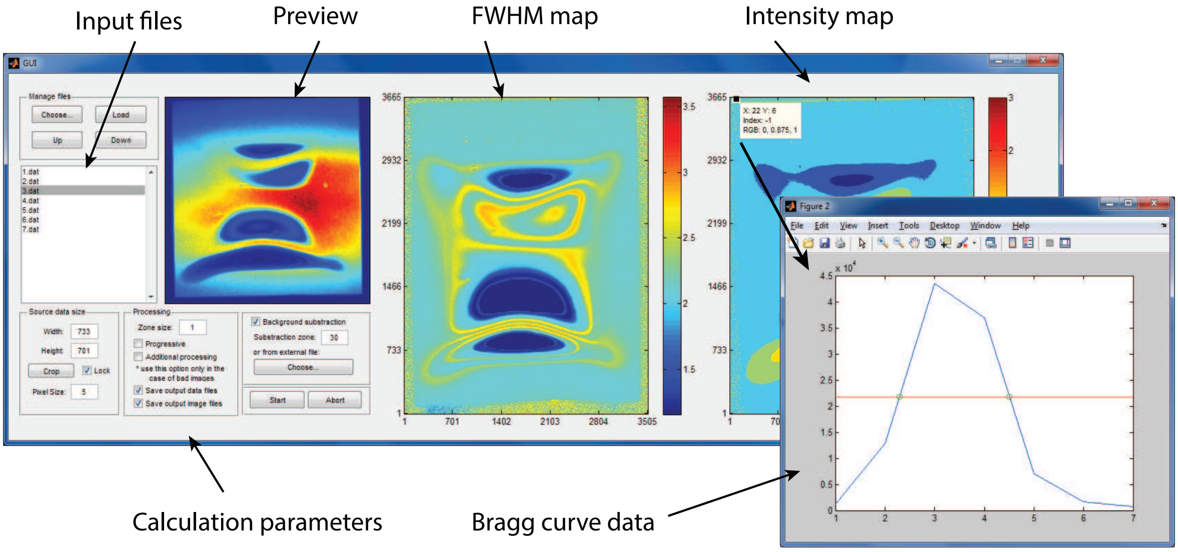

1.dat
2.dat
3.dat
4.dat
5.dat
6.dat
7.dat

Source data size
Width: 733
Height: 701
☑ Lock
Pixel Size: 5

Processing
Zone size: 1
☐ Progressive
☐ Additional processing
* use this option only in the case of bad images
☑ Save output data files
☑ Save output image files

☑ Background substraction
Substraction zone: 30
or from external file:

X: 22 Y: 6
Index: -1
RGB: 0, 0.875, 1

Figure 3.13: Software for the on-line data processing of the topography data during the experiment.

3.6 Description of the beamlines

3.6.1 BM05/ESRF

Investigations of the thin PCVM beam splitters performance (see Section 4.2) were performed at the BM05 beamline [112] of the European Synchrotron Radiation Facility (ESRF). This experimental station is dedicated for a test-and-development of X-ray optical elements, beam characterization, and instrumentation research. This beamline is unique in terms of flexibility, having a wide photon energy range from 6 to 60 keV and the beam size from 1.0×1.0 μm^2 (H x V) up to 40.0×8.0 mm^2. Si(111) and Si(333) monochromators can be used to control energy resolution of the beam. As a photon source a bending magnet is used. The beamline has a various customizable stations located at 28m, 40m and 55m where either white or monochromatic beam can be delivered.

A schematic sketch of the beamline is shown at the Figure 3.14. After the bending magnet, a pair of primary slits cut the part of the beam. A double-multilayer

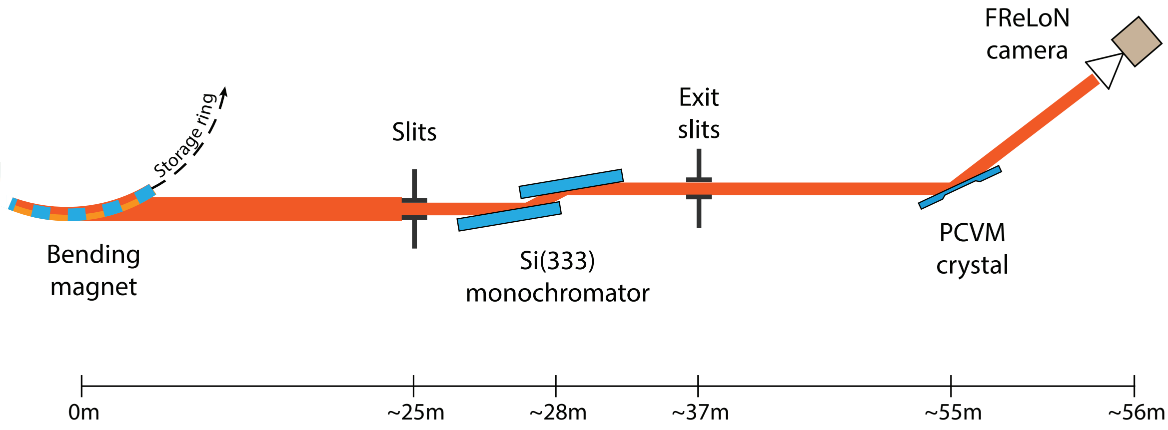

Figure 3.14: Scheme of the BM05 beamline at ESRF.

monochromator is located further after the primary slits, aligning the energy bandwidth with the Si(333) crystal monochromator. Final beam size is tuned by the exit slits, located before the experimental hutch. Investigated PCVM crystals were mounted at the sample stage, shown in Figure 3.15 a).

On the vertical diffractometer arm (see Figure 3.15 b). a FReLoN detector [113] was mounted in order to collect the diffraction patterns. The FReLoN camera is a fast-readout, low-noise Multi-Pinned Phase detector with a 14-bit resolution. It is based on a CCD sensor, having 2048 × 2048 pixels with the pixel size of 14 μm^2. The camera is equipped with a 5 μm thick Gd_2O_2S:Tb scintillator screen, which has a grain size of 1 μm, giving a field of view of 10.85 μm^2 in respect to the 5.3 μm input optics resolution. By using a custom tunable optics, resolution down to 1.4 μm can be obtained. Housing of the camera is shielded by 2 mm thick brass housing, preventing the noise on acquired images.

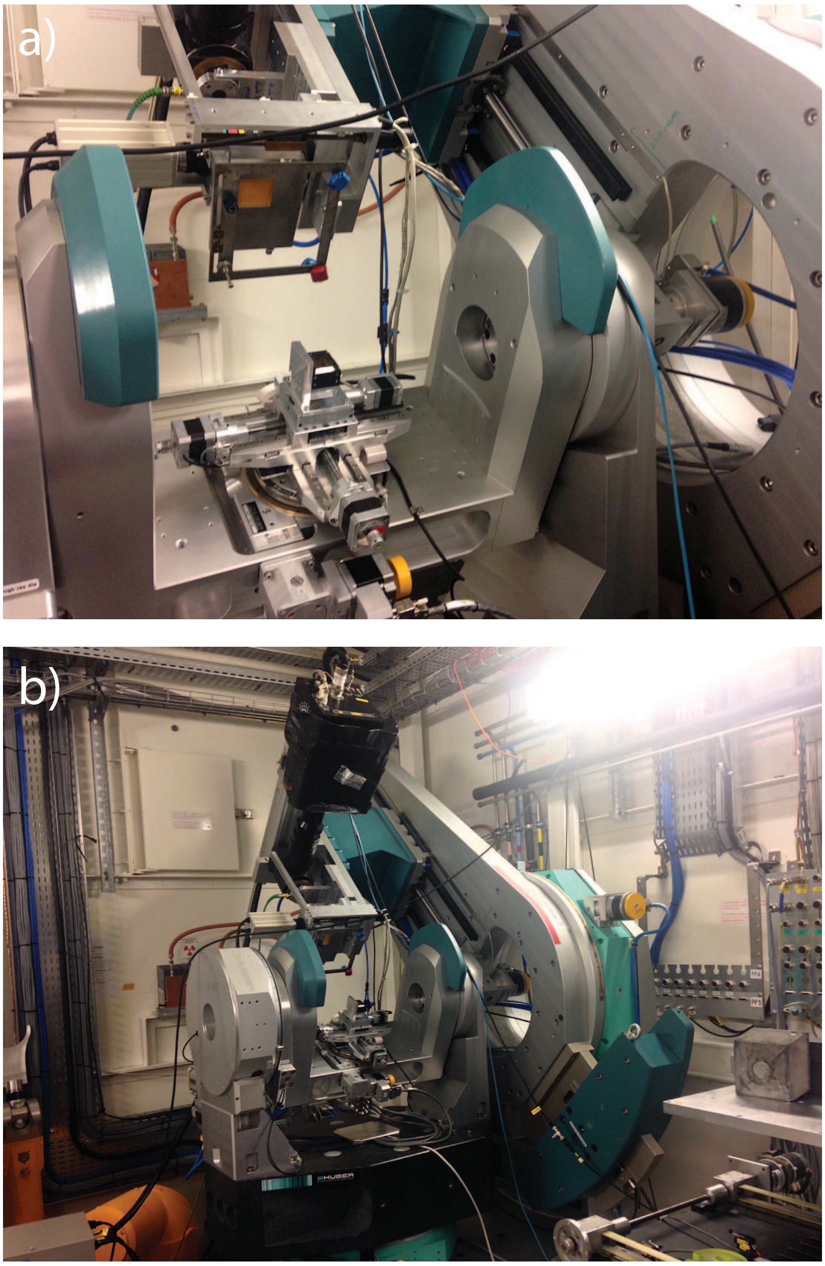

Figure 3.15: a) The diffractometer in the experimental hutch with the b) investigated crystal, mounted in the holder.

3.6.2 P10/PETRA III

Scanning topography investigations on PCVM beam splitters (see Section 4.2.2) were performed at the P10 beamline [114] of PETRA III at DESY. The beamline is dedicated to experiments using coherent X-rays.

The beamline infrastructure consists of the front-end part, the optics hutch and two experimental hutches. The source of X-rays for the beamline is a 5 m long undulator, located at the low-beta section of the storage ring. The photon source size is $\sigma_h \times \sigma_v = 39.5 \times 6.52\ \mu m^2$.

Power slits systems are installed after the undulator in 14 and 28 meters, respectively (see Figure 3.16). The heat load monochromator is located at about 38 meters away from the source. Flat X-ray mirrors M1 and M2 (curvature radius R>100 km) are located after the monochromator and reflect the beam in order to suppress higher harmonics of the undulator spectrum.

At the distance of approximately 73 meters, a diffractometer is installed in the experimental hutch. During the scanning topography measurements a hexapod with the investigated crystal was mounted on the diffractometer. A PCO Edge 5.5 camera was installed on the vertical movable arm of diffractometer to acquire the diffraction patterns from the crystal. The PCO Edge 5.5 is equipped with a high resolution 2560×2160

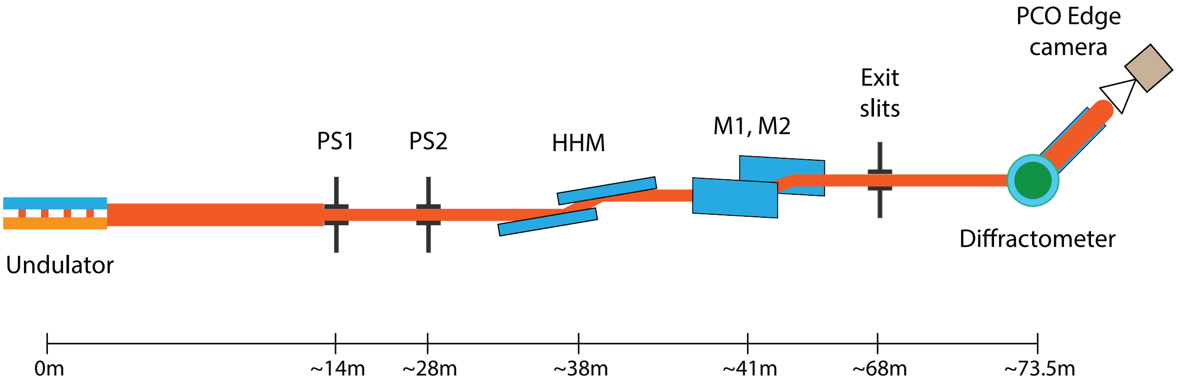

Figure 3.16: Scheme of the P10 beamline at PETRA III.

CMOS sensor (6.5×6.5 µm pixel size), providing images at the frame rate up to 100 fps. This specific camera was used for topography investigations due to the homogeneous pixel response and an excellent dark signal pixel behavior with the readout noise of 1.0 electrons (e^-).

Figure 3.17 shows the general view on the experimental hutch and the diffractometer, where the crystal was mounted. The investigated crystal was placed in the diffractometer's center of rotation.

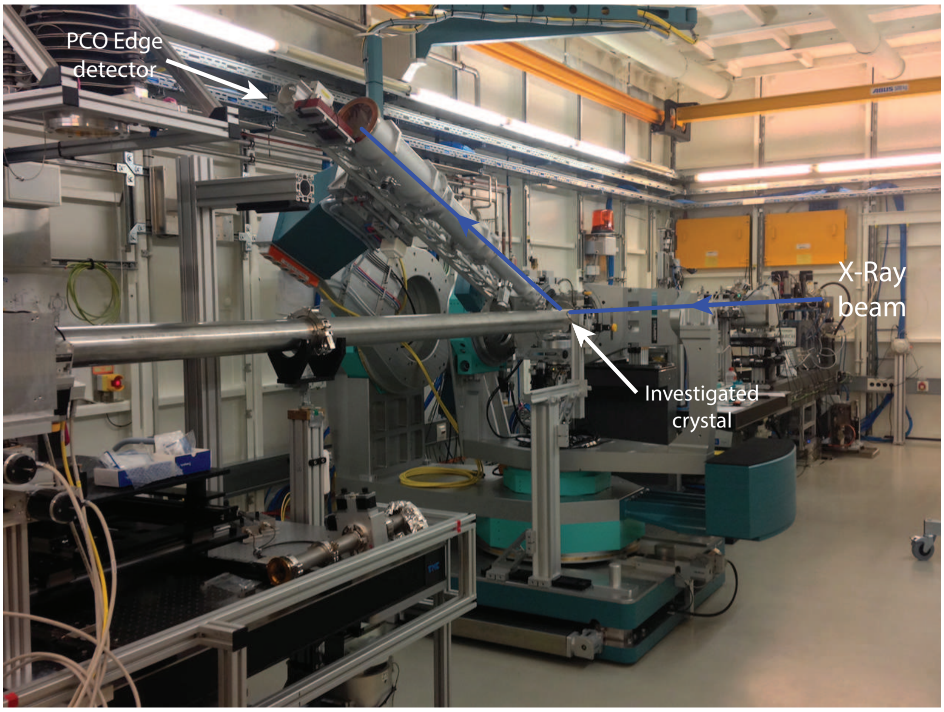

Figure 3.17: a) View on the diffractometer in the experimental hutch of the P10 beamline.

3.6.3 P64/PETRA III

The splitting performance of the Si(220) beam splitter as well as throughput and delay time measurements (see Sections 4.2.3, 4.3, 4.4) were performed at the P64 beamline [112] of PETRA III at DESY.

P64 beamline is dedicated to X-ray absorption spectroscopy experiments, which require high flux at the sample. This is a major advantage for testing the performance of the SDL. The 2 m long undulator act as a beamline photon source, providing 1×10^{13} photons/second at the sample position.

A scheme of the P64 beamline is shown in Figure 3.18. After the undulator a power slit system S1 is installed. To control the beam a cooled double crystal monochromator (HHM) and two mirrors M1 (flat) and M2 (flat bendable) are installed in the beam. The beam size at the sample is controlled by the exit slits S2.

After the exit slits the experimental hutch with a sample setup is located. The sample environment consists of holders and calibrated ionization chambers.

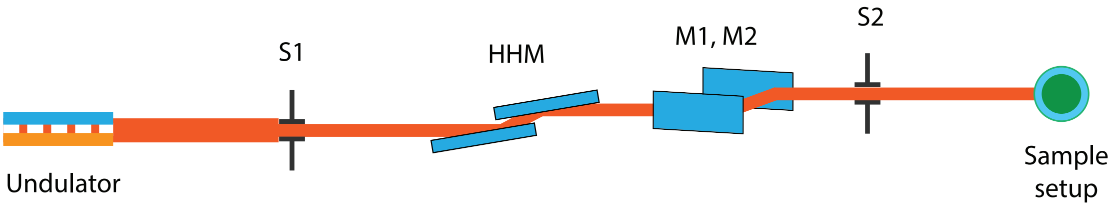

Figure 3.18: Scheme of the P64 beamline at PETRA III.

Chapter 4

Split-and-delay Line performance

In this chapter the performance of the split-and-delay (SDL) unit is presented. A novel method of SDL alignment and time delay calibration using a infrared (IR) laser setup was developed and successfully employed. The performance of Si(422) beam splitting optics was tested by X-ray topography measurements. The first results of the beam splitting optics under operating conditions of the SDL are presented. A single Si(422) beam splitter was studied in the typical experimental environment.

The SDL throughput and delay times were measured using synchrotron radiation of PETRA III. The time calibration of the setup with the novel Si(220) and Si(111) beam splitting optics was performed at 7 and 9 keV photon energies. The results are discussed and compared to the calibration data, obtained with the developed IR laser setup. The expected performance of the setup, presented in Chapter 2, is experimentally verified.

4.1 Laser-based time delay calibration

The split-and-delay unit splits a single FEL pulse into two fractions, introducing time delays between them on the pico- and femtosecond timescales. A precise alignment of the crystals and a measurement of the generated delay times are mandatory tasks prior to perform ultrafast experiments with FEL pulses. In order to reduce the alignment time during time-critical environments such as FEL sources, a laser-based optical measurement system was employed [115]. In this work such a laser scheme was further developed to measure and calibrate the time delay continuously. A major advantage of this technique is that it requires only simple optical components such as mirrors and collimators. The aim is to utilize this setup together with the SDL for the preliminary calibration and further measurements during X-ray experiments.

Figure 4.1 shows a conceptual scheme of the laser-based calibration setup. It consists of the low coherence IR semiconductor fiber superluminescent diode source, operating at the wavelength of λ=1550 nm. The bandwidth of the generated light is $\Delta\lambda$=50 nm, which corresponds to the longitudinal coherence length L_c and the coherence time t_c

$$L_c = \sqrt{\frac{2\ln 2}{\pi}} \frac{\lambda^2}{\Delta\lambda} = 31.9\ \mu m, \tag{4.1}$$

$$t_c = L_c/c = 106\ fs, \tag{4.2}$$

respectively, assuming that the source has a Gaussian emission spectrum [116].

The input laser beam is split by the fiber Variable Ratio Fiber-Optic Coupler (VRC) Newport Model F-C5-F2-543. The first fiber channel is guided to the fiber collimator FC1 located in front of the input window of the SDL. The fiber couplers FC1-FC4 can collimate the light from the fiber into air and back with a very small focal length shift. This method allows a precise laser beam alignment along the X-ray path through the fixed- and variable-delay branches at the same optical path. The Bragg crystal BR reflects the laser beam and the BS crystal acts as a wavefront splitter. Thus, the FC2 collimator receives a pair of the IR beams with the optical delay, which is to the first order equal to the X-ray delay time τ.

It is noteworthy, that the IR light is reflected from the surface of crystals, while the X-rays are diffracted from their lattice. Therefore, the X-ray optical path length is longer than the IR laser beam path due to the X-ray penetration inside a crystal to the extinction depth (see Section 2.1).

The second fiber channel from the VRC is connected to the collimator FC4. The gold mirrors are guiding a beam to the IR camera. Variable delay stages TS1 and TS2

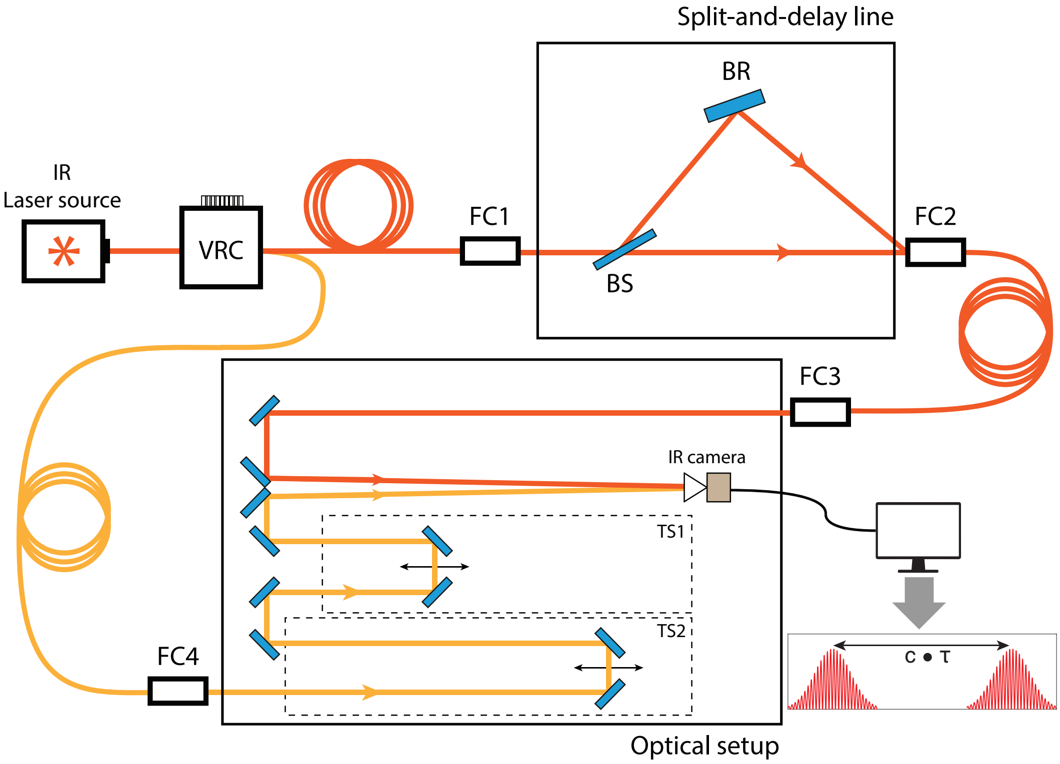

Figure 4.1: Sketch of an interferometry scheme implemented in the SDL setup. The IR laser beam is split by the Variable Ratio Fiber-Optic Coupler (VRC) and guided by the fibers and fiber collimators FC1-FC4 through the SDL and the optical setup. The path length difference is measured from interferometry patterns, registered by the IR camera while the TS1 and TS2 translation stages are moved.

can extend this optical path up to 1 m with discrete steps of 400 nm.

Both laser beams from the VRC channels are guided to the IR camera, which registers the sum of two signals. The optical paths inside the SDL (from VRC through FC1-FC3 to the IR camera) and the path in the optical setup (from VRC through FC4, stages TS1 and TS2 to the IR camera) act as the interferometer arms, respectively. Since the SDL arm consists of two separate beams (fixed- and variable-delay branches), two interference patterns will be observed by the camera in specific positions of TS2 stage, when the interferometer arms have the equal length. The difference between positions of TS2 stage, where the interference occurs, is equal to the path length difference between two IR beams inside the SDL.

The laser intensity distribution on the IR camera shows the interference pattern (see Figure 4.2) in the specific position of the TS2 stage, when the optical path through the laser setup is equal to the SDL fixed- or variable-delay branch paths.

The IR camera has a pixel size of 8.4×9.8 μm (H×W) and the CCD size of 768×494 pixels. The angle α between the two beams can be calculated from the fringe spacing according to [70, 117]:

$$\alpha = \arcsin\left(\frac{\lambda}{\Delta D}\right), \tag{4.3}$$

where ΔD is a fringe spacing. For the acquired interference patterns $\Delta D = 34$ μm, which results in an angle of $\alpha = 0.54$ arcsec between the beams.

The fringe spacing of any interference pattern of two waves depends on their amplitude, polarization and incident angles. In order to observe the interference fringes, several conditions must be met. The polarization of two beams must be the same and the relative intensities must be close in magnitude. In addition, the angle α between two beams must be set by the boundaries of the detection device, namely the pixel size and the CCD size, allowing the camera to distinguish the interference fringes. The angle α_{min} corresponds to the case, when the fringe size is comparable to the camera's pixel size. The maximum angle α_{max} has a limitation of horizontal CCD size, when two separate fringes still can fit to the CCD. Using the aforementioned values of the pixel size and the camera resolution, limits $\alpha_{\min} < \alpha < \alpha_{\max}$ can be defined as 0.006 arcsec $< \alpha <$ 2.186 arcsec.

The interference pattern can be observed only when the path length difference ΔL_{IR} between the two interferometer arms is within the longitudinal coherence length of the laser source. During the translation of the TS2 stage the emergence and disappearance of fringe patterns can be observed twice. These two events occur when the optical path length of the laser setup is equal to the SDL path length through the fixed- and variable-delay branch, respectively.

The pre-alignment of the SDL for future X-ray investigations was performed for two test conditions: a set of six BS and BR crystal configurations was calculated according to Bragg conditions for 7 keV and 9 keV (see Section 4.4). For each crystal

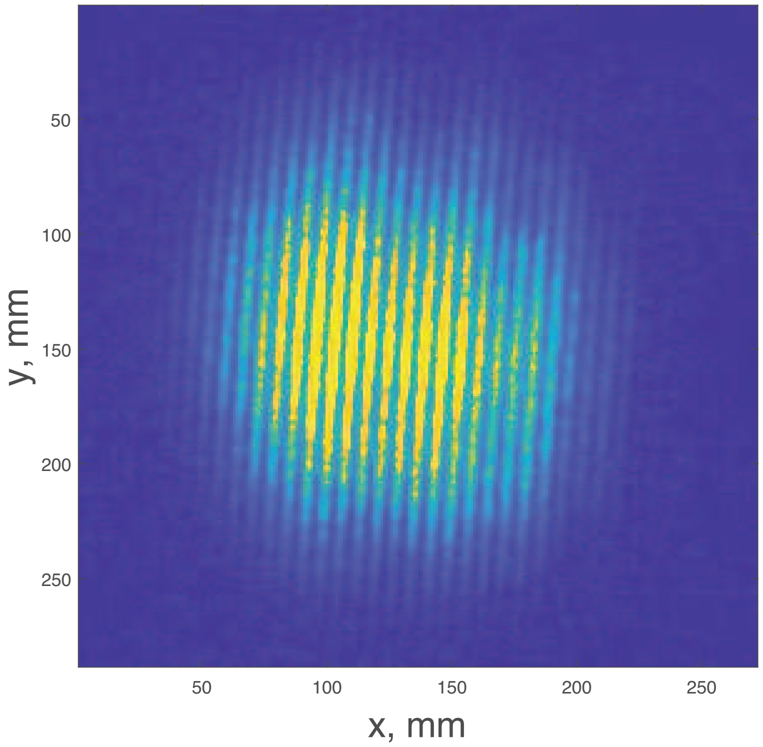

Figure 4.2: Interference pattern, recorded at the IR camera.

coordinate a laser-based time delay calibration was performed. The TS2 translation stage was moved with a step of 800 nm, acquiring the intensity patterns from fixed- and variable-delay branches of the SDL. For each TS2 scan ∼1800 images was recorded, showing the increase and decrease of fringes during translation of the stage. To analyze the fringe visibility, a oscillatory component was extracted from each recorded pattern (see Figure 4.3 a) by selecting a 1D intensity profile I_P (blue line in Figure 4.3 b).

In the second step, the profile I_{F} was calculated (red dashed line in Figure 4.3 b) from I_{P} by using the Savitzky-Golay filtering algorithm [118]. The intensity distribution I_{F} is a calculated intensity, which represents the sum of two non-interfering beams. This method allows to increase the signal to noise ratio of the data. The extracted oscillatory pattern $_{\mathrm{P}}/I_{\mathrm{F}}$ (see Figure 4.3 c) was used to calculate the fringe visibility V as

$$V = \frac{I_{\max} - I_{\min}}{I_{\max} + I_{\min}} \tag{4.4}$$

where $\mathrm{I}_{\max}$ and $\mathrm{I}_{\min}$ are maximum and minimum intensities of $\mathrm{I}_{\mathrm{p}}/\mathrm{I}_{\mathrm{f}}$ distributions, respectively. Figure 4.4 shows the visibility V as a function of the path length difference for both SDL branches. Each data point in the figure corresponds to the visibility of a single recorded pattern at a specific coordinate of the translation stage. The Gaussian fit (red curve on the plot) was used to get positions of the visibility peaks with full width at half maximum (FWHM) values of 41.5 µm and 44.3 µm for fixed- and variable-delay branches, respectively. The deviation of these coherence length from the calculated value in equation 4.1 could be caused by the low signal to noise ratio of the acquired data.

The uncertainty of each visibility peak is calculated from the fit and equals 0.14 µm. The corresponding delay time uncertainty is 0.5 fs. Such uncertainties of this measurement method are most likely caused by the camera noise.

Differences between the paths of the laser beam through the delay line (red path) and through the laser setup (yellow path) in the Figure 4.1 can be defined as ΔL_{IR1}

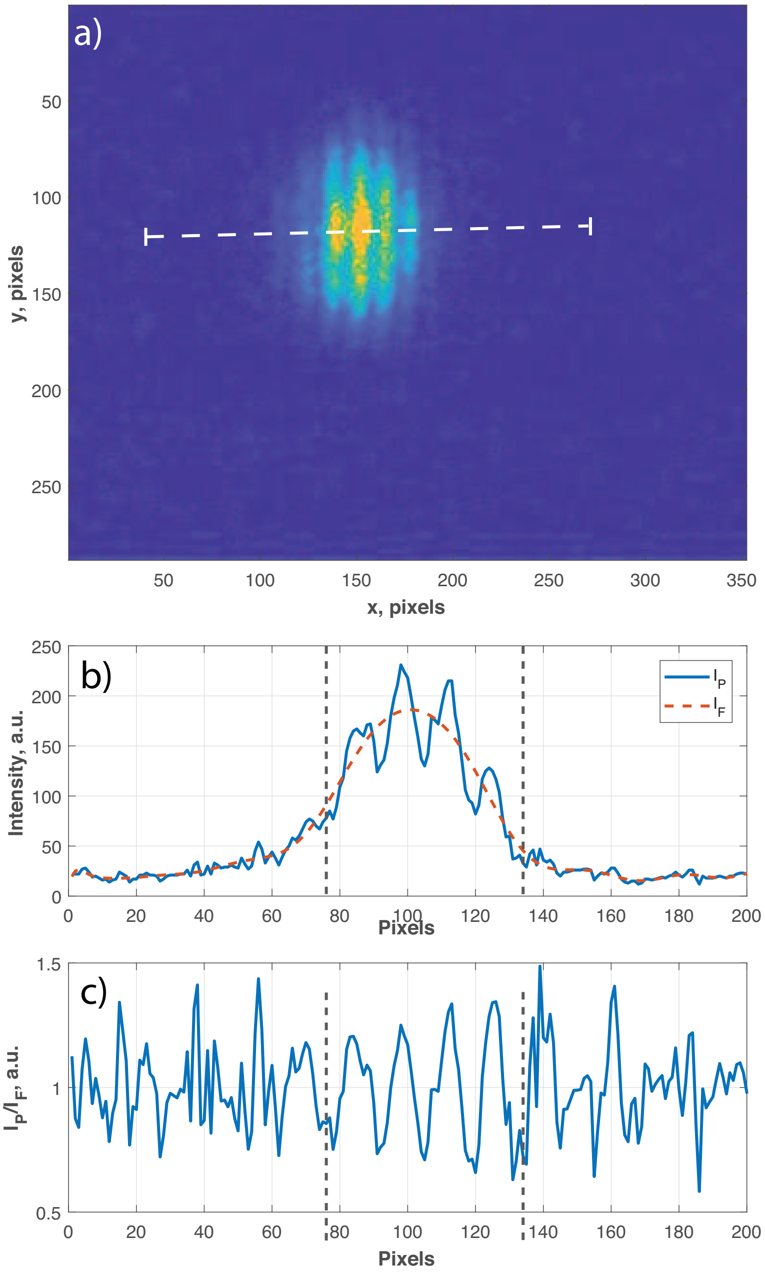

Figure 4.3: a) Selected 2D interference pattern with a line cut (white dashed line), showing 1D intensity distributions b) A 1D intensity profile I_P (blue line) and it's shape I_F after the filtering (red dashed line). The calculated I_P/I_F distribution c) is used for determining the fringe visibility V. Black dashed lines shows the part of the curve, where fringes from 2D pattern appear.

and ΔL_{IR2}, respectively. Thus, two visibility peaks in the Figure 4.4 have coordinates ΔL_{IR1} and ΔL_{IR2}, respectively, and the distance between peaks can be determined as

$$\Delta L_{IR} = \Delta L_{IR2} - \Delta L_{IR1} \tag{4.5}$$

During the X-ray experiment, the defined X-ray delay time ΔL between two successive X-ray pulses from fixed- and variable-delay branches of the SDL will be always equal to ΔL_{IR}.

In order to perform a delay time calibration of the setup, two sets of six configurations (12 in total) for 7 keV and 9 keV photon energies was generated by the motor encoders. Each configuration corresponds to specific X-ray delay times τ. For each configuration corresponding delay times were calculated (see dashed lines in Figures 4.5 a) and b) based on visibility peaks, obtained from interference patterns. Time delay values can be described by the linear function as

$$\tau = \frac{a}{c}\,\Delta L_{IR} + b, \tag{4.6}$$

where a and b are the fit parameters. The value of a is related to the precision of the SDL alignment as a function of ΔL_{IR}. In an ideal case $a = 1$, where c is a light

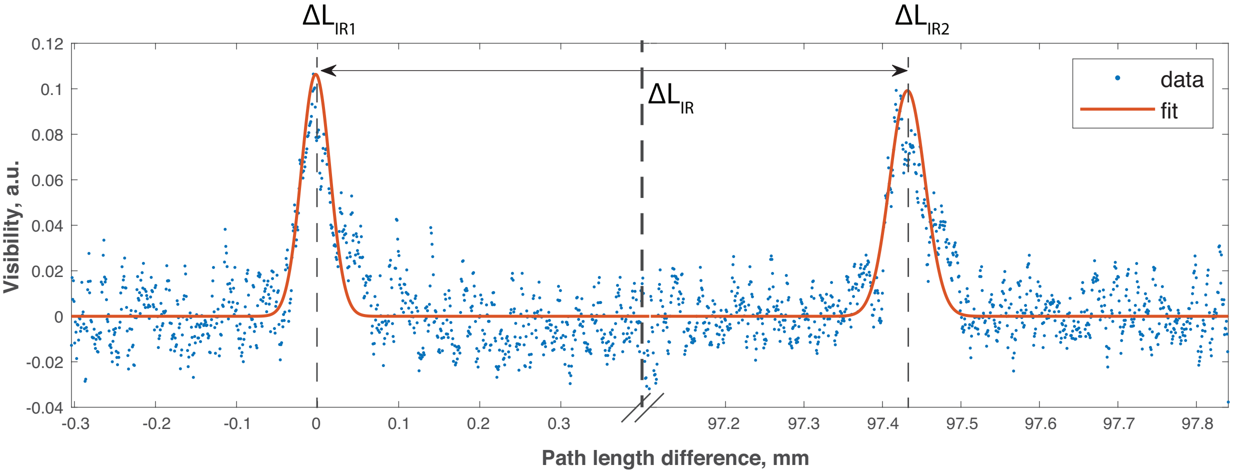

Figure 4.4: Fringe visibility V (blue scatter plot), extracted from the acquired fringe patterns. Red line represents the applied Gaussian fits with peak positions ΔL_{IR1} and ΔL_{IR2}, showed by the dashed lines. A path length difference ΔL_{IR} is calculated from the coordinates of visibility peak positions.

speed. Any deviation from this value can indicate non-perfect laser beam alignment with respect to the center of crystal rotations.

Additionally any mechanical imperfections (e.g. motor step precisions) will affect time delay calibration by changing the constant offset b. In order to quantify the precision of the alignment an additional beam path Δl can be implemented as

$$\tau = \frac{1}{c}(\Delta L_{IR} + \Delta l) + b. \tag{4.7}$$

The parameter Δl is a path difference between perfect and measured beam trajectories inside the delay line. The precision of the SDL alignment can be calculated from Equations 4.6 and 4.7 as

$$\frac{\Delta l}{\Delta L_{IR}} = a - 1 \tag{4.8}$$

which is equal to 0.12 and 0.15 for 7 keV and 9 keV measurements, respectively, describing the correction factors of the measured delay times. In total, temporal deviations from measured values are in the range of $12 < \Delta\tau < 22$ ps for 7 keV and $8 < \Delta\tau < 15$ ps for 9 keV photon energy. Thus, the measured data points have a time delay errors below 22 ps. This value is mostly determined by the resolution of the laser system and can be improved (see Section 5).

The fit parameter b represents a constant time delay offset of the measurement. For 7 keV and 9 keV this parameter equals 54 and 95 fs, respectively.

Overall results shows the clear linear relation of the measured path length difference ΔL_{IR} to the delay time τ, having up to 12% and 15% offset from the theoretical estimation for two photon energies, respectively. Measured data points are well described by the linear fit function, indicating the absence of any non-linear effects. This result promises successful operation of SDL in the X-ray based experiments.

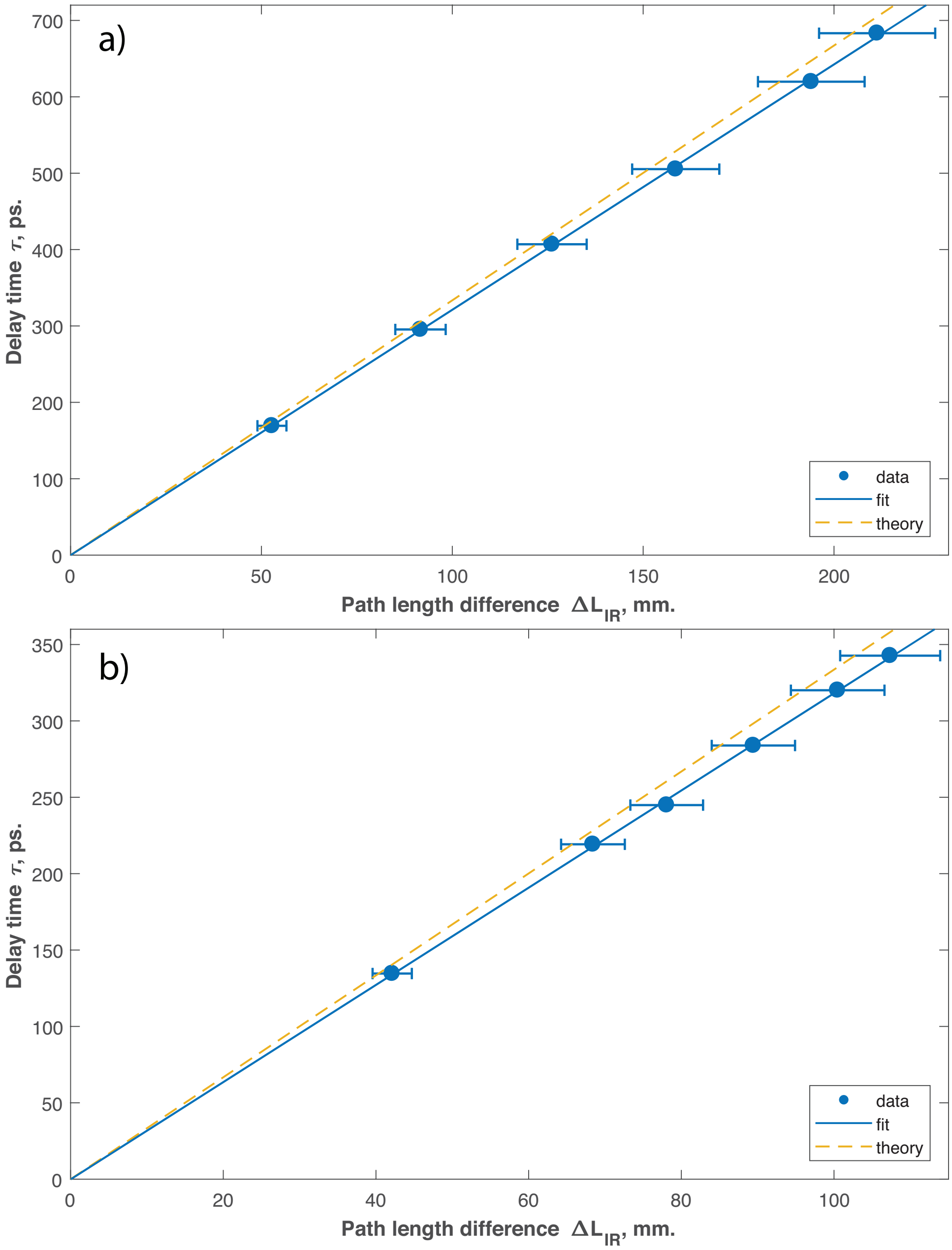

Figure 4.5: Measured delay time τ vs the applied path length difference ΔL_{IR} for a) 7 keV and b) 9 keV. The solid line is a fit to the measured data. The orange dashed line represents theoretical values of the delay times.

4.2 Beam splitting optics

Beam splitting optics plays a key role in the performance of split-and-delay lines. It should preserve the parameters (e.g. wavefront, intensity profile) of the incident beam and split it into fractions without compromising the beam quality (see Section 2.4.1). A thin PCVM Bragg beam splitter (see Figure 4.6 a) is used to employ the amplitude division (see Section 2.4.1) of incoming X-ray pulses in the SDL setup.

In section 4.2.1 a set of PCVM Si(422) beam splitters was investigated with X-ray topography. Experiments were performed at the BM05 beamline (ESRF) (see Section 3.6.1), which is dedicated to crystal topography and X-ray optics development. A set of beam splitters was characterized together with various mounting schemes: adhesive mount, and using the various types of holders in the holder assembly, shown in Figure 4.6 b). The motivation for this investigations is to estimate the crystal lattice quality and verify whether they can be used for beam splitting in the SDL setup.

The section 4.2.2 presents the first performance results of the beam splitting optics

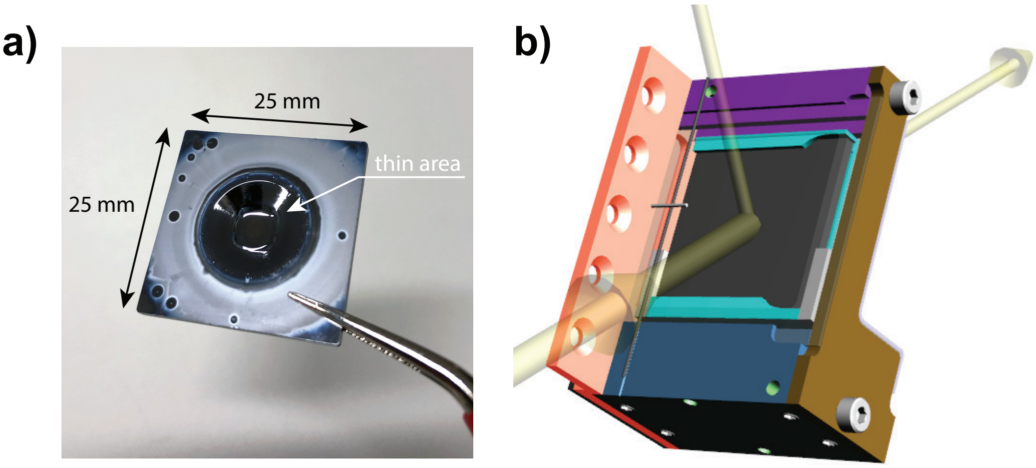

Figure 4.6: a) A photo of the Si(422) PCVM beam splitter. The crystal was mounted inside the assembly b) during the topography investigations.

under operating conditions of the beam splitter. The Si(422) PCVM beam splitter quality was evaluated while mounted on the 6-axis tripod in the helium housing, Strain propagation was examined by performing the high resolution topography scans at beamline P10 (PETRA III) (see Section 3.6.2).

4.2.1 X-ray topography

Four thin Si(422) Bragg beam splitters (here called: BS1, BS2, BS3, BS4) were investigated at beamline BM05 (ESRF) (see Section 3.6.1). The crystal lattice structure of each splitter was studied using the X-ray topography method (see Section 2.1.1) in combinations with different holders as listed in the Table 4.1. The crystals BS1, BS3 and BS4 have thick silicon frames (1.5 mm) and very thin central areas (<10 μm). The crystal BS2 has much thinner frame (0.5 mm) with a rectangular thin (<10 μm) area in the center. The splitter BS1 was mounted to the aluminium holder and fixed with a high bond strength adhesive "Crystalbond 509". This acetone-soluble solution provides excellent adhesion properties, having a viscosity of 2.16×10^7 kg/m·h and a melting point of 121 °C. The holder of the BS2 crystal consists of two aluminum square windows, holding the splitter in between, having direct surface contact with it. The crystals BS3 and BS4 were mounted to novel lightweight steel holders, which was designed to minimize any applied forces on crystals. This scheme provides a reliable fastening of the crystal without the use of adhesives or any clamping parts and minimizing the contact surface with the crystal. Small gaps of 0.1 mm between the splitter and the metal surface of clamping parts should prevent any excessive pressure on the crystal.

To investigate the crystalline quality of the BS1-BS4 crystals, series of topography measurements (see Section 2.1.1) were performed. Beam splitters were mounted on the diffractometer stage and illuminated with the 12×8 mm^2 X-ray beam according to the experimental scheme, shown in Figure 3.14. The beamline was operating at 15 keV photon energy with a Si(333) monochromator. For each of investigated crystal-holders (see Table 4.1) a series of 150-200 diffraction patterns were taken with angular steps of 0.36 arcsec. The diffracted intensity from each beam splitter was recorded with the exposure time of 1 s while the crystal was rocked within the range of angles $21.883<\theta_B<21.895°$. The diffracted intensity was captured by the FReLoN

Name	Crystal	Frame thickness	Clamping type	Holder
BS1	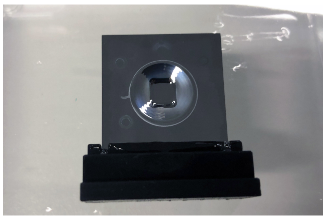	1.5 mm	crystalbond adhesive	 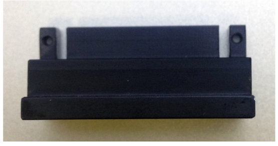
BS2	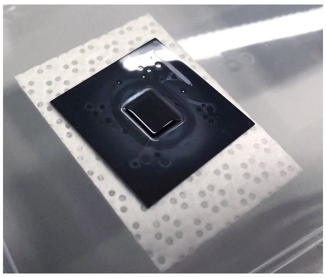	0.5 mm	aluminium clamp	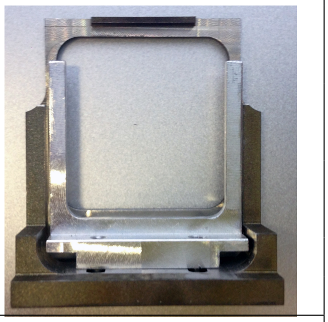
BS3	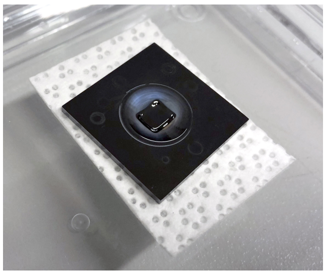	1.5 mm	lightweight steel	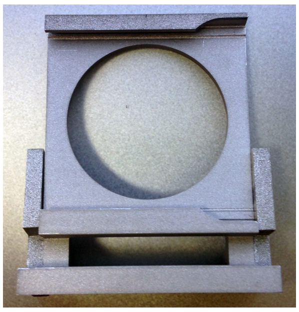
BS4		1.5 mm	lightweight steel	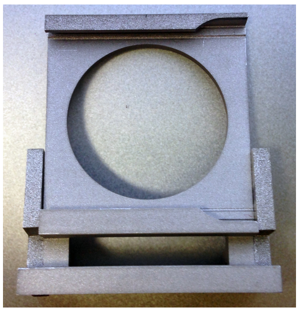

Table 4.1: Description of the PCVM crystals BS1-BS4 and corresponding holders, investigated at beamline BM05 of ESRF

camera [113]. A CCD sensor of the camera with 14 bit dynamic range has a resolution of 2048×2048 pixels and a pixel size of 14 microns. Selected diffraction patterns from BS1 and BS3 crystals are shown in Figure 4.7. The recorded 2D intensity patterns show the projection of the illuminated crystal area. Therefore, the obtained patterns had to be corrected to the initial geometrical dimensions.

To get more insight about the strain in every location of the crystal, topography maps with 16×10 µm^2 (H×W) resolution for each crystal were generated from the recorded rocking curves. Each map consist of the full width at half maximum (FWHM) values, calculated for the intensity in each pixel. Figures 4.8 (a, c, e, g) represents FWHM maps of the crystals BS1-BS4, respectively. Rocking curve from each pixel was fit by the Gaussian. The diffracted beam is a convolution of Si(422) beam splitter and Si(333) monochromator. To generate topography maps a parallel processing software was developed (see Section 3.3). It allows fast processing of the big amounts of diffraction patterns, registered by the camera, in order to generate the FWHM map of the investigated crystal. Typically, for every single FWHM map up to 4×10^6 fits has been calculated. The FWHM value from each fit is stored in each single pixel of the maps in Figures 4.8 (a, c, e, g). Areas marked by red squares correspond to the thinnest part of crystals. Structural defects that are present inside these areas, indicating the presence and behaviour of the lattice imperfections. Distributions of the peak intensity of the Bragg curves for the crystals BS1-BS4 at the Bragg angle θ_B=21.8°, are shown

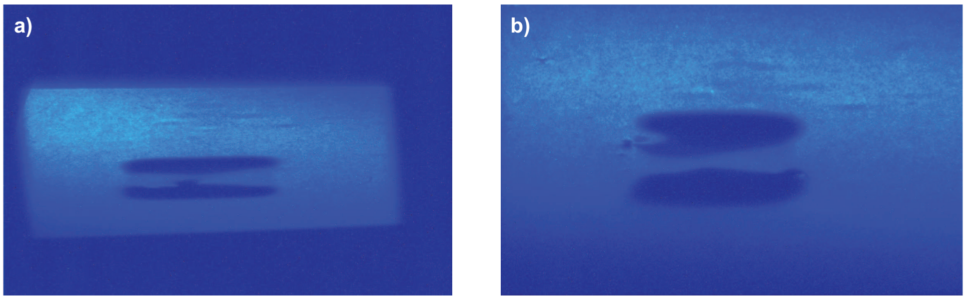

Figure 4.7: Example of the 2D intensity profiles of the diffracted beam obtained from a) BS1 and b) BS3 crystals. Intensity profile of BS3 was reshaped to the initial crystal dimensions.

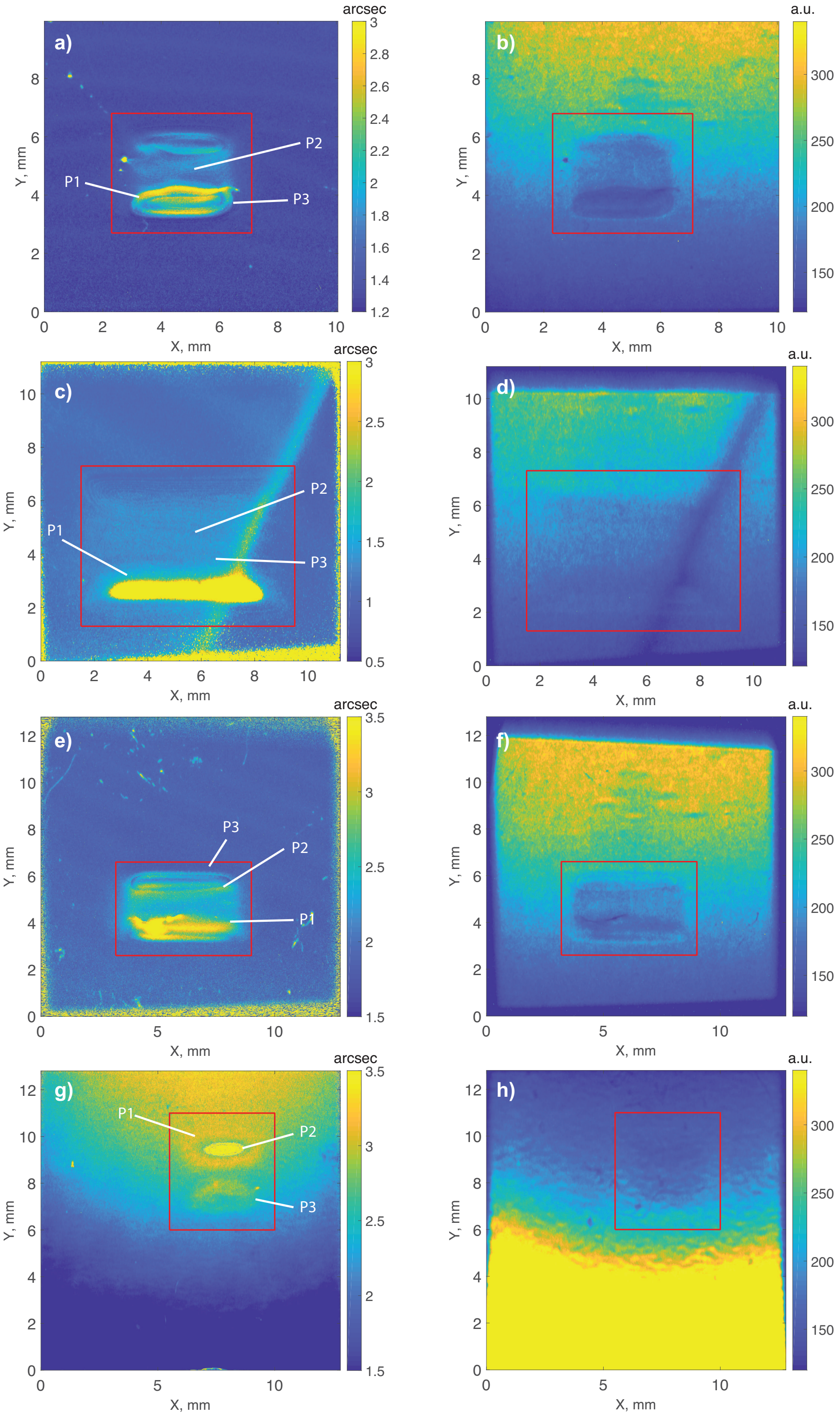

Figure 4.8: FWHM maps of the investigated beam splitters BS1-BS4 are shown on a), c), e), g), respectively. Maximum intensity maps b), d), f), h) represent the peak intensity of the Bragg curve at the angle $\theta_B = 21.8°$ in every pixel for respective crystals. The red square shows the thin area of the crystal, involved in the beam splitting.

in Figures 4.8 (b, d, f, h) respectively. For thin beam splitters the thickness of the diffracting area is related to the diffracted intensity as it is shown in Figure 2.12 in Section 2.4.1. The thinner parts of the crystal diffract less intensity which is indicated by the respective thickness deviations in the crystal lattice (see Figure 4.8 (b, d, f, h).

To estimate the overall crystal quality the FWHM maps were analysed. Rocking curves corresponding to points P1, P2 and P3 (see Figure 4.8 a, c, e, g) are represented by the blue, red and yellow curves in Figures 4.9 (a-d). The violet curve represents the diffraction curve from the bulk crystal frame. The dashed line shows a convolution curve of the beam splitter-monochromator crystals configuration, calculated for 15 keV photon energy. It has a FWHM value of 1.4 arcsec, which is very close to the value for the measured bulk crystal diffraction curve of 1.41 arcsec. Rocking curves of crystals BS1-BS3 show a clear angular shift of the peak position.

A broadening and the shift of the Bragg curve can occur when the crystal lattice has internal deformations, caused for instance by internal lattice strain. The peak intensity is also changing relative to the FWHM, which is also clearly visible on respective intensity maps (see Figure 4.8 b, d, f, h). The distribution of the FWHM values in the central thin area is represented by the histogram shown in Figure 4.10. The crystal BS2 has the highest crystalline quality, as indicated by the closest FWHM value to the theoretically expected 1.4 arcsec. The crystal BS1 has a lower intensity histogram peak with an FWHM value of 1.75 arcsec. Histograms of BS3 and BS4 have a broad distribution of FWHM ranging from 2.26 to 2.59 arcsec and from 2.6 to 3 arcsec, respectively. This can be explained by the presence of the stronger crystal lattice strains, compared to the crystals BS1 and BS2.

The crystal BS2 shows the best performance in terms of FWHM values. This crystal is the only one with the 0.5 mm thin outer frame. Other crystals have a 1.5 mm thick frame. The thick crystal frame can cause an additional strain to the thin area, indicated by the broadening of the reflection curve and decreasing the peak intensity. In this context only the BS1, BS3 and BS4 crystal holders can be compared to each other. Crystal BS1 with the adhesive mount shows the best result, as shown in Figure 4.10.

Overall the results from all four beam splitters show the wide distribution of the lattice quality. FWHM values from 1.3 to almost 4 arcsec can be explained by the deviations of the BS1-BS4 lattice quality. The beam splitters with the rocking curves which are closer to the theoretical value are preferable for applications in SDL X-ray

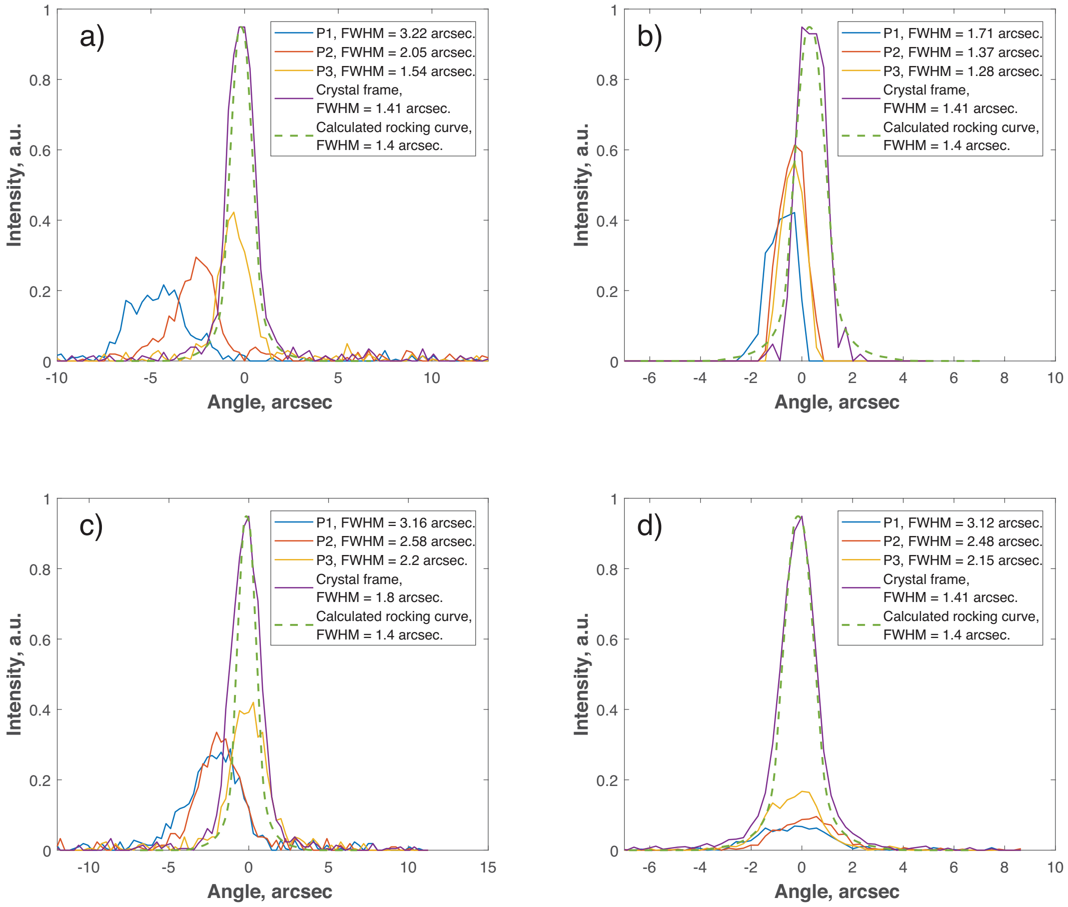

Figure 4.9: Rocking curves obtained from the crystals BS1 (a), BS2 (b), BS3 (c) and BS4 (d). Blue, red and yellow plots corresponds to the thin splitting area region (inside the red square on Figure 4.8), the violet curve represents the Bragg diffraction curve from the bulk crystal frame. Green dashed line shows the reflection curve of the perfect bulk Si(422) crystal.

experiments. Based on the obtained topography maps the best areas should be chosen for the splitting. The quality of a thinnest splitting area have crucial impact on the beam quality at the sample and on the splitting ratio in the case of possible thickness deviations. Thus, further investigations are required, for instance, the measurements of the same crystal with different holders. From the obtained topograms the influence of holders can not be distinguished from intrinsic crystal lattice strains.

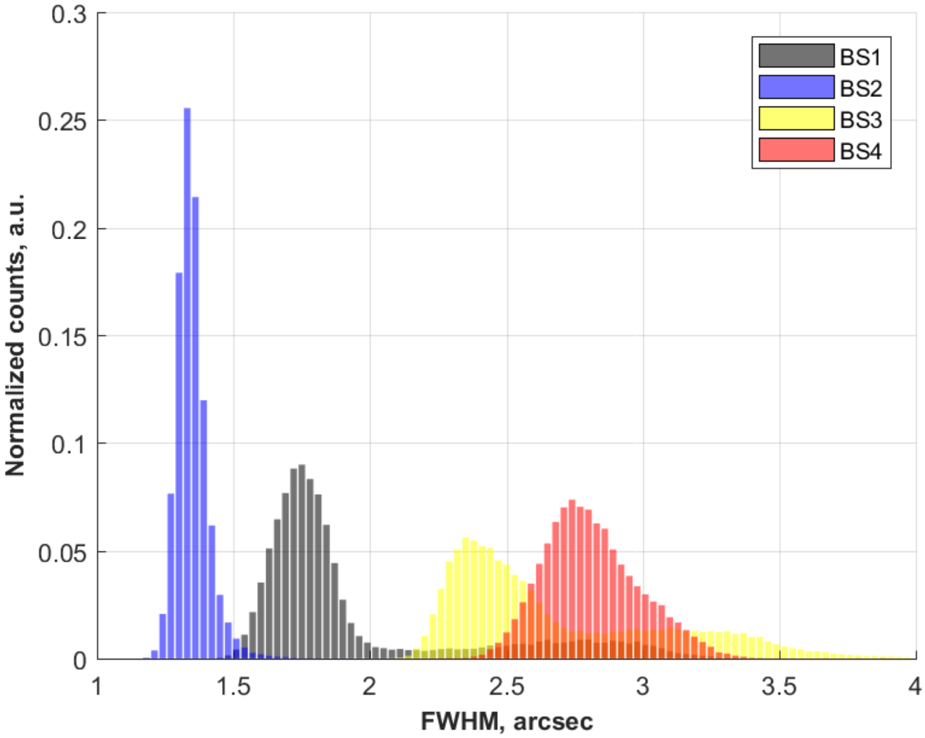

Figure 4.10: Histogram of FWHM values in the thin area from the investigated beam splitters.

4.2.2 Performance of the beam splitter unit

Before utilizing the SDL setup in FEL experiments, a test of the beam splitter unit under typical experimental conditions is required. The Si(422) PCVM beam splitter with the 1.5 mm thick frame was mounted in the helium chamber on the 6-axis tripod, in the same way as it will be employed in the SDL setup. The performance of the beam splitter unit under typical operating conditions was simulated at the P10 beamline of PETRA III (see Section 3.6.2). The beam splitter unit was filled with helium to prevent oxidation, reduce intensity losses and dissipate heat from X-ray radiation. The crystal quality was examined by performing high resolution scanning topography [119] using a 0.6×0.3 mm^2 coherent beam. The investigated crystal was mounted to the holder (see Figure 4.11 a). A series of high-resolution diffraction patterns was obtained while the crystal was rocked on the 6-axis tripod (see Figure 4.11 b). The experiment was performed using a Si (333) premonochromatized beam at the 7.9 keV photon energy. The tripod stage is able to move in three directions and rotate around three axes with

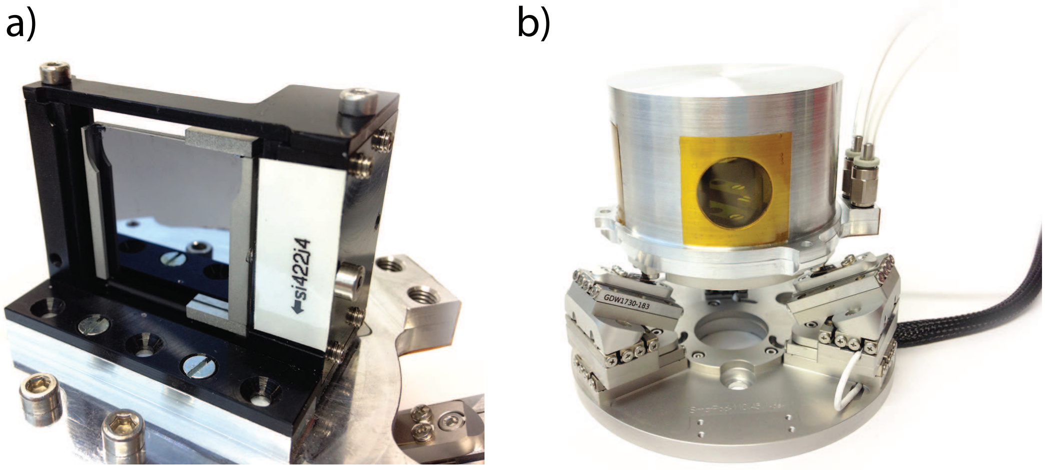

Figure 4.11: a) crystal, mounted at the novel holder, b) crystal 6-axis tripod with the helium chamber on top.

a precision of 1 nm (see Section 3.1). The crystal was scanned with 1 arcsecond steps around the Bragg angle θ_b=45.06° to obtain the intensity distribution in diffraction geometry. To rock the crystal a hexapod and a HUBER 6-Circle diffractometer were used. For registering the diffracted intensity a PCO Edge detector was mounted on the top arm of the diffractometer in the Bragg geometry.

The data was acquired in selected areas of the crystal, generating an array from 70 crystal regions. Diffraction patterns from the selected areas were stitched according to the geometrical coordinates, resulting in diffracted intensity distribution maps as

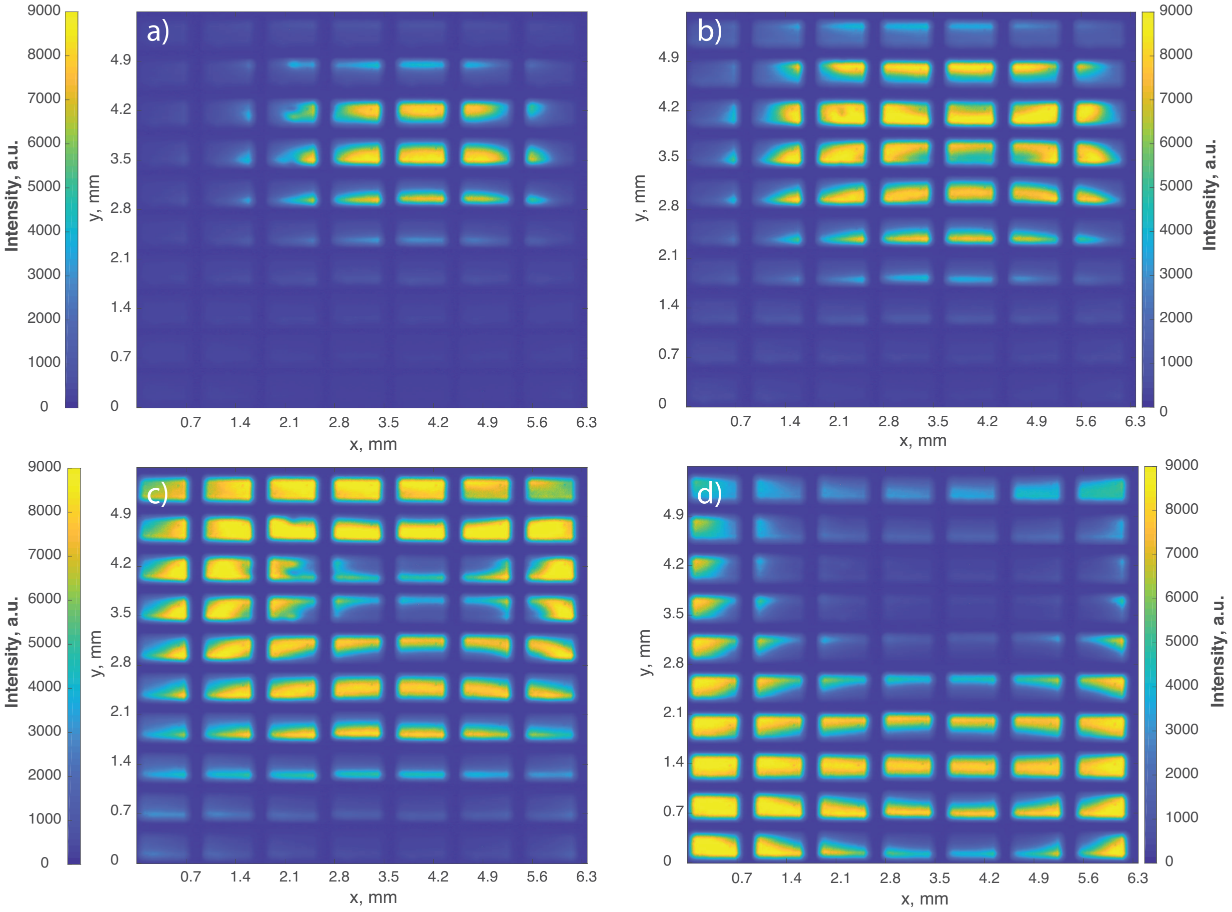

Figure 4.12: Diffraction patterns measured from the beam splitter in symmetric Bragg geometry as a function of $\Delta\theta = \theta - \theta_B$, where θ and θ_B are the incident and Bragg angles, respectively. $\Delta\theta$ equals to a) -0.0012° b) -0.0006° c) 0° and d) 0.0006°.

shown in Figure 4.12.

The rocking curves from the different areas of the investigated crystal were obtained and analyzed resulting in the FWHM map shown in Figure 4.13. It provides the information on the crystal quality of the beam splitter. Area A, marked in the figure, is chosen as a best area of the crystal. It has a FWHM of 4.5 arcsec while the average value for the whole crystal is equal to 4.74 arcsec. These numbers can be compared the theoretical Bragg curve FWHM of 2.76 arcsec as it shown in Figure 4.14. The dashed curve represents the convolution of the Si(111) monochromator and Si(422) curve.

For further SDL X-ray experiments a region with the best quality can be defined on the thin area of the crystal. The beam splitter has a strong point-like defect on the left top corner (see Figure 4.13) with the coordinates approximately x=2.1 mm

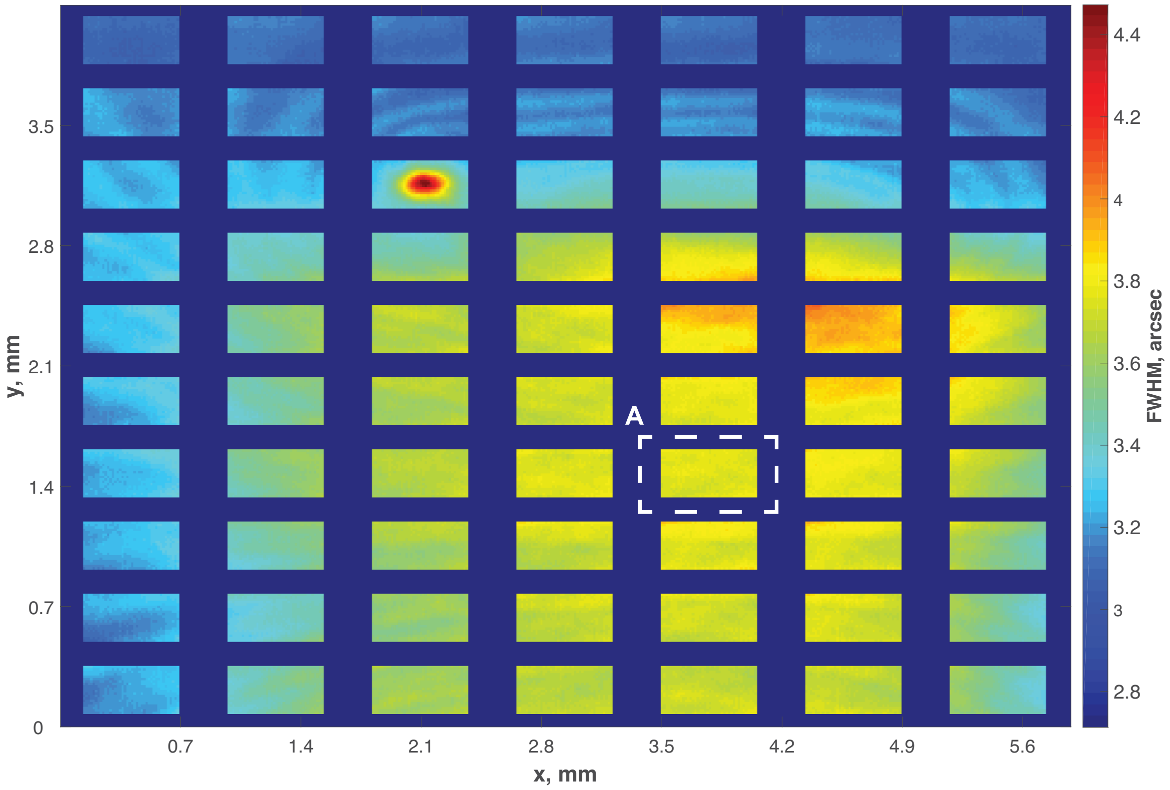

Figure 4.13: FWHM scanning topography map of the beam splitter.

y=3.15 mm on the FWHM map. This defect is located outside the splitting area and can be neglected. Moreover, the broadening of the Bragg curves is visible in the area x=3-5 mm, y=2-3 mm. Preferable areas for the splitting can be defined using the FWHM based on the beam size value over the selected region.

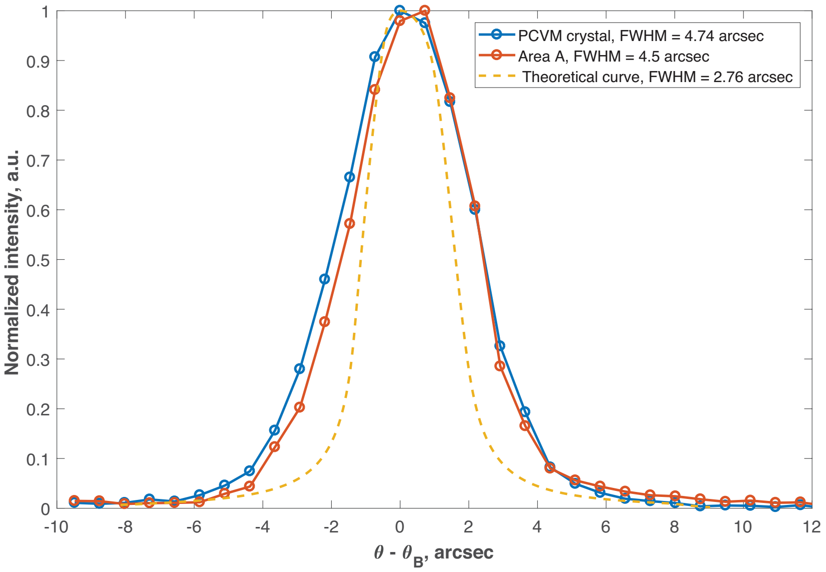

Figure 4.14: Comparison between the average rocking curves from the whole measured area (blue line), a selected area A (red line) and the theoretical Si(333)-Si(422) Bragg curves convolution at 7.9 keV photon energy (dashed line).

4.2.3 Si(220) splitting performance

For the X-ray investigations a Si(220) PCVM beam splitter was used. The quality of this crystal was investigated at the P64 beamline (PETRA III). A detailed description of the beamline can be found in Section 3.6.3. The SDL was mounted in the experimental hutch behind the exit slits as shown in the Figure 4.15. The beam was pre-monochromatized by the Si(111) channel-cut, yielding an energy resolution of the incoming beam of $\Delta E/E = 1.4 \times 10^{-4}$ (see Table 2.2).

The SDL was positioned on the optical table in the horizontal scattering plane, as shown in the Figure 4.16. Between the ionization chamber and the setup, a 100 cm vacuum pipe was mounted to minimize the photon losses in air. The beam splitter is located after the entrance window of SDL and surrounded by Hamamatsu S3590-09 Silicon PIPS diodes in the fixed- and variable-delay branch directions (see Section 3.1). These diodes were used to measure the rocking curves of the beam splitter using the incident beam photon energies of 8 keV and 9 keV. The crystal was rocked with an angular step of 1 arcsec and the diffracted and transmitted intensities was registered by the respective diodes. The obtained rocking curves are shown in Figure 4.17 are

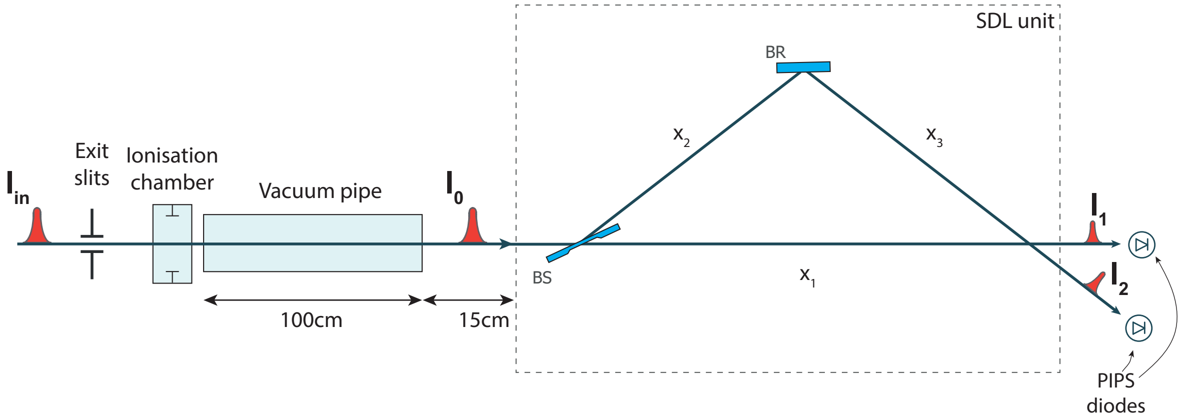

Figure 4.15: Sketch of SDL positioning at the P64 experimental station.

compared to the theoretical calculated distributions (dashed lines). Since the incident beam was pre-monochromatized before the SDL, the diffracted beam should have an intensity distribution corresponding to the convolution of Si(111) monochromator and Si(220) crystal.

At 8 keV and 9 keV photon energies the diffracted beams have a FWHM of 12.6 arcsec and an FWHM of 10.3 arcsec, respectively. Theoretical FWHM values for this configurations are equal to 10.6 arcsec and 9.2 arcsec. These results show a good beam splitting performance according to the estimations presented in Section 2.4.1.

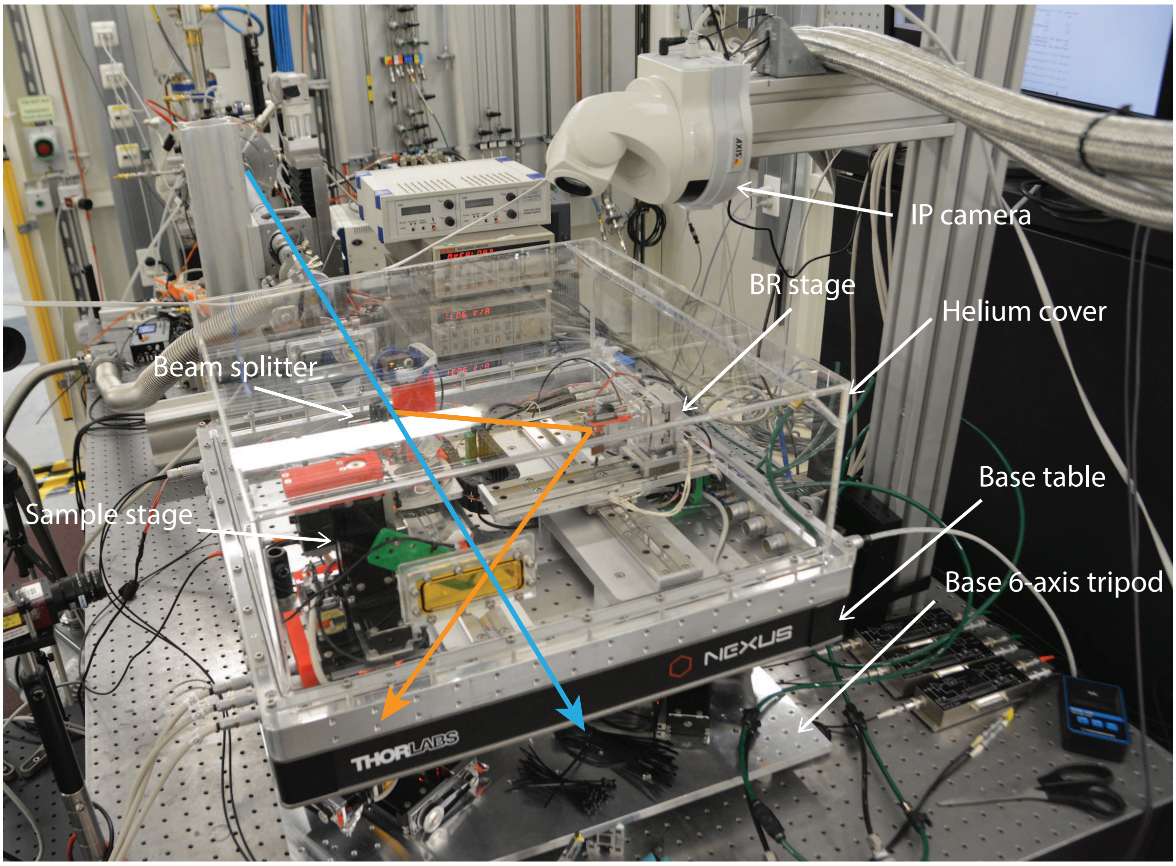

Figure 4.16: The SDL setup in the P64 experimental hutch. Blue and orange lines denote the main and reflected beam propagation path accordingly.

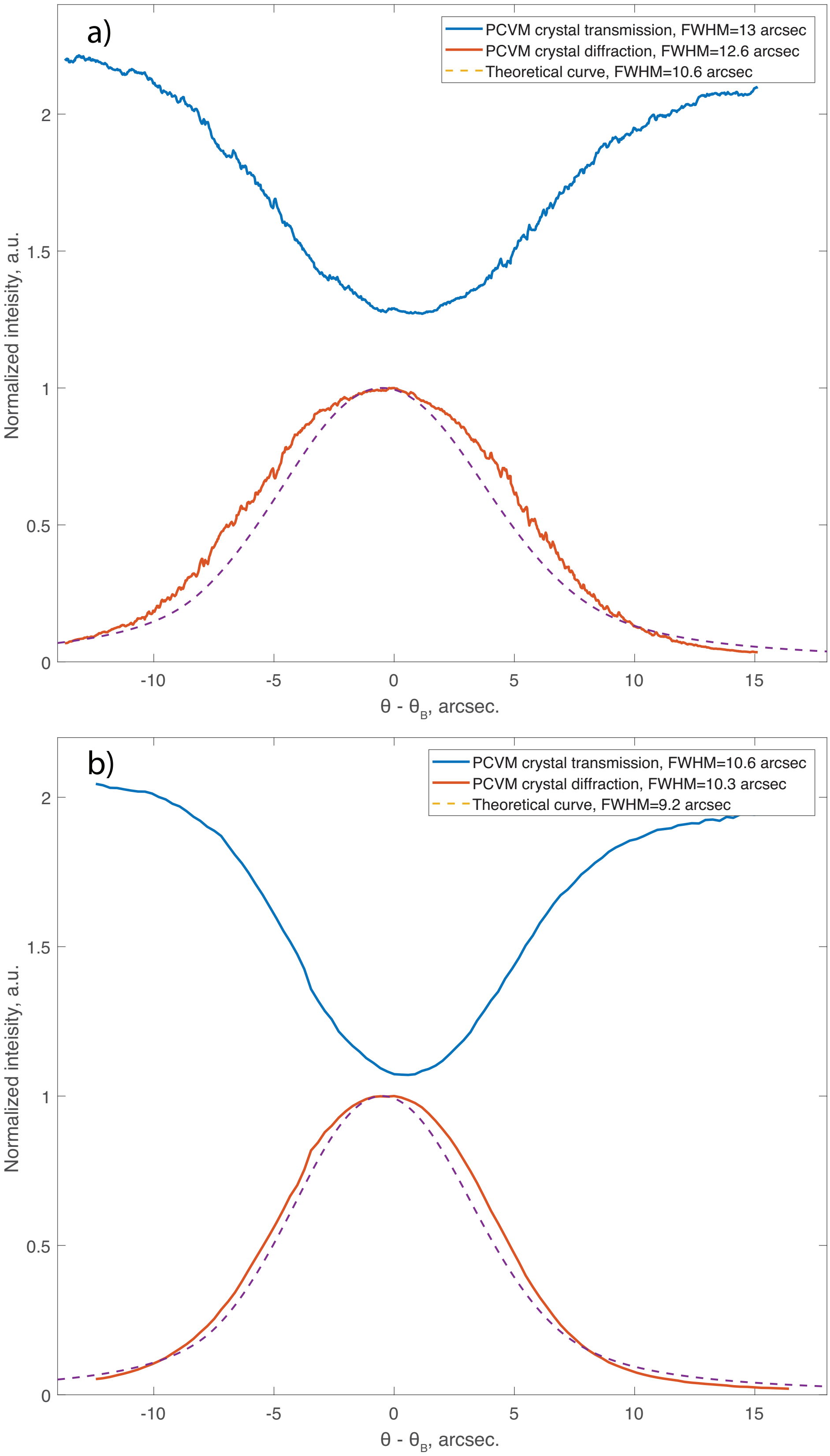

Figure 4.17: Measured rocking curves of the Si(220) PCVM beam splitter at a) 8 keV and b) 9 keV photon energies. Blue and red curves represent transmitted and reflected intensities, registered by PIPS diodes. The dashed line shows the theoretical rocking curve of the crystal.

4.3 Throughput measurements

To estimate the performance of the SDL, quantitative measurements of the device throughput were performed at the P64 beamline (PETRA III) using the configuration, presented in Section 4.2.3. An X-ray beam with photon energy of 7 keV and the size of 0.5×0.5 mm^2 was used. After the beamline exit slits, a 5.5 cm long ionization chamber filled with N_2 at the pressure of 760 torr was mounted to measure the input flux. The N_2 gas absorption values are listed in the Table 4.2. The intensity downstream the SDL was registered by a Hamamatsu S3590-09 Silicon PIPS diode [109]. The X-ray transmission of the SDL was investigated with air and helium atmosphere. To align the base table in the horizontal plane parallel to the beam, a 6-axis tripod (see Section 3.1.3) was implemented below the SDL (see Figure 4.16). This device is able to hold the whole unit and move it with a 1 µm linear and 0.4 arcsec angular step resolution.

An optimum alignment of the main beam spitter translation stage along the X-ray path was achieved by using the X-ray beam position monitor (XBPM). The device is mounted on top of the beam splitter stage (See Figure 4.18 a). Beam position tracking is achieved by moving the stage along the main beam path and tracking the position of the beam spot on the fluorescent screen, located at 45° with respect to the XBPM

Energy, keV	7	9
Ionisation chamber N_2 absorbtion losses, %	7.29	3.43
Ionisation chamber conversion counts conversion value, $\times 10^6$ photons/count	3.676	6.078
Linear absorption coefficient µ for air, cm^{-1}	0.0339	0.0158
Linear absorption coefficient µ for helium, $\times 10^{-5}$ cm^{-1}	3.94	3.33

Table 4.2: Ionisation chamber parameters and linear absorption coefficients of air and helium for 7 keV and 9 keV photon energies.

camera. It has a 3.75 µm^2 pixel size and together with the lens it gives a resolution of 3 µm.

Throughput calculations of the P64 experimental setup, including the ionization chambers, vacuum pipe and the beam path through the air was made according to a scheme, shown in Figure 4.15. The delay line was operating with the Si(220) thin PCVM beam splitter (BS) and Si(422) beam reflector (BR). The incoming flux value was measured by the ionization chamber, amplifying the output current signal by current-to-voltage amplifier Keithley 428.

The ionization chamber is filled with a gas and two collecting electrodes: the anode and cathode (the anode is positively charged with respect to the cathode). When the gas between the electrodes is ionized by the incident radiation, ion-pairs are created and the resulting positive ions and dissociated electrons move to the electrodes of the opposite polarity under the influence of the electric field. This generates an ionization current in the amounts defined by the chamber size and the gas medium. The photon flux value can be calculated [120] as:

$$\Phi = \frac{VE_i}{eEk}, \tag{4.9}$$

where V is the measured output voltage, E$_i$ is the ionization energy of the gas (32 eV for N_2). The value e corresponds to the electron charge (1.6×10^{-19} C) and E is the

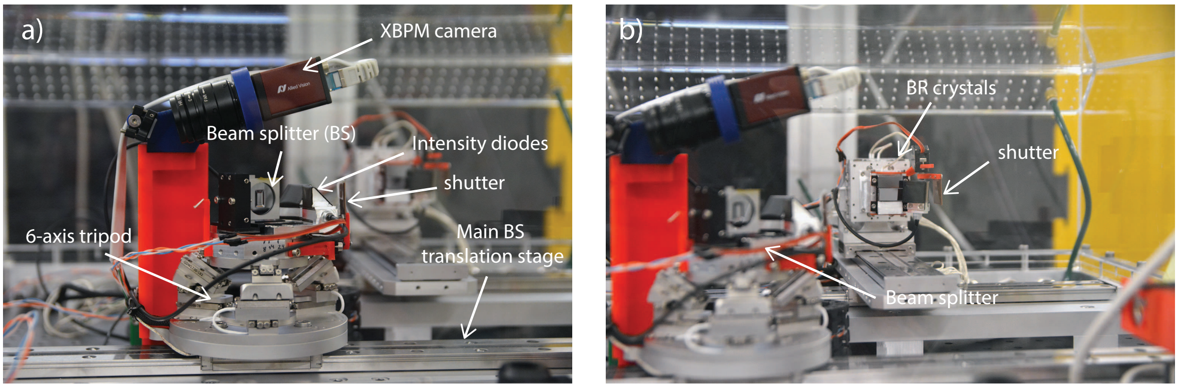

Figure 4.18: Beam splitter (a) and the BR crystal (b) stages with mounted crystals at the P64 beamline.

photon energy. The coefficient k is the amplification gain of the current-to-voltage amplifier. The voltage signal was amplified by Keithley 428 as 1 V of the registered signal corresponds to the 10000 counts. The total number of photons was calculated using the conversion values listed in Table 4.2.

After the ionization chamber and before the SDL a vacuum pipe was placed (see Figure 4.15) to minimize the photon losses. The transmission of this pipe was calculated as $I = I_0\ e^{(-\mu x)}$, where x is its length. The values for linear absorption coefficient μ for the different photon energies are listed in the Table 4.2.

Theoretical throughput values were calculated by multiplying the transmission values of all components on the propagation way of the beam. Thus, for the fixed-delay branch in the pump-probe mode the throughput can be defined as:

$$T_{FB} = \frac{I_0}{I_1} = e^{-\mu x_1}(1 - \frac{\Delta E_{BS}}{\Delta E_{source}})(1 - A_{BS}), \tag{4.10}$$

where ΔE_{BS} and ΔE_{source} are the energy resolutions of the beam splitter and the input beams, respectively. The parameter μ corresponds to the linear absorption coefficient for helium and x_1 is the flightpath distance (See Figure 4.15), respectively. The absorption due to the beam splitter is A_{BS}. Intensity values of fixed- and variable delay branches at the output are equal to I_1 and I_2, respectively.

For the upper branch it is necessary to include the reflectivities of the Bragg crystals and the horizontal synchrotron polarization:

$$T_{VB} = \frac{I_0}{I_2} = e^{-\mu(x_2+x_3)}\frac{\Delta E_{BS}}{\Delta E_{source}}R_{BS}cos^2(2\theta_{BS})\frac{\Delta E_{BR}}{\Delta E_{BS}}R_{BR}cos^2(2\theta_{BR}), \tag{4.11}$$

where ΔE_{BR} is the energy resolution of the reflecting crystal, R_{BS}, R_{BR}, θ_{BS} and θ_{BR} are the reflectivity values and the Bragg angles of the beam splitter (BS) and the second crystal (BR) respectively. The flightpath distances x_2 and x_3 are shown at Figure 4.15. Factors $cos^2(2\theta_{BS})$ and $cos^2(2\theta_{BR})$ denote the reduction of incident intensity due to the horizontal polarization of X-rays in the synchrotron.

Together, the overall throughput of the SDL can be defined as:

$$T = I_0 e^{(-\mu_a x_1)} T_1^2 T_2^2 (T_{FB} + T_{VB}), \tag{4.12}$$

where I_0 is the intensity on the output from the ionization chamber, μ_a is the linear absorption coefficient for air. T_1 and T_2 are the throughput values of the kapton windows with the respective thicknesses of 25 μm and 100 μm, respectively. Air absorption in this configuration corresponds to 31.3% and 23.5% in the variable and fixed-delay branches respectively. Calculated and measured values of the throughput are listed in the Table 4.3.

The measured fluxes for the air and helium atmosphere agree well with the calculated values. This indicates a proper operation of the device and all its optical components. Delay time performance measurements in same configurations for 7 keV and 9 keV are presented in the next section. In order to obtain a higher throughput, a further experiment in vertical orientation of the SDL must be performed.

	Calculated throughput, %	Calculated flux, photons/second	Measured flux, photons/second
Helium atmosphere			
Upper branch	0.2	6.95×10^{8}	5.48×10^{9}
Lower branch	48.26	1.4×10^{11}	5.84×10^{10}
SDL setup	48.46	1.4×10^{11}	6.39×10^{10}
Air atmosphere			
Upper branch	0.14	4.08×10^{8}	1.16×10^{9}
Lower branch	37.5	9.1×10^{10}	1.39×10^{10}
SDL setup	37.64	9.14×10^{10}	1.5×10^{10}

Table 4.3: The calculated and measured values of throughput and flux for the air and helium atmosphere at 7 keV using synchrotron radiation.

4.4 Delay time measurements

To measure the performance of the SDL device in generating time delays a set of measurements was performed at 7 and 9 kev photon energies. Measuring the delay times produced by the device requires fast photon diagnostics. Therefore, two fast avalanche photodiodes (APD) were mounted at the output of the device to count photon arrival times. Figure 4.19 a) shows a scheme which was used for the data acquisition. APD signals were amplified and sent to a Constant Fraction Discriminator (CFD). The CFD device filters out the noise and provides the applicable signal for the Time-to-Digital Converter (TDC). It is synchronized with the bunch clock signal from the PETRA III synchrotron ring. This signal is used as a start reference point for the TDC to measure the photon arrival time signal from CFD with respect to the bunch clock. Furthermore, the pulses are digitized by an analog-to-digital converter (ADC) and stored in a multichannel analyzer. Afterwards the signals were recorded by the computer.

From each of the 40 bunches in PETRA III storage ring the photon pulses were registered in the time spectrum plot (see Figure 4.19 b). Each incoming X-ray pulse is split to a pair of pulses, produced by the SDL. The experimental data from the corresponding photon events is shown in Figure 4.20 a).

The histograms shown in Figure 4.20 b) represents the main (violet) and delayed (green) pulse photon distribution pairs, registered by the APD's. The bin width corresponds to the time resolution of the detection system (Δt = 100 ps). Each pair of curves was fitted using an asymmetric Gaussian fit as represented by the red and violet lines, respectively. Maximum intensity $I_{\max}$ and the standard deviation σ in the plot are shown for each curve, respectively. The delay time τ was calculated as a difference between the maxima of these two curves.

The resulting distribution of events recorded by APD corresponds to the distribution of detecting a photons in each Δt interval. The overall resolution of the measurement is defined by the FWHM of the measured distribution pattern. It shows a slight asymmetry due to the initial photon beam structure, and can be described by an

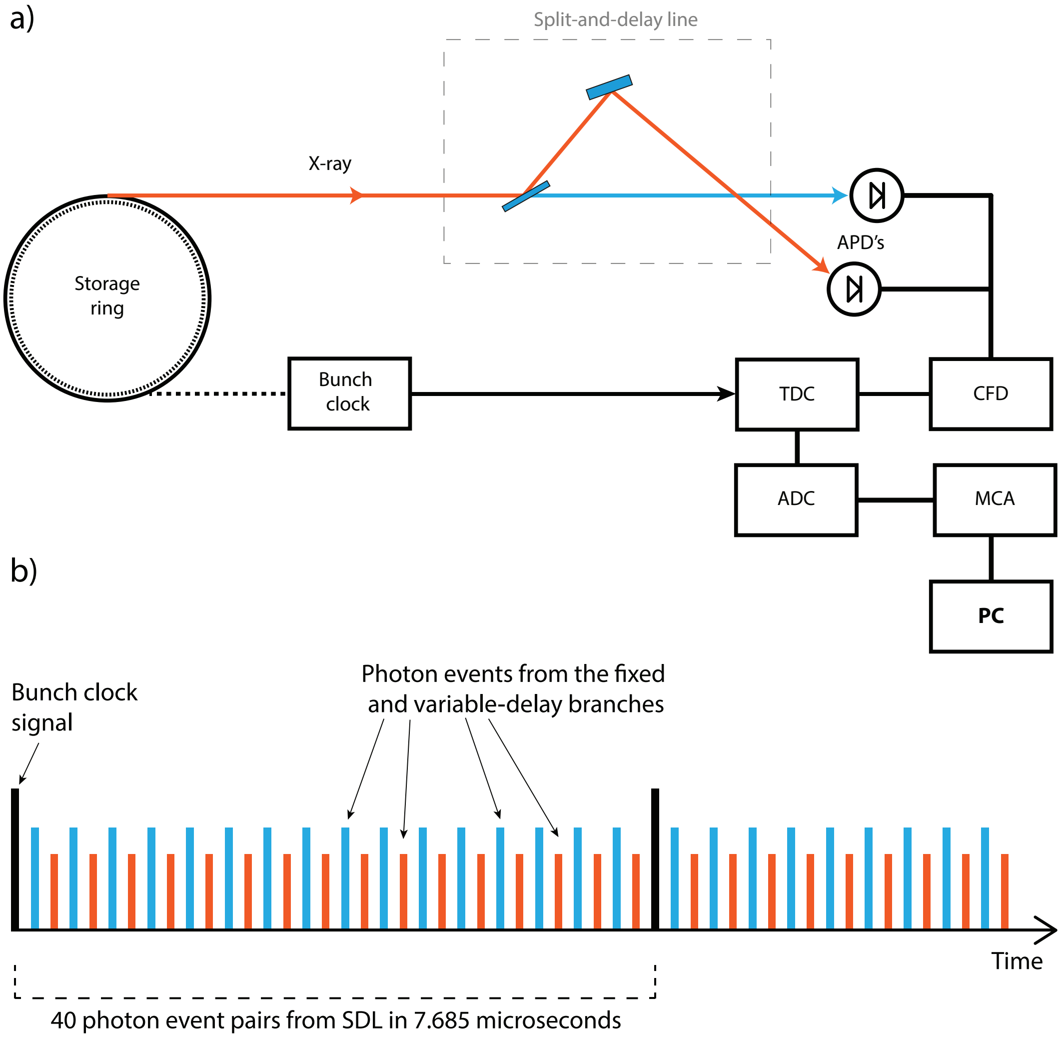

Figure 4.19: a) Scheme of the data acquisition during the delay time measurements and b) sketch of the signals, arrived from the bunch clock and the photon events at the APD position

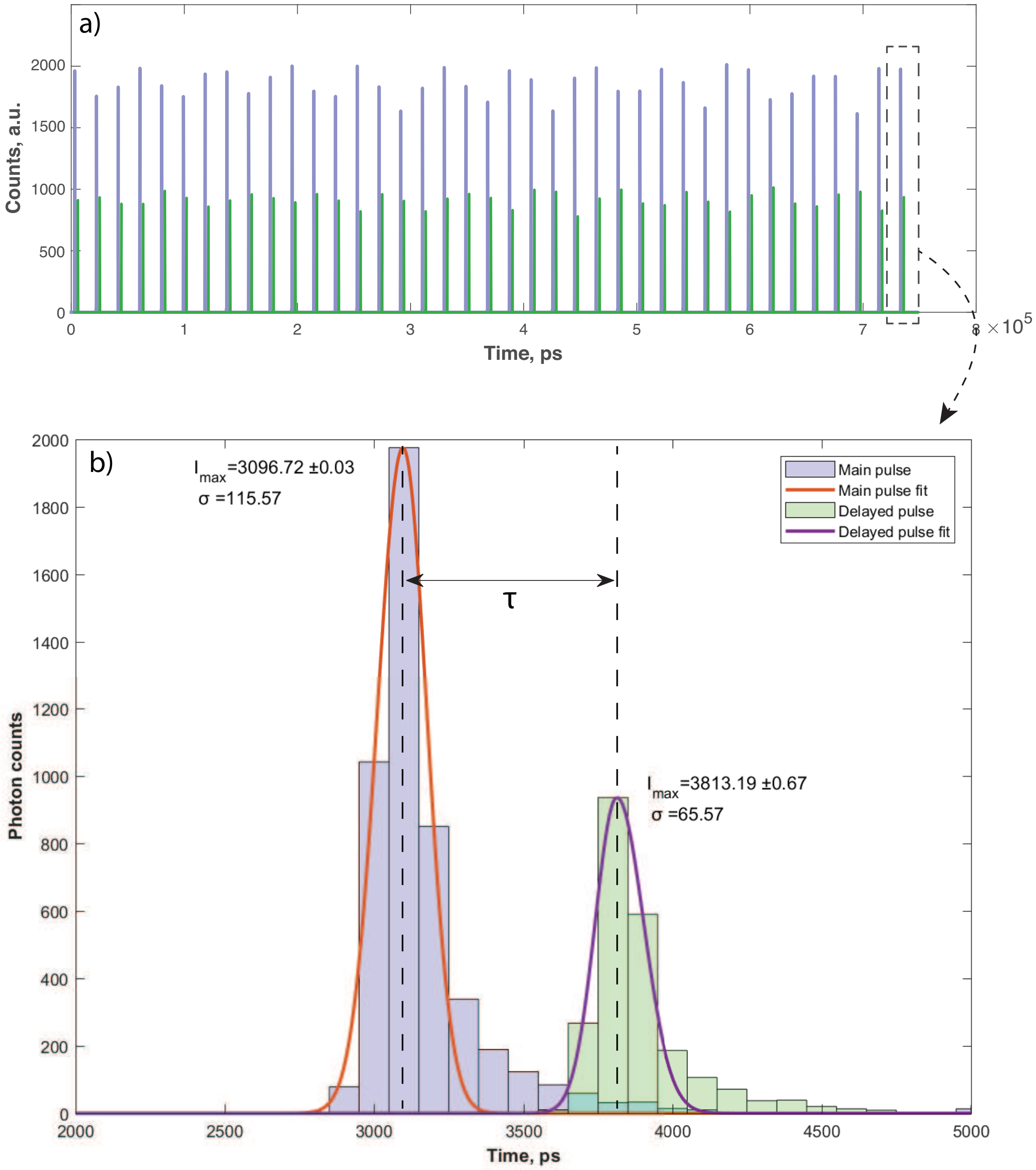

Figure 4.20: a) A set of the registered signals, registered by the APD's from the fixed- (violet) and variable (green) delay branches. Zero time coordinate corresponds to the bunch clock signal. Selected pair of pulses (b) is fit by the Gaussian curves (red and violet curves). Time delay τ is a difference between the peak positions.

asymmetric Gaussian function with the peak position t_0 defined by

$$f(t) = A \cdot \begin{cases} \exp\left(-\frac{(t-t_0)^2}{2r^2\sigma^2}\right), \text{ if } t \leq t_0 \\ \exp\left(-\frac{(t-t_0)^2}{2\sigma^2}\right), \text{ if } t > t_0, \end{cases} \tag{4.13}$$

where r is the asymmetry parameter. The variable σ is a standard deviation, which is related to the time resolution Δt (FWHM) as $\Delta t = \sqrt{2\ln(2)}\sigma(1+r)$. The parameter A corresponds to the maximum intensity in the peak position t_0.

For every successive pair of photon pulses a fit function can be expressed as

$$f(t) = f(t_1) + f(t_2), \tag{4.14}$$

where f is the asymmetric Gaussian fit function (see Equation 4.13). The total delay time between the two pulses can be obtained as a time difference between the positions of peaks on the plots, since both pulses are registered with respect to the bunch clock signal. The uncertainty of the peak position is calculated from the fit function.

Calculated and measured delay times are shown in Figure 4.21 for the energies of 7 keV (a) and 9 keV (b). The obtained errorbars are smaller than the size of data points. In total, the delay times $201 < \tau < 716$ ps for 7 keV and $130 < \tau < 370$ ps have been measured for 7 keV and 9 keV, respectively. The delay time was changed by the parallel movement of the BS and BR crystals with respect to the diode position. The arrival time of the photons from the both branches is changing as a function of the path length difference. According to the relative positions of the crystal stages a theoretical delay time was calculated. The precision of a SDL alignment can be calculated by the value $\Delta l/\Delta L$.

A fit to the data was performed with the linear function (see Equation 4.6). The values of precision of the SDL alignment $\Delta l/\Delta L$ (see Equation 4.8) are 0.05 and 0.003 for 7 keV and 9 keV, respectively, showing the excellent precision of the performed measurement. Values of the coefficient b are 8.51 ps and -6.39 ps for the aforementioned energies, respectively. The time delay differences between the measured data points

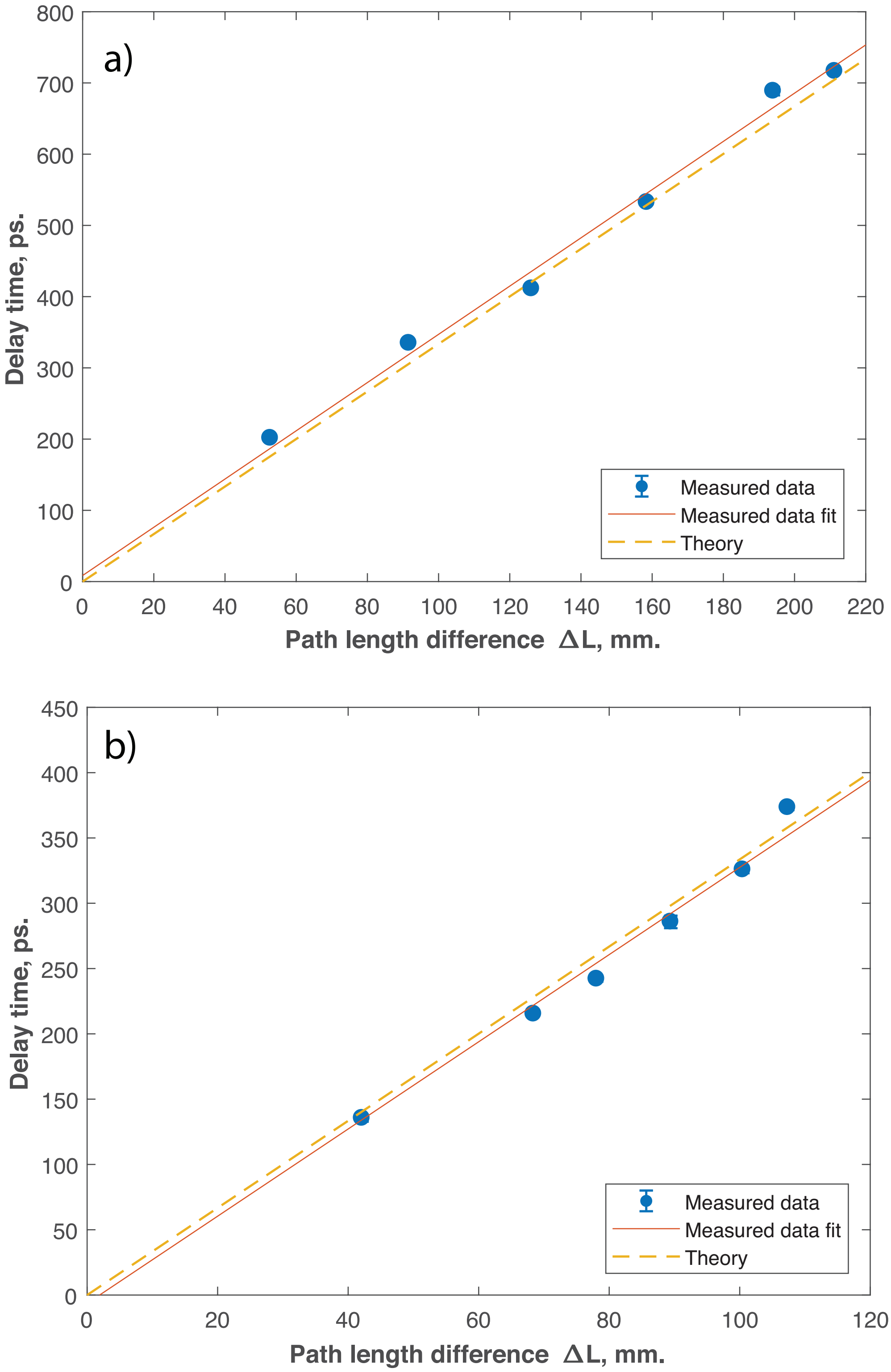

Figure 4.21: Measured and calculated delay times with corresponding fits at E=7 keV (a) and E=9 keV (b).

and expected delay time values is shown in Figure 4.22. Average deviations of the delay time $\Delta\tau$ are equal to 20 ps and 12.3 ps for 7 keV and 9 keV, respectively. Thus, the total mean error of the presented measurements is equal to 16.2 ps.

Figure 4.23 shows combined results from the laser calibration, presented in the Section 4.1 and the X-ray data from the current section. Both measurements were performed at the same BS and BR coordinates, as it is shown in the Figure 4.23. This allows to compare the data points for each separate delay time. The best precision of laser and X-ray measurements for 7 keV was observed with 12 ps and 3.5 ps temporal errors for the IR and APD detection systems, respectively. For 9 keV these values are equal to 8 ps and 5.1 ps, respectively, which shows the better precision of APD diodes rather than laser measurements.

The vertical shift of the data fit from the theoretical dashed curve indicates the presence of the constant offset rather than the progression of the error with increasing the path length difference. One of the main reasons for these offsets can be the deviation

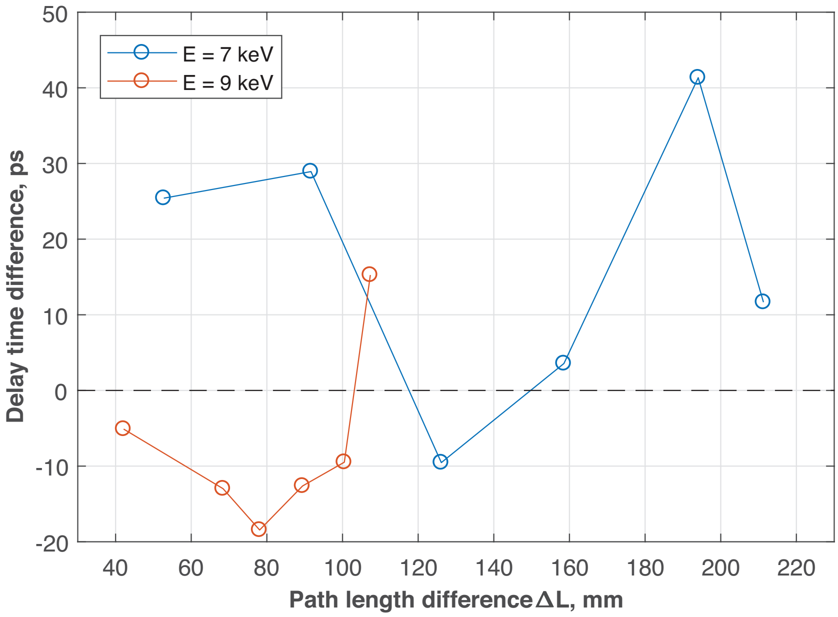

Figure 4.22: Difference between measured and calculated delay time values for 7 keV and 9 keV

of the relative angle between the BS and BR crystals. As far as they are not mechanically connected one to each other, the reflected BS beam to the variable-delay branch can reflect from the BR crystal not precisely in the center, generating a bigger uncertainty of the path length difference and delay. The crystal is 5 mm wide, which gives a ±2.5 mm range, where the offset can be generated. Geometrically it gives a ±6.9 ps and ±17 ps of additional delay at 7 and 9 keV, respectively. These estimations indicate that the range of the measured data have an additional deviation. To improve the precision of measurements, for instance, additional X-ray apertures can be implemented in the SDL.

Apart from the geometrical deviations, the X-ray optical path always will be different from the laser path due to the penetration of X-rays to the diffracting crystal. Symmetric Bragg extinction length can be calculated from the equation 2.9. For Si(220) beam splitter and Si(422) BR crystal the extinction length L_{ext}^{Bragg} is giving an additional delay time of 48 fs as a constant difference in path between the fixed- and variable-delay branch.

In summary, data sets are showing very good linearity. The measurements provide good calibration background for further X-ray investigations. Delay time errors, obtained during X-ray investigations, are comparable to performance results of similar devices. For instance, a hard X-ray delay line, which was developed for fixed energies at DESY [16], reported about the mean error of 16.7 ps. Mean error of the presented investigation method for the designed device is equal to 16.2 ps. This resolution does not represent an intrinsic property of the delay line. The precision can be improved, for example with use of a higher resolution detection system.

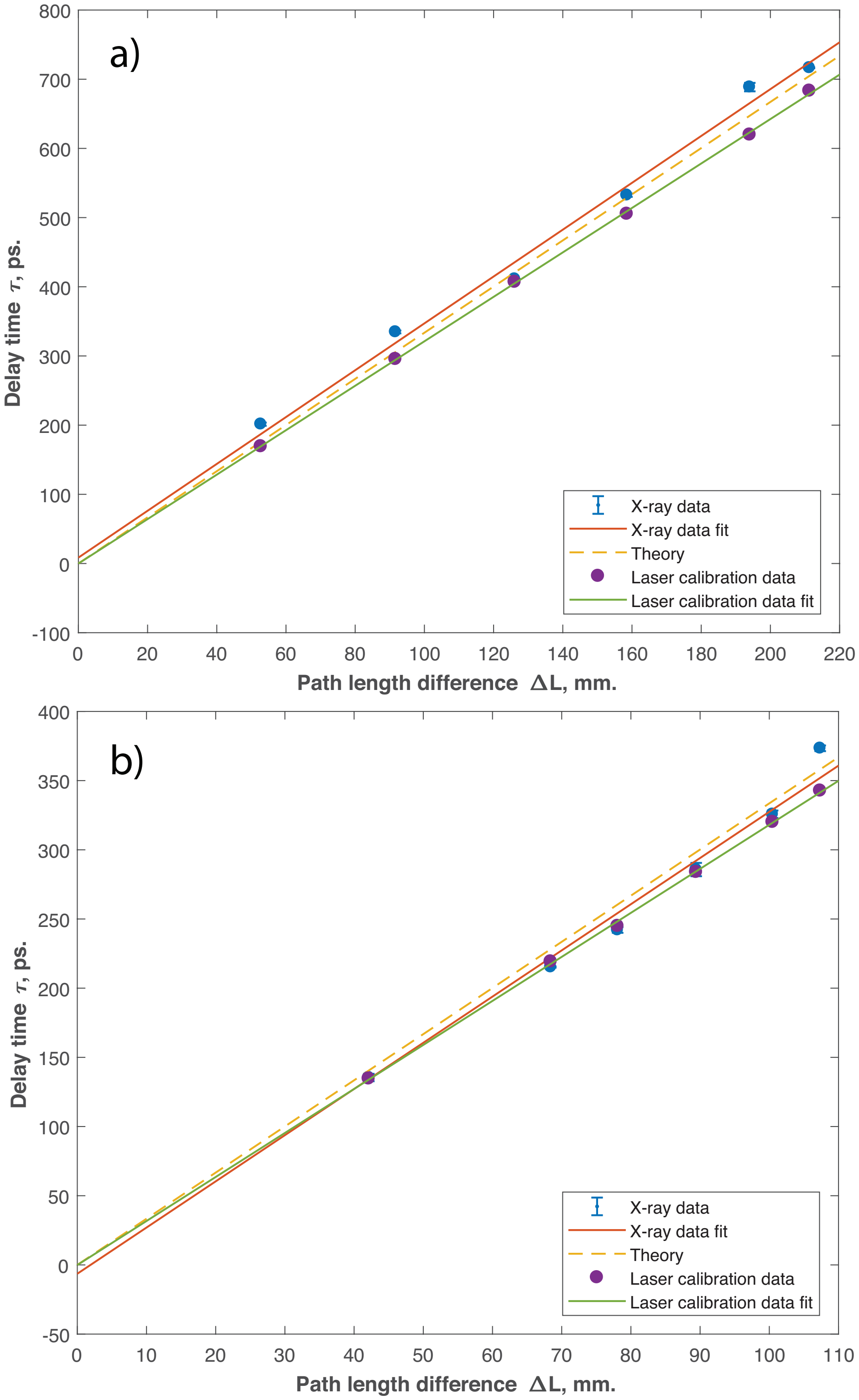

Figure 4.23: Delay times with the fits at the energy (a) 7 keV and (b) 9 keV obtained with the laser calibration, X-ray measurements and theoretical estimations.

Chapter 5

Outlook

The compact hard X-ray device was developed to operate in the energy range from 7 keV to 16 keV. The SDL performance was tested at 7 kev and 9 keV photon energies with help of a laser calibration setup. Future development and possible improvements of the SDL components are discussed in this chapter. Improvements of the Bragg optics and diagnostic tools can potentially increase the throughput, precision and capabilities of the setup, enabling new research opportunities at FEL sources.

Bragg optics

The quality of the employed Bragg optics was investigated and tested (see Section 4.2). Thin Si(220) PCVM beam splitters are used in amplitude division mode, providing a high quality diffracted beam. However, residual strain is observed in the topography measurements. Presently it is not known if this is intrinsic or arises from the holders. Detailed studies of single beam splitter with various holders should be performed to improve the obtained results.

Amplitude division is the default method which is used to divide the incoming pulse into two fractions. As an alternative, wavefront division can be optionally employed as the splitting mechanism. It can be achieved by inserting a sharply polished reflective crystal edge into the incident beam [17, 18, 117]. The setup mechanics is designed to include this option as a future development of the SDL setup.

Germanium can be used as an alternative material for the BS crystal optics and channel-cuts CH1 and CH2. According to the Table 2.2 it has a lower energy resolution and can improve the overall throughput of the device more than a factor of 2. Unfortunately, it is difficult to obtain precisely polished crystals from Germanium, especially with the high indices of reflection (i.e. Ge(220) and Ge(422)). It might however be possible in the future with surface nanomachining [121].

Another option can be diamond Bragg optics. This material has the highest reflectivity, but a narrow energy resolution window. With a narrow Bragg curve this type of optics is harder to align, however, the transmitted flux will be almost 3 times higher as compared to silicon.

Mechanical components

The main crystal stages are based on piezo motors which are nowadays regarded as the most advanced positioning technology (see Section 3.1). They provide nanometer precision (see Table 3.1) and exceptionally small sizes which makes them difficult to improve. However, by decreasing the weight of holders and supplementary parts on the movable stages, the precision and positioning speed can be improved. Such results can be achieved by using light materials such as plastics for general applications and titanium for precise holders and mechanisms.

Diagnostics tools

The SDL setup has robust and simple diagnostics tools which are well-studied and easy to operate. PIPS diodes and XBPM monitor are serving mainly for alignment and relative measurements. The PIPS diodes can be exchanged by the diamond intensity monitors [122], which can serve as the absolute intensity measurement tool. The graphite detector could also be used as a beam position monitor although with rather coarse resolution.

Resolution of the setup

A laser setup was built for time calibration of the SDL (see Section 4.1). Currently it is operating with a semiconductor laser source with 300 mW laser power. Since the setup consists of numerous mirrors, fibers, collimators etc., power losses have a significant influence on the resulting intensity of the interference pattern. According to the measurements, temporal errors of the delay time of $\Delta\tau <$22 ps were obtained. This result can be improved by increasing the visibility of fringes by having a better interference contrast. This can be achieved by increasing the intensity of the laser source as well as decreasing the amount of optical components in scheme. Increasing the laser power can help to distinguish interference fringes and reduce the camera noise, resulting in the higher precision of the delay time alignment. A smaller coherence length of the source will lead to sharper visibility peaks and improving signal-to-noise ratio. Moreover, two stages TS1 and TS2 can be exchanged to a single long stage for scanning the whole delay time range simultaneously. An improved scheme of the laser setup is shown in Figure 5.1.

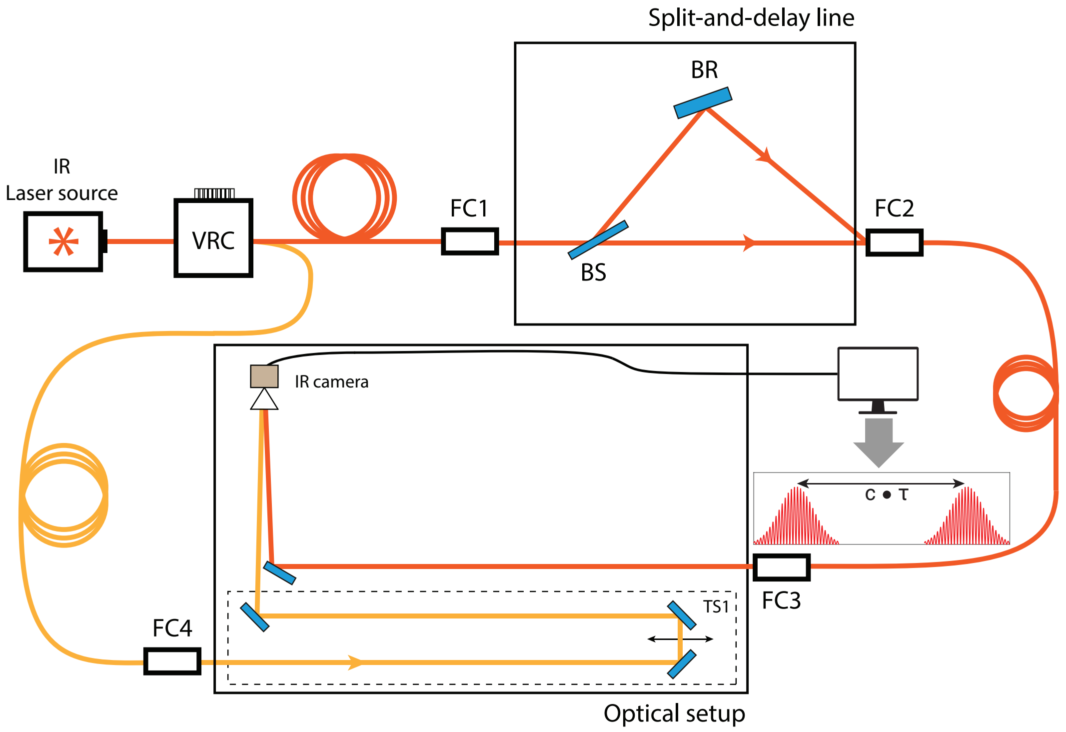

Figure 5.1: Sketch of the improved and simplified interferometry scheme.

Chapter 6

Summary and conclusions

This thesis work presents the concept and the technical design of a compact split-and-delay unit. The device is capable of splitting FEL pulses in the hard X-ray energy range from 7 keV to 16 keV and is designed to introduce time delays from -5 to 815 ps with femtosecond resolution. This will allow to study ultrafast dynamics on timescales beyond the repetition rate of X-ray sources. The split-and-delay line unit employs different pairs of silicon Bragg optics to split the incident pulses in two fractions and recombines them at the sample with a precisely controlled time delay. The setup can operate in three configurations, using additional channel cut crystals to increase the achievable time delay range and to guide the beam fractions along various path geometries.

The mechanical design of the split-and-delay unit employs 31 motorized and virtual stages, based on piezo and stepper motors to position the Bragg crystals. The whole unit has a compact dimensions of 60×60×30 cm^3 with a total weight of about 60 kg, which makes the split-and-delay setup portable and suitable to be installed directly in any experimental hutch.

The on-line diagnostics of the developed device consists of a X-ray beam position monitor and intensity diodes in both X-ray branches, which provide the intensity ratio of the two beam fractions. A software package to control the split-and-delay unit was developed in Python. The positioning of all stages and their calibration as well as diagnostic tools are implemented in the convenient user interface and can be operated simultaneously.

The performance of the beam splitting optics was characterized by X-ray topography measurements. Moreover, the optics was studied with synchrotron radiation of PETRA III. A dedicated laser setup was developed and built to calibrate the generated time delays between X-ray pulses. It is based on a infrared laser, employing the interferometer scheme and measuring the interference patterns from the two delay branches. A set of calibration measurements using this laser setup showed an average temporal resolution of 14.3 ps. The calibration results showed a linear relation between the measured branch length difference and the delay time with a 13.5% average deviation from the theoretical estimated values.

The temporal performance of the split-and-delay unit was tested by measuring delay times from 201 ps to 716 ps for 7 keV and from 130 ps to 370 ps for 9 keV with X-rays. It could be shown that the average temporal errors $\Delta\tau$ of the measured delay times are equal to 20 ps and 12.3 ps for 7 keV and 9 keV, respectively.

The results show excellent positioning performance, which is comparable to previously built split-and-delay devices.

Chapter 7

List of abbreviations

ADC	Analog to Digital Converter
APD	Avalanche PhotoDiode
BR	Beam Reflector
BS	Beam Splitter
DESY	Deutsches Elektronen-SYnchrotron
ESRF	European Synchrotron Radiation Facility
FERMI	Free Electron laser Radiation for Multidisciplinary Investigations
FPGA	Field-Programmable Gate Array
FWHM	Full-Width at Half-Maximum
IC	Ionization Chamber
LASER	Light Amplification by Stimulated Emission of Radiation
LCLS	Linac Coherent Light Source

LINAC	LINear ACcelerator
PAL	Pohang Accelerator Laboratory
PETRA	Positron-Elektron-Tandem-Ring-Anlage
PiLC	raspberry Pi Logic Controller
RF	Radio Frequency
SACLA	SPring-8 Angstrom Compact free electron LAser
SDL	Split-and-Delay Line
SASE	Self Amplified Spontaneous Emission
SHV	Safe High Voltage
TAC	Time to Amplitude Converter
TPDI	Two-Photon Double Ionization
VUV	Vacuum UltraViolet
XFEL	X-ray Free Electron Laser
XPCS	X-ray Photon Correlation Spectroscopy
XBPM	X-ray Beam Position Monitor
XRD	X-Ray Diffraction
XSVS	X-ray Speckle Visibility Spectroscopy
YAG	Yttrium Aluminium Garnet

Bibliography

[1] T. Tschentscher, C. Bressler, J. Grünert, A. Madsen, A. Mancuso, M. Meyer, A. Scherz, H. Sinn, and U. Zastrau, “Photon Beam Transport and Scientific Instruments at the European XFEL,” *Applied Sciences*, vol. 7, p. 592, 2017.

[2] M. Yabashi, H. Tanaka, K. Tono, and T. Ishikawa, “Status of the SACLA Facility,” *Applied Sciences*, vol. 7, p. 604, 2017.

[3] M. O. Wiedorn, D. Oberthür, R. Bean, R. Schubert, N. Werner, B. Abbey, M. Aepfelbacher, L. Adriano, A. Allahgholi, N. Al-Qudami, J. Andreasson, S. Aplin, S. Awel, K. Ayyer, S. Bajt, I. Barák, S. Bari, J. Bielecki, S. Botha, D. Boukhelef, W. Brehm, S. Brockhauser, I. Cheviakov, M. A. Coleman, F. Cruz-Mazo, C. Danilevski, C. Darmanin, R. B. Doak, M. Domaracky, K. Dorner, Y. Du, H. Fangohr, H. Fleckenstein, M. Frank, P. Fromme, A. M. Gañán-Calvo, Y. Gevorkov, K. Giewekemeyer, H. M. Ginn, H. Graafsma, R. Graceffa, D. Greiffenberg, L. Gumprecht, P. Göttlicher, J. Hajdu, S. Hauf, M. Heymann, S. Holmes, D. A. Horke, M. S. Hunter, S. Imlau, A. Kaukher, Y. Kim, A. Klyuev, J. Knoška, B. Kobe, M. Kuhn, C. Kupitz, J. Küpper, J. M. Lahey-Rudolph, T. Laurus, K. L. Cong, R. Letrun, P. L. Xavier, L. Maia, F. R. N. C. Maia, V. Mariani, M. Messerschmidt, M. Metz, D. Mezza, T. Michelat, G. Mills, D. C. F. Monteiro, A. Morgan, K. Mühlig, A. Munke, A. Munnich, J. Nette, K. A. Nugent, T. Nuguid, A. M. Orville, S. Pandey, G. Pena, P. Villanueva-Perez, J. Poehlsen, G. Previtali,

L. Redecke, W. M. Riekehr, H. Rohde, A. Round, T. Safenreiter, I. Sarrou, T. Sato, M. Schmidt, B. Schmitt, R. Schönherr, J. Schulz, J. A. Sellberg, M. M. Seibert, C. Seuring, M. L. Shelby, R. L. Shoeman, M. Sikorski, A. Silenzi, C. A. Stan, X. Shi, S. Stern, J. Sztuk-Dambietz, J. Szuba, A. Tolstikova, M. Trebbin, U. Trunk, P. Vagovic, T. Ve, B. Weinhausen, T. A. White, K. Wrona, C. Xu, O. Yefanov, N. Zatsepin, J. Zhang, M. Perbandt, A. P. Mancuso, C. Betzel, H. Chapman, and A. Barty, "Megahertz serial crystallography," *Nature Communications*, vol. 9, 2018.

[4] M. Altarelli, R. Abela, A. Aghababyan, C. Altucci, G. Amatuni, P. Anfinrud, P. Audebert, V. Ayvazyan, N. Baboi, J. Baehr, V. Balandin, R. Bandelmann, J. Becker, B. Beutner, C. Blome, I. Bohnet, A. Bolzmann, C. Bostedt, Y. Bozhko, A. Brandt, S. Bratos, C. Bressler, O. Brovko, H. Brück, J. P. Carneiro, S. Casalbuoni, M. Castellano, P. Castro, L. Catani, A. Cavalleri, S. Celik, H. Chapman, D. Charalambidis, J. Chen, M. Chergui, S. Choroba, A. Cianchi, M. Clausen, E. Collet, H. Danared, C. David, W. Decking, M. Dehler, H. Delsim-Hashemi, G. Dipirro, B. Dobson, M. Dohlus, S. Duesterer, A. Eckhardt, H. J. Eckoldt, H. Edwards, B. Faatz, M. Fajardo, A. Fateev, J. Feldhaus, Y. Filipov, K. Floettmann, R. Follath, B. Fominykh, M. French, J. Frisch, L. Froehlich, E. Gadwinkel, L. Garca-Tabars, J. J. Gareta, T. Garvey, F. Gel'mukhanov, U. Gensch, C. Gerth, M. Goerler, N. Golubeva, H. Graafsma, W. Graeff, O. Grimm, B. Griogoryan, G. Grübel, C. Gutt, K. Hacker, L. Haenisch, U. Hahn, J. Hajdu, J. H. Han, M. Hartrott, J. Havlicek, O. Hensler, K. Honkavaara, V. Honkimäki, T. Hott, M. R. Howells, M. Huening, H. Ihee, F. O. Ilday, R. Ischebeck, M. Jablonka, E. Jaeschke, K. Jensch, J. P. Jensen, S. Johnson, L. Juha, F. Kaerntner, R. Kammering, H. Kapitza, V. Katalev, B. Keil, S. Khodyachykh, R. Kienberger, J. W. Kim, Y. Kim, K. Klose, V. Kocharyan, W. Koehler, M. Koerfer, M. Kollewe, Q. Kong, W. Kook, D. Kostin, O. Kozlov, D. Kraemer, M. Krasilnikov, B. Krause,

O. Krebs, J. Krzywinski, G. Kube, M. Kuhlmann, H. Laich, R. Lange, M. Larsson, R. W. Lee, A. Leuschner, H. Lierl, L. Lilje, T. Limberg, A. Lindenberg, D. Lipka, F. Loehl, K. Ludwig, M. Luong, C. Magne, A. Maquet, J. Marangos, C. Masciovecchio, M. Maslov, A. Matheisen, E. Matyushevskiy, O. Matzen, H. J. May, I. McNulty, D. McCormick, P. Meulen, N. Meyners, P. Michelato, N. Mildner, V. Miltchev, M. Minty, W. D. Moeller, T. Möller, L. Monaco, M. Nagl, O. Napoly, G. Neubauer, P. Nicolosi, A. Nienhaus, D. Noelle, T. Nunez, F. Obier, A. Oppelt, C. Pagani, R. Paparella, H. B. Pedersen, B. Petersen, B. Petrosyan, L. Petrosyan, A. Petrov, P. Piot, J. Pflueger, A. Plech, E. Plönjes, L. Poletto, G. Pöplau, E. Prat, S. Prat, J. Prenting, D. Proch, D. Pugachov, H. Quack, B. Racky, D. Ramert, H. Redlin, K. Rehlich, R. Reininger, H. Remde, D. Reschke, D. Richter, M. Richter, S. Riemann, D. Riley, I. Robinson, J. Roensch, F. Rosmej, M. Ross, J. Rossbach, V. Rybnikov, M. Sachwitz, E. Saldin, W. Sandner, J. Schäfer, T. Schilcher, H. Schlarb, M. Schloesser, V. Schlott, B. Schmidt, M. Schmitz, P. Schmueser, J. Schneider, E. Schneidmiller, F. Schotte, S. Schrader, S. Schreiber, C. Schroer, R. Schuch, H. Schulte-Schrepping, A. Schwarz, M. Seidel, J. Sekutowicz, P. Seller, D. Sellmann, F. Senf, D. Sertore, A. Shabunov, S. Simrock, W. Singer, H. Sinn, R. Smith, E. Sombrowski, A. A. Sorokin, E. Springate, M. Staack, L. Staykov, B. Steffen, B. Stephenson, F. Stephan, F. Stulle, E. Syresin, K. Sytchev, V. Sytchev, G. Tallents, S. Techert, N. Tesch, H. Thom, K. Tiedtke, M. Tischer, M. Tolan, S. Toleikis, F. Toral, R. Treusch, D. Trines, V. Tsakanov, I. Tsakov, T. Tschentscher, F. R. Ullrich, U. van Rienen, A. Variola, I. Vartaniants, E. Vogel, J. Vogel, R. Vuilleumier, H. Wabnitz, R. Wanzenberg, J. S. Wark, H. Weddig, T. Weiland, H. Weise, M. Wendt, R. Wenndorff, R. Wichmann, I. Will, A. Winter, K. Witte, K. Wittenburg, P. Wochner, T. Wohlenberg, J. Wojtkiewicz, A. Wolf, M. Wulff, M. Yurkov, I. Zagorodnov, P. Zambolin, K. Zapfe, P. Zeitoun, V. Ziemann, A. Zolotov, R. Brinkmann, and H. J. Grabosch, *"XFEL:*

The European X-Ray Free-Electron Laser - Technical Design Report". Hamburg: DESY, 2006.

[5] P. Emma, R. Akre, J. Arthur, R. Bionta, C. Bostedt, J. Bozek, A. Brachmann, P. Bucksbaum, R. Coffee, F.-J. Decker, Y. Ding, D. Dowell, S. Edstrom, A. Fisher, J. Frisch, S. Gilevich, J. Hastings, G. Hays, P. Hering, Z. Huang, R. Iverson, H. Loos, M. Messerschmidt, A. Miahnahri, S. Moeller, H.-D. Nuhn, G. Pile, D. Ratner, J. Rzepiela, D. Schultz, T. Smith, P. Stefan, H. Tompkins, J. Turner, J. Welch, W. White, J. Wu, G. Yocky, and J. Galayda, "First lasing and operation of an ångstrom-wavelength free-electron laser," *Nature Photonics*, vol. 4, p. 641, 2010.

[6] E.-S. Kim and M. Yoon, "Beam dynamics in a 10-GeV linear accelerator for the X-ray free electron laser at PAL," *IEEE Transactions on Nuclear Science*, vol. 56, p. 3597, 2009.

[7] P. M. Chaikin and T. C. Lubensky, *"Principles of condensed matter physics"*, vol. 1. Cambridge university press Cambridge, 2000.

[8] S. Komura, *"Dynamics of ordering processes in condensed matter"*. Springer Science & Business Media, 2012.

[9] B. W. J. McNeil and N. R. Thompson, "X-ray free-electron lasers," *Nature Photonics*, vol. 4, p. 814, 2010.

[10] D. H. Bilderback, P. Elleaume, and E. Weckert, "Review of third and next generation synchrotron light sources," *Journal of Physics B: Atomic, Molecular and Optical Physics*, vol. 38, p. 773, 2005.

[11] H. Ihee, "Ultrafast X-ray diffraction of transient molecular structures in solution," *Science*, vol. 309, p. 1223, 2005.

[12] G. Grübel, "X-ray photon correlation spectroscopy at the european X-ray free-electron laser (XFEL) facility," *Comptes Rendus Physique*, vol. 9, p. 668, 2008.

[13] O. G. Shpyrko, "X-ray photon correlation spectroscopy," *Journal of Synchrotron Radiation*, vol. 21, p. 1057, 2014.

[14] E. M. Dufresne, S. Narayanan, A. R. Sandy, D. M. Kline, Q. Zhang, E. C. Landahl, and S. Ross, "Pushing X-ray photon correlation spectroscopy beyond the continuous frame rate limit," *Optics Express*, vol. 24, p. 355, 2016.

[15] W. Roseker, H. Franz, H. Schulte-Schrepping, A. Ehnes, O. Leupold, F. Zontone, S. Lee, A. Robert, and G. Grübel, "Development of a hard X-ray delay line for X-ray photon correlation spectroscopy and jitter-free pump–probe experiments at X-ray free-electron laser sources," *Journal of Synchrotron Radiation*, vol. 18, p. 481, 2011.

[16] W. Roseker, H. Franz, H. Schulte-Schrepping, A. Ehnes, O. Leupold, F. Zontone, A. Robert, and G. Grübel, "Performance of a picosecond X-ray delay line unit at 8.39 kev," *Optics Letters*, vol. 34, p. 1768, 2009.

[17] D. Zhu, Y. Sun, D. W. Schafer, H. Shi, J. H. James, K. L. Gumerlock, T. O. Osier, R. Whitney, L. Zhang, J. Nicolas, B. Smith, A. H. Barada, and A. Robert, "Development of a hard X-ray split-delay system at the Linac Coherent Light Source," in *Advances in X-ray Free-Electron Lasers Instrumentation IV*, vol. 10237, SPIE, 2017.

[18] T. Hirano, T. Osaka, Y. Morioka, Y. Sano, Y. Inubushi, T. Togashi, I. Inoue, S. Matsuyama, K. Tono, A. Robert, J. B. Hastings, K. Yamauchi, and M. Yabashi, "Performance of a hard X-ray split-and-delay optical system with a wavefront division," *Journal of Synchrotron Radiation*, vol. 25, p. 20, 2018.

[19] T. Osaka, T. Hirano, Y. Sano, Y. Inubushi, S. Matsuyama, K. Tono, T. Ishikawa, K. Yamauchi, and M. Yabashi, "Wavelength-tunable split-and-delay optical system for hard X-ray free-electron lasers," *Optics Express*, vol. 24, p. 9187, 2016.

[20] W. Lu, T. Noll, T. Roth, I. Agapov, G. Geloni, M. Holler, J. Hallmann, G. Ansaldi, S. Eisebitt, and A. Madsen, "Design and throughput simulations of a hard X-ray split and delay line for the MID station at the european XFEL," in *AIP Conference Proceedings*, 2016.

[21] W. Lu, B. Friedrich, T. Noll, K. Zhou, J. Hallmann, G. Ansaldi, T. Roth, S. Serkez, G. Geloni, A. Madsen, and S. Eisebitt, "Development of a hard X-ray split-and-delay line and performance simulations for two-color pump-probe experiments at the european XFEL," *Review of Scientific Instruments*, vol. 89, p. 063121, 2018.

[22] W. Roseker, S. O. Hruszkewycz, F. Lehmkühler, M. Walther, H. Schulte-Schrepping, S. Lee, T. Osaka, L. Strüder, R. Hartmann, M. Sikorski, S. Song, A. Robert, P. H. Fuoss, M. Sutton, G. B. Stephenson, and G. Grübel, "Towards ultrafast dynamics with split-pulse X-ray photon correlation spectroscopy at free electron laser sources," *Nature Communications*, vol. 9, p. 1704, 2018.

[23] W. Röntgen, "Über eine neue Art von Strahlen," *Sber. Physik.-med. Ges. Würzburg*, vol. 9, p. 132, 1895.

[24] S. Schreiber, B. Faatz, J. Feldhaus, K. Honkavaara, and R. Treusch, "FEL user facility Flash," in *Proc. of the 2010 International Particle Accelerator Conference, Kyoto*, 2010.

[25] "FLASH Accelerator web page." `http://flash.desy.de/accelerator/`.

[26] B. Faatz, N. Baboi, V.Bal, W. Decking, S. Duesterer, J. Feldhaus, N. A. Golubeva, T. Laarmann, T. Limberg, D. Nölle, E. Plönjes, H. Schlarb, S. Schreiber, F. Tavella,

K. Tiedtke, and R. Treusch, "FLASH II: a Seeded Future at FLASH," *Conference Proceedings (IPAC'10)*, vol. C100523, p. 2152, 2010.

[27] "LCLS Technical Design Report web-page." `http://www-ssrl.slac.stanford.edu/lcls/cdr/`.

[28] "LCLS II web-page." `https://lcls.slac.stanford.edu/lcls-ii/design-and-performance`.

[29] T. Shintake *et al.*, "Status report on japanese XFEL construction project at SPring-8," in *Proceedings of the 2010 International Particle Accelerator Conference*, 2010.

[30] "SACLA Technical Design Report web-page." `http://{XFEL}.riken.jp/eng/pdf/{XFEL}_BL-TDRver1.0.pdf`.

[31] L. Giannessi, "The FERMI@Elettra commissioning," in *FEL 201213, 4th International Free Electron Laser Conference*, vol. 1, p. 13, 2012.

[32] E. Allaria, C. Callegari, D. Cocco, W. M. Fawley, M. Kiskinova, C. Masciovecchio, and F. Parmigiani, "The FERMI@Elettra free-electron-laser source for coherent X-ray physics: photon properties, beam transport system and applications," *New Journal of Physics*, vol. 12, p. 075002, 2010.

[33] B. D. Patterson, R. Abela, H.-H. Braun, U. Flechsig, R. Ganter, Y. Kim, E. Kirk, A. Oppelt, M. Pedrozzi, S. Reiche, L. Rivkin, T. Schmidt, B. Schmitt, V. N. Strocov, S. Tsujino, and A. F. Wrulich, "Coherent science at the SwissFEL X-ray laser," *New Journal of Physics*, vol. 12, p. 035012, 2010.

[34] "SwissFEL Conceptual Design Report web-page." `https://www.psi.ch/swissfel/HomeEN/SwissFEL_CDR_web_small.pdf`.

[35] "PAL FEL Technical Design Report web-page." `http://pal.postech.ac.kr/downloadServlet?file_path=/home/pal/ROOT/download&file_name=PAL_XFEL_TDR.pdf`.

[36] W. Crookes, "On the illumination of lines of molecular pressure, and the trajectory of molecules," *Proceedings of the Royal Society of London*, vol. 170, p. 1535, 1879.

[37] K. Balewski, W. Brefeld, W. Decking, H. Franz, R. Rohlsberger, and E. Weckert, *PETRA III: A low emittance synchrotron radiation source (Technical design report)*. ISSN: 0418-9833.

[38] R. Haensel, "European Synchrotron Radiation Facility (ESRF)," *Review of Scientific Instruments*, vol. 63, p. 1571, 1992.

[39] J. A. Clarke, *"The science and technology of undulators and wigglers"*, vol. 4. Oxford University Press on Demand, 2004.

[40] A. Kondratenko and E. Saldin, "Generating of coherent radiation by a relativistic electron beam in an ondulator," *Part. Accel.*, vol. 10, p. 207, 1980.

[41] J. M. J. Madey, "Stimulated emission of bremsstrahlung in a periodic magnetic field," *Journal of Applied Physics*, vol. 42, p. 1906, 1971.

[42] C. Pellegrini, A. Marinelli, and S. Reiche, "The physics of x-ray free-electron lasers," *Reviews of Modern Physics*, vol. 88, 2016.

[43] C. W. Siders, "Detection of nonthermal melting by ultrafast x-ray diffraction," *Science*, vol. 286, p. 1340, 1999.

[44] D. Brinks, R. Hildner, E. M. H. P. van Dijk, F. D. Stefani, J. B. Nieder, J. Hernando, and N. F. van Hulst, "Ultrafast dynamics of single molecules," *Chemical Society Reviews*, vol. 43, p. 2476, 2014.

[45] A. M. Lindenberg, S. Engemann, K. J. Gaffney, K. Sokolowski-Tinten, J. Larsson, P. B. Hillyard, D. A. Reis, D. M. Fritz, J. Arthur, R. A. Akre, M. J. George, A. Deb, P. H. Bucksbaum, J. Hajdu, D. A. Meyer, M. Nicoul, C. Blome, T. Tschentscher, A. L. Cavalieri, R. W. Falcone, S. H. Lee, R. Pahl, J. Rudati, P. H. Fuoss, A. J. Nelson, P. Krejcik, D. P. Siddons, P. Lorazo, and J. B. Hastings, "X-Ray Diffuse Scattering Measurements of Nucleation Dynamics at Femtosecond Resolution," *Physical Review Letters*, vol. 100, 2008.

[46] G. B. Stephenson, A. Robert, and G. Grübel, "Revealing the atomic dance," *Nature Materials*, vol. 8, p. 702, Sept. 2009.

[47] M. Chollet, R. Alonso-Mori, M. Cammarata, D. Damiani, J. Defever, J. T. Delor, Y. Feng, J. M. Glownia, J. B. Langton, S. Nelson, K. Ramsey, A. Robert, M. Sikorski, S. Song, D. Stefanescu, V. Srinivasan, D. Zhu, H. T. Lemke, and D. M. Fritz, "The X-ray pump–probe instrument at the linac coherent light source," *Journal of Synchrotron Radiation*, vol. 22, p. 503, 2015.

[48] C. Gutt, L.-M. Stadler, S. Streit-Nierobisch, A. P. Mancuso, A. Schropp, B. Pfau, C. M. Günther, R. Könnecke, J. Gulden, B. Reime, J. Feldhaus, E. Weckert, I. A. Vartanyants, O. Hellwig, F. Staier, R. Barth, M. Grunze, A. Rosenhahn, D. Stickler, H. Stillrich, R. Frömter, H. P. Oepen, M. Martins, T. Nisius, T. Wilhein, B. Faatz, N. Guerassimova, K. Honkavaara, V. Kocharyan, R. Treusch, E. Saldin, S. Schreiber, E. A. Schneidmiller, M. V. Yurkov, S. Eisebitt, and G. Grübel, "Resonant magnetic scattering with soft X-ray pulses from a free-electron laser operating at 1.59 nm," *Physical Review B*, vol. 79, p. 212406, 2009.

[49] C. Gutt, S. Streit-Nierobisch, L.-M. Stadler, B. Pfau, C. M. Günther, R. Könnecke, R. Frömter, A. Kobs, D. Stickler, H. P. Oepen, R. R. Fäustlin, R. Treusch, J. Feldhaus, E. Weckert, I. A. Vartanyants, M. Grunze, A. Rosenhahn, T. Wilhein,

S. Eisebitt, and G. Grübel, “Single-pulse resonant magnetic scattering using a soft X-ray free-electron laser,” *Physical Review B*, vol. 81, p. 100401, 2010.

[50] L. Müller, C. Gutt, S. Streit-Nierobisch, M. Walther, S. Schaffert, B. Pfau, J. Geilhufe, F. Büttner, S. Flewett, C. M. Günther, S. Eisebitt, A. Kobs, M. Hille, D. Stickler, R. Frömter, H. P. Oepen, J. Lüning, and G. Grübel, “Endstation for ultrafast magnetic scattering experiments at the free-electron laser in Hamburg,” *Review of Scientific Instruments*, vol. 84, p. 013906, 2013.

[51] R. Pan, E. Zapolnova, T. Golz, A. J. Krmpot, M. D. Rabasovic, J. Petrovic, V. Asgekar, B. Faatz, F. Tavella, A. Perucchi, S. Kovalev, B. Green, G. Geloni, T. Tanikawa, M. Yurkov, E. Schneidmiller, M. Gensch, and N. Stojanovic, “Photon diagnostics at the FLASH THz beamline,” *Journal of Synchrotron Radiation*, vol. 26, p. 700, 2019.

[52] M. Drescher, M. Hentschel, R. Kienberger, M. Uiberacker, V. Yakovlev, A. Scrinzi, T. Westerwalbesloh, U. Kleineberg, U. Heinzmann, and F. Krausz, “Time-resolved atomic inner-shell spectroscopy,” *Nature*, vol. 419, p. 803, 2002.

[53] G. Grübel and F. Zontone, “Correlation spectroscopy with coherent X-rays,” *Journal of Alloys and Compounds*, vol. 362, p. 3, 2004.

[54] A. R. Sandy, Q. Zhang, and L. B. Lurio, “Hard X-ray photon correlation spectroscopy methods for materials studies,” *Annual Review of Materials Research*, vol. 48, p. 167, 2018.

[55] F. Lehmkühler, J. Valerio, D. Sheyfer, W. Roseker, M. A. Schroer, B. Fischer, K. Tono, M. Yabashi, T. Ishikawa, and G. Grübel, “Dynamics of soft nanoparticle suspensions at hard X-ray FEL sources below the radiation-damage threshold,” *International Union of Crystallography Journal*, vol. 5, p. 801, 2018.

[56] P. K. Dixon and D. J. Durian, “Speckle visibility spectroscopy and variable granular fluidization,” *Physical Review Letters*, vol. 90, p. 184302, 2003.

[57] R. Bandyopadhyay, A. S. Gittings, S. S. Suh, P. K. Dixon, and D. J. Durian, “Speckle-visibility spectroscopy: A tool to study time-varying dynamics,” *Review of Scientific Instruments*, vol. 76, p. 093110, 2005.

[58] I. Inoue, Y. Shinohara, A. Watanabe, and Y. Amemiya, “Effect of shot noise on X-ray speckle visibility spectroscopy,” *Optics Express*, vol. 20, p. 26878, 2012.

[59] C. DeCaro, V. N. Karunaratne, S. Bera, L. B. Lurio, A. R. Sandy, S. Narayanan, M. Sutton, J. Winans, K. Duffin, J. Lehuta, and N. Karonis, “X-ray speckle visibility spectroscopy in the single-photon limit,” *Journal of Synchrotron Radiation*, vol. 20, p. 332, 2013.

[60] L. Li, P. Kwaśniewski, D. Orsi, L. Wiegart, L. Cristofolini, C. Caronna, and A. Fluerasu, “Photon statistics and speckle visibility spectroscopy with partially coherent X-rays,” *Journal of Synchrotron Radiation*, vol. 21, p. 1288, 2014.

[61] J. Verwohlt, M. Reiser, L. Randolph, A. Matic, L. A. Medina, A. Madsen, M. Sprung, A. Zozulya, and C. Gutt, “Low dose X-ray speckle visibility spectroscopy reveals nanoscale dynamics in radiation sensitive ionic liquids,” *Physical Review Letters*, vol. 120, p. 168001, 2018.

[62] F. Perakis, G. Camisasca, T. J. Lane, A. Späh, K. T. Wikfeldt, J. A. Sellberg, F. Lehmkühler, H. Pathak, K. H. Kim, K. Amann-Winkel, S. Schreck, S. Song, T. Sato, M. Sikorski, A. Eilert, T. McQueen, H. Ogasawara, D. Nordlund, W. Roseker, J. Koralek, S. Nelson, P. Hart, R. Alonso-Mori, Y. Feng, D. Zhu, A. Robert, G. Grübel, L. G. M. Pettersson, and A. Nilsson, “Coherent X-rays reveal the influence of cage effects on ultrafast water dynamics,” *Nature Communications*, vol. 9, p. 1917, 2018.

[63] C. Gutt, L.-M. Stadler, A. Duri, T. Autenrieth, O. Leupold, Y. Chushkin, and G. Grübel, “Measuring temporal speckle correlations at ultrafast X-ray sources,” *Optics Express*, vol. 17, p. 55, 2008.

[64] P. Emma, K. Bane, M. Cornacchia, Z. Huang, H. Schlarb, G. Stupakov, and D. Walz, “Femtosecond and Subfemtosecond X-ray Pulses from a Self-Amplified Spontaneous-Emission–Based Free-Electron Laser,” *Physical Review Letters*, vol. 92, p. 074801, 2004.

[65] A. A. Lutman, R. Coffee, Y. Ding, Z. Huang, J. Krzywinski, T. Maxwell, M. Messerschmidt, and H.-D. Nuhn, “Experimental Demonstration of Femtosecond Two-Color X-ray Free-Electron Lasers,” *Physical Review Letters*, vol. 110, p. 134801, 2013.

[66] E. Ferrari, C. Spezzani, F. Fortuna, R. Delaunay, F. Vidal, I. Nikolov, P. Cinquegrana, B. Diviacco, D. Gauthier, G. Penco, P. R. Ribič, E. Roussel, M. Trovò, J.-B. Moussy, T. Pincelli, L. Lounis, M. Manfredda, E. Pedersoli, F. Capotondi, C. Svetina, N. Mahne, M. Zangrando, L. Raimondi, A. Demidovich, L. Giannessi, G. D. Ninno, M. B. Danailov, E. Allaria, and M. Sacchi, “Widely tunable two-colour seeded free-electron laser source for resonant-pump resonant-probe magnetic scattering,” *Nature Communications*, vol. 7, p. 10343, 2016.

[67] Y. Sun, F.-J. Decker, J. Turner, S. Song, A. Robert, and D. Zhu, “Pulse intensity characterization of the LCLS nanosecond double-bunch mode of operation,” *Journal of Synchrotron Radiation*, vol. 25, p. 642, 2018.

[68] S. Roling and H. Zacharias, “Split-and-delay units for soft and hard X-rays,” in *Synchrotron Light Sources and Free-Electron Lasers*, p. 891, Springer International Publishing, 2016.

[69] F. Sorgenfrei, W. F. Schlotter, T. Beeck, M. Nagasono, S. Gieschen, H. Meyer, A. Föhlisch, M. Beye, and W. Wurth, "The extreme ultraviolet split and femtosecond delay unit at the plane grating monochromator beamline PG2 at FLASH," *Review of Scientific Instruments*, vol. 81, p. 043107, 2010.

[70] R. Mitzner, B. Siemer, M. Neeb, T. Noll, F. Siewert, S. Roling, M. Rutkowski, A. A. Sorokin, M. Richter, P. Juranic, K. Tiedtke, J. Feldhaus, W. Eberhardt, and H. Zacharias, "Spatio-temporal coherence of free electron laser pulses in the soft X-ray regime," *Optics Express*, vol. 16, p. 19909, 2008.

[71] R. Mitzner, M. Neeb, T. Noll, N. Pontius, and W. Eberhardt, "An X-ray autocorrelator and delay line for the VUV-FEL at TTF/DESY," in *Ultrafast X-ray Detectors, High-Speed Imaging, and Applications*, vol. 5920, SPIE, 2005.

[72] T. Osaka, T. Hirano, M. Yabashi, Y. Sano, K. Tono, Y. Inubushi, T. Sato, K. Ogawa, S. Matsuyama, T. Ishikawa, and K. Yamauchi, "Development of split-delay X-ray optics using si(220) crystals at SACLA," in *Proc.SPIE*, vol. 9210, p. 9210, 2014.

[73] S. Roling, S. Braun, P. Gawlitza, L. Samoylova, B. Siemer, H. Sinn, F. Siewert, F. Wahlert, M. Wöstmann, and H. Zacharias, "A split- and delay-unit for the european XFEL," in *Advances in X-ray Free-Electron Lasers II: Instrumentation*, vol. 8778, SPIE, 2013.

[74] S. Roling, V. Kärcher, L. Samoylova, K. Appel, S. Braun, P. Gawlitza, F. Siewert, U. Zastrau, M. Rollnik, F. Wahlert, and H. Zacharias, "A hard X-ray split-and-delay unit for the HED instrument at the european XFEL," in *Advances in X-ray Free-Electron Lasers Instrumentation IV*, vol. 10237, SPIE, 2017.

[75] C. Darwin, "XXXIV. the theory of X-ray reflexion," *The London, Edinburgh, and Dublin Philosophical Magazine and Journal of Science*, vol. 27, p. 315, 1914.

[76] B. Batterman and H. Cole, “Dynamical diffraction of x rays by perfect crystals,” *Reviews of Modern Physics*, vol. 36, p. 681, 1964.

[77] W. Zachariasen, *"Theory of X-ray Diffraction in Crystals"*. Dover phoenix editions, Dover Publications, 2004.

[78] Z. Pinsker, *"Dynamical Scattering of X-rays in Crystals"*. Springer-Verlag Berlin Heidelberg, 1978.

[79] A. Authier, *"Dynamical Theory of X-ray Diffraction"*. IUCr monographs on crystallography, Oxford University Press, 2004.

[80] L. Øgendal, *"Light Scattering Demystified"*. University of Copenhagen, 2019.

[81] D. Koningsberger and R. Prins, *"X-ray Absorption: Principles, Applications, Techniques of EXAFS, SEXAFS and XANES"*. Chemical Analysis: A Series of Monographs on Analytical Chemistry and Its Applications, Wiley, 1988.

[82] S. Wallwork, *"Introduction to the calculation of structure factors"*. University College Cardiff Press, 1980.

[83] W. M. Vetter, “The characterization of defects in silicon carbide crystals by X-ray topography in the back-reflection geometry,” *Defect and Diffusion Forum*, vol. 230, p. 1, 2004.

[84] W. M. Vetter and M. Dudley, “X-ray topographic dislocation contrast visible in reflections orthogonal to the burgers vectors of axial screw dislocations in hexagonal silicon carbide,” *Journal of Applied Crystallography*, vol. 34, p. 20, 2001.

[85] D. Nakamura, S. Yamaguchi, I. Gunjishima, Y. Hirose, and T. Kimoto, “Topographic study of dislocation structure in hexagonal SiC single crystals with low dislocation density,” *Journal of Crystal Growth*, vol. 304, p. 57, 2007.

[86] T. N. T. Thi, J. Morse, D. Caliste, B. Fernandez, D. Eon, J. Härtwig, C. Barbay, C. Mer-Calfati, N. Tranchant, J. C. Arnault, T. A. Lafford, and J. Baruchel, "Synchrotron bragg diffraction imaging characterization of synthetic diamond crystals for optical and electronic power device applications," *Journal of Applied Crystallography*, vol. 50, p. 561, 2017.

[87] J. ul Hassan, *Epitaxial Growth and Characterization of SiC for High Power Devices*. PhD thesis, Linköping University, 2009.

[88] G. Grübel, G. Stephenson, C. Gutt, H. Sinn, and T. Tschentscher, "XPCS at the european X-ray free electron laser facility," *Nuclear Instruments and Methods in Physics Research Section B: Beam Interactions with Materials and Atoms*, vol. 262, p. 357, 2007.

[89] A. G. Michette, *"Optical Systems for Soft X Rays"*. Springer US, 1986.

[90] D. Bilderback, B. Lairson, T. Barbee Jr, G. Ice, and C. Sparks Jr, "Design of doubly focusing, tunable (5–30 kev), wide bandpass optics made from layered synthetic microstructures," *Nuclear Instruments and Methods in Physics Research*, vol. 208, p. 251, 1983.

[91] D. Nagel, J. Gilfrich, and T. Barbee Jr, "Bragg diffractors with graded-thickness multilayers," *Nuclear Instruments and Methods in Physics Research*, vol. 195, p. 63, 1982.

[92] W. Roseker, *Development of an X-Ray Delay Unit for Correlation Spectroscopy and Pump-Probe Experiments*. Dr., Universität Hamburg, 2008. Universität Hamburg, Diss., 2008.

[93] D. Koningsberger and R. Prins, *"Group IV Elements, IV-IV and III-V Compounds. Part b - Electronic, Transport, Optical and Other Properties"*. Berlin, Heidelberg: Springer, 2002.

[94] L. G. Carpenter, H. L. Rogers, C. Holmes, J. C. Gates, and P. G. R. Smith, "Facet machining of silica waveguides with nanoscale roughness without polishing or lapping," in *2013 Conference on Lasers & Electro-Optics Europe & International Quantum Electronics Conference CLEO EUROPE/IQEC*, IEEE, 2013.

[95] M. Wöstmann, R. Mitzner, T. Noll, S. Roling, B. Siemer, F. Siewert, S. Eppenhoff, F. Wahlert, and H. Zacharias, "The XUV split-and-delay unit at beamline BL2 at FLASH," *Journal of Physics B: Atomic, Molecular and Optical Physics*, vol. 46, p. 164005, 2013.

[96] N. Kujala, M. Makita, J. Liu, A. Zozulya, M. Sprung, C. David, and J. Grünert, "Characterizing transmissive diamond gratings as beam splitters for the hard X-ray single-shot spectrometer of the european XFEL," *Journal of Synchrotron Radiation*, vol. 26, p. 708, 2019.

[97] T. Osaka, M. Yabashi, Y. Sano, K. Tono, Y. Inubushi, T. Sato, S. Matsuyama, T. Ishikawa, and K. Yamauchi, "A bragg beam splitter for hard X-ray free-electron lasers," *Optics Express*, vol. 21, p. 2823, 2013.

[98] S. Rutishauser, L. Samoylova, J. Krzywinski, O. Bunk, J. Grünert, H. Sinn, M. Cammarata, D. M. Fritz, and C. David, "Exploring the wavefront of hard X-ray free-electron laser radiation," *Nature Communications*, vol. 3, 2012.

[99] T. Osaka, T. Hirano, Y. Inubushi, M. Yabashi, Y. Sano, S. Matsuyama, K. Tono, T. Sato, K. Ogawa, T. Ishikawa, and K. Yamauchi, "Development of hard X-ray split-delay optics based on si(220) crystals," in *JSAP-OSA Joint Symposia 2014 Abstracts*, OSA, 2014.

[100] W. J. Bartels, J. Hornstra, and D. J. W. Lobeek, "X-ray diffraction of multilayers and superlattices," *Acta Crystallographica Section A Foundations of Crystallography*, vol. 42, p. 539, 1986.

[101] W. J. Bartels, “Characterization of thin layers on perfect crystals with a multipurpose high resolution X-ray diffractometer,” *Journal of Vacuum Science & Technology B: Microelectronics and Nanometer Structures*, vol. 1, p. 338, 1983.

[102] T. Matsushita and H. Hashizume, *”Handbook on Synchrotron Radiation: X-ray Monochromators*. North-Holland Publishing Company, 1983.

[103] J. W. M. DuMond, “Theory of the use of more than two successive X-ray crystal reflections to obtain increased resolving power,” *Physical Review*, vol. 52, p. 872, 1937.

[104] S. Brauer, G. B. Stephenson, M. Sutton, S. G. J. Mochrie, S. B. Dierker, R. M. Fleming, R. Pindak, I. K. Robinson, G. Grübel, J. Als-Nielsen, and D. L. Abernathy, “Asymmetrically cut crystals as optical elements for highly collimated X-ray beams,” *Review of Scientific Instruments*, vol. 66, p. 1506, 1995.

[105] J. H. Williams and S. K. Allison, “Design of a double X-ray spectrometer,” *Journal of the Optical Society of America*, vol. 18, p. 473, 1929.

[106] J. Luo and D. Dornfeld, “Material removal mechanism in chemical mechanical polishing: theory and modeling,” *IEEE Transactions on Semiconductor Manufacturing*, vol. 14, p. 112, 2001.

[107] “SmarAct web page.” `http://www.smaract.com/`.

[108] “SmarPod Programmer’s Guide.” `https://www.smaract.de/`.

[109] R. L. Owen, J. M. Holton, C. Schulze-Briese, and E. F. Garman, “Determination of X-ray flux using silicon pin diodes,” *Journal of Synchrotron Radiation*, vol. 16, p. 143, 2009.

[110] P. Goettlicher, ed., *Studiengruppe Elektronische Instrumentierung: Proceedings, 106. SEI-Tagung*, (Hamburg), DESY, 2015.

[111] "Tango controls web-page." `https://www.tango-controls.org/`.

[112] "BM05 beamline web-page." `https://www.esrf.eu/UsersAndScience/Experiments/XNP/BM05`.

[113] J.-C. Labiche, O. Mathon, S. Pascarelli, M. A. Newton, G. G. Ferre, C. Curfs, G. Vaughan, A. Homs, and D. F. Carreiras, "The fast readout low noise camera as a versatile X-ray detector for time resolved dispersive extended X-ray absorption fine structure and diffraction studies of dynamic problems in materials science, chemistry, and catalysis," *Review of Scientific Instruments*, vol. 78, p. 091301, 2007.

[114] "P10 beamline web-page." `http://photon-science.desy.de/facilities/petra_iii/beamlines/p10_coherence_applications/index_eng.html`.

[115] W. Roseker, S. Lee, M. Walther, R. Rysov, M. Sprung, and G. Grübel, "Spatial and temporal pre-alignment of an X-ray split-and-delay unit by laser light interferometry," *Review of Scientific Instruments*, vol. 90, p. 045106, 2019.

[116] D. Attwood, *"Soft X-rays and Extreme Ultraviolet Radiation"*. Cambridge University Press, 1999.

[117] T. Osaka, T. Hirano, Y. Morioka, Y. Sano, Y. Inubushi, T. Togashi, I. Inoue, K. Tono, A. Robert, K. Yamauchi, J. B. Hastings, and M. Yabashi, "Characterization of temporal coherence of hard X-ray free-electron laser pulses with single-shot interferograms," *International Union of Crystallography Journal*, vol. 4, p. 728, 2017.

[118] S. J. Orfanidis, *"Introduction to Signal Processing"*. Englewood Cliffs, NJ: Prentice-Hall, 1996.

[119] D. Bowen and B. Tanner, *"High resolution X-ray diffractometry and topography"*. CRC press, 2005.

[120] "Athena: Hephaestus EXAFS software manual web-page." `https://bruceravel.github.io/demeter/documents/Athena/hephaestus.html`.

[121] M. Jergel, Y. Halahovets, I. Maťko, D. Korytár, Z. Zápražný, J. Hagara, P. Nádaždy, P. Šiffalovič, J. Kečkéš, and E. Majková, "Finishing of Ge nanomachined surfaces for X-ray crystal optics," *The International Journal of Advanced Manufacturing Technology*, vol. 96, p. 3603, 2018.

[122] T. Roth, W. Freund, U. Boesenberg, G. Carini, S. Song, G. Lefeuvre, A. Goikhman, M. Fischer, M. Schreck, J. Grünert, and A. Madsen, "Pulse-resolved intensity measurements at a hard X-ray FEL using semi-transparent diamond detectors," *Journal of Synchrotron Radiation*, vol. 25, p. 177, 2018.

Acknowledgements

First of all, I would like to express my gratitude to Prof. Dr. Gerhard Grübel and Dr. Wojciech Roseker for making my project possible. To Prof. Dr. Gerhard Grübel I am thankful for all of the opportunities I was given to conduct this research at DESY and advance my scientific carreer. I would like to thank my supervisor Dr. Wojciech Roseker for his tremendous support on my Ph.D topic and sharing his immense knowledge.

I would like to thank Prof. Dr. Martin Trebbin for being my second supervisor, for his genuine interest in the subject and careful reading of my thesis manuscript. Additionally, I am grateful to Michael Walther for his work on the SDL design as well as fruitful discussions and experienced pieces of advice.

Many thanks as well to the P64 beamline stuff, especially to Vadim Murzin and Wolfgang Caliebe. They supported me for the experimental investigations of the SDL giving a helpful opportunity to perform X-ray experiments.

I thank Dr. Leonard Müller, Dr. Andre Philippi-Kobs and Matthias Riepp for participating in numerous beamtimes related to their projects in the magnetism world and for useful knowledge and advices regarding the experimental work. Many thanks to my former and current colleagues in the Coherent X-Ray Scattering Group - Dr. Felix Lehmkühler, Verena Markmann, Donatella Rosetti, Dr. Irina Lokteva, Dr. Wonhyuk Jo, Dr. Francesco Dallari, Dr. Joana Valerio, Michael Koof, Dr. Dina Sheyfer, Dr. Michael Höltig, Dr. Magnus Berntsen and others who worked with me and supported me during this years.

I thank as well to Dr. Volodymyr Myronenko for careful reading of my thesis and providing me a useful advices on scientific writing.

Furthermore, I would like to acknowledge and thank my friends in Hamburg:

Anastasiia Velyka, Mykyta Haranko, Dr. Mykola Biednov, Nastasia Mukharamova, Dr. Nataliia Kovalchuk, Dr. Mark Stöver, Dr. Dmitry Dzhigaev, Natalia Zolotova, Aleksandra Tolstikova, Aram Kalaydzhyan and others. Your friendship and support are very important to me.

Special thank goes to Kateryna Frantseva for the enormous personal support of mine since my university years.

Finally I would like to thank my parents for their patience, wise counsel and sympathetic ear. You are always here to help me.

Eidesstattliche Versicherung

Hiermit erkläre ich an Eides statt, dass ich die vorliegende Dissertationsschrift selbst verfasst und keine anderen als die angegebenen Quellen und Hilfsmittel benutzt habe.

Declaration on oath

I hereby declare, on oath, that I have written the present dissertation by my own and have not used other than the acknowledged resources and aids.

Hamburg,
August 6, 2019